The Dissertation Committee for Seth Weisberg Certifies that this is the approved version of the following Dissertation:

Nanoscale Synaptic Plasticity of Aspiny Interneuron Dendrites with Respect to Characteristic Fine Structures

Committee:

Kristen M. Harris, Supervisor

Boris Zemelman

Laura L. Colgin

Hiroshi Nishiyama

Hans Hofmann

Nanoscale Synaptic Plasticity of Aspiny Interneuron Dendrites with Respect to Characteristic Fine Structures

by

Seth Arthur Weisberg

Dissertation

Presented to the Faculty of the Graduate School of

The University of Texas at Austin

in Partial Fulfillment

of the Requirements

for the Degree of

Doctor of Philosophy

The University of Texas at Austin

August 2018

Dedication

To Mom and Dad,

John and Jack,

Dean, John, and Bob,

and to Daniela

Acknowledgements

To fully acknowledge all the people who have helped me through this arduous and enlightening process would make the length of this dissertation inconsequential in comparison. I would like to thank past and present members of the Harris lab. Guan Cao for teaching me about physiology and conscientiousness. Masaaki Kuwajima for teaching me about effective laboratory practice, safety, dedication, and stoicism. John Mendenhall for teaching me microscopy and wisdom. Jen Bourne and Deb Watson for specimen preparation and tenacity. Heather Smith for reconstructing prowess and fortitude. Dusten, Dakota, and Lyndsey for their kind and helpful comments and suggestions in the preparation of this work. Thanks to Olga for many helpful comments and insights and instructions. And Patrick Parker (obviously a superhero alias) for material aid in data acquisition, presentation, and indispensable contributions to the drafting of this manuscript.

I would like to thank my excellent dissertation committee. To Dr. Boris Zemelman for teaching me more about how to be a scientist than I can express here. To Dr. Laura Colgin and Dr. Hiroshi Nishiyama for kindly sharing their considerable expertise in helping to make sense of this often-complex data. To Dr. Hans Hofmann for his guidance, experience, and deep insights on understanding and presenting science in a way that is intelligible and hopefully fun.

So many people have taught me what to do to be a good scientist, and equally important, what not to do. I want to thank the incredible Institute for Neuroscience and the Center for Learning and Memory for inviting me into their estimable ranks and supporting me in all seasons.

My most profound and everlasting thanks must go to my PI, Dr. Kristen Harris. All the virtues transmitted to me above emanate from Dr. Harris. Without the intercession of the more experienced, sturdy, and tempered members of the lab to focus these radiations, I would surely have burned away long before. I am now doubtlessly made of sterner stuff. Without her constant support and enthusiasm, I could not have succeeded. I am honored to have been accepted into her lab, and I will carry this honor with me wherever I may go.

With my face turned to heaven and Kannon, I take up the brush and begin to write at 3:30am on the 7th day of the 6th month in the year 2018.

Abstract

Nanoscale Synaptic Plasticity of Aspiny Interneuron Dendrites with Respect to Characteristic Fine Structures

Seth Arthur Weisberg, Ph.D.

The University of Texas at Austin, 2018

Supervisor: Kristen M. Harris

Abstract

Long term plastic changes in synaptic function have been reported in GABAergic inhibitory interneurons in the mammalian hippocampus, but structural changes associated with plasticity at the predominantly aspiny dendrites is not known. Aspiny dendrites are known to exhibit two distinct morphological types, smooth and varicose. Because of their rarity in neuropil, we reimaged tissue in which long-term potentiation (LTP) had been induced by theta-burst stimulation (TBS) in acute hippocampal slices from mature rat using the tSEM method to obtain sufficiently large fields, and we measured the response of aspiny synapses. We report significant changes in synapse size after potentiation induction in the slice that is influenced by the type of fine structure on which it occurs.

We developed quantitative methods to distinguish smooth from varicose aspiny dendrites and within varicose dendrites we found that the varicose and inter-varicose regions could respond differently to TBS. After potentiation induction in the slice synapse ultrastructure and mitochondria distribution changed in different directions in our two experiments but the relationship of synapse change and mitochondrial redistribution was consistent. In both experiments inter-varicose synapses significantly enlarged and were more likely to occur near mitochondria. In one experiment, varicose synapses enlarged and were associated with more mitochondria; in the other synapses did not change but were less likely to associate with mitochondria. In smooth type synapses, both experiments showed lower association with mitochondria and synapses either did not change or significantly decreased. Our findings of divergent ultrastructural changes among different aspiny dendrite regions may help to reconcile some of the disparate findings showing that similar stimulation protocols can lead to depressed or potentiated responses from inhibitory interneurons.

Table of Contents

List of Figures

Chapter 1: Introduction

The term *interneuron* describes inhibitory neurons that do not send axons beyond the local network (Freund & Buzsáki, 1996; Ramón y Cajal, 1904). Interneurons contribute to information processing by controlling or influencing the timing and routing of the flow of excitatory signals (Hayama et al., 2013; Lisman et al., 2018; Markram et al., 2011). For a system so heavily reliant on positive feedback loops, inhibition is necessary to prevent runaway excitation (Buzsáki & Mizuseki, 2014; Scheffer et al., 2009)—in animals, runaway excitation is an unfortunately common and potentially fatal condition known as epilepsy (Löscher, 2017). At a finer scale, interneurons conduct the synchrony of cell assemblies through their highly divergent outputs (Halasy et al., 1996) and even control the temporal precision of coincidence detection at discrete dendritic compartments of excitatory cells (Kullmann & Lamsa, 2011). Interneurons contribute information to the principal cells, which through their long-range projections turn an assembly of distinct networks into a brain (Buzsáki & Wang, 2012; Colgin et al., 2009; Lopez-Pigozzi et al., 2016). Not every interneuron is inhibitory and not every projecting principal cell is excitatory. In the hippocampus, a region of the brain strongly associated with episodic memory (Squire, 2009) and the subject of this dissertation, the interneurons are inhibitory and the principal pyramidal cells are excitatory (Freund et al., 1996).

Interneurons make up only ~10% of all neurons in the rodent hippocampus (Bezaire & Soltesz, 2013). Area CA1, the subregion of hippocampus from which our data was collected, is known to contain at least 23 distinct types of interneurons (Harris et al.,

2018). They exhibit extreme heterogeneity in morphology, molecular expression, membrane properties, and characteristic location of inputs and outputs (Harris et al., 2018; Klausberger & Somogyi, 2008). Despite such diversity they do share some common structural features that are distinct from the excitatory neurons. More than 80% of CA1 interneurons possess dendrites that completely lack spines (Scheuss & Bonhoeffer, 2013), specialized protrusions that are abundantly expressed on most types of principal cell dendrites and that host nearly all of the incoming excitatory synapses (Harris & Stevens, 1988). The pyramidal cells of Ammon's horn and the granule cells of the dentate gyrus are excitatory, projecting neurons with abundant dendritic spines (Fifková & Anderson, 1981; Lansing, 1984). In striatum, the principal cell is the medium spiny neuron, a projecting inhibitory cell with abundant spines (Gertler et al., 2008). This remarkable consistency in the structure of dendrites in neurons seems linked with their role—either as local information transformers or long-range transmitters.

Despite the majority of interneuron types' complete lack of spines, interneuron dendrites host a similar portion of excitatory synapses as pyramidal cells (Gulyás et al., 1999; Megías et al., 2001). Structural changes in spine properties, such as their size and frequency, are known to occur as correlates of learning and memory (Fifková & Van Harreveld, 1977; Matsuzaki et al., 2004). Spine size correlates with synapse area, an indirect but valid proxy for synapse strength (Bartol et al., 2015), and changes in synaptic strength are thought to be one of the major physiological processes identified with memory (Mayford et al., 2012).

ULTRASTRUCTURE

The mammalian brain operates over a range of spatial scales spanning 12 orders of magnitude, from ~$1x10^{1}$ meters to ~$1x10^{-10}$ meters. Relevant functions occur at all levels. At one extreme, individual neurons can traverse a distance of 30 meters in the spine of the blue whale (Smith, 2009). At the other extreme, the molecular organization of amino acid side chains that line the pores of ion channels are measured in fractions of a nanometer (MacKinnon et al., 1998). *Ultrastructure* is the term that pertains to the measurement of anatomical features with resolution around 1-10 nanometers or 1-10 billionths of a meter. Typical synapses in the hippocampus can vary in area by several-fold but lengths and widths around 200nm are not uncommon (Harris, 1994). Precise quantification of synapse area or discriminating the distance between synapses and subcellular structures is not possible with light microscopy, where resolution is limited by the wavelengths of visible light. The Abbe limit describes the minimum area on which light can be made to converge as a function of its wavelength (Abbe, 1873).

$$d = \frac{\lambda}{2n \sin \theta}$$

Equation 1. Abbe limit—d is the diffraction limit, which is the wavelength lambda divided by 2 times the refractive index n times the sine of the aperture angle, or equivalent to half the wavelength of the light. Structures smaller than ~200nm cannot be directly discriminated by optical microscopy.

Electron microscopy exploits the discovery by Louis De Broglie that particles with mass display wave-like properties (De Broglie, 1924). The wavelength is a function of their mass and velocity.

$$\lambda = \frac{h}{m * v}$$

Equation 2. The De Broglie equation. Lambda = wavelength; h = Planck's constant (6.6 X 10^{-27}); m = mass of the particle, for an electron (9.1 X 10^{-28} kg); v = velocity of particle.

The Abbe limit applies to electrons as well as photons. The velocity of an electron can be stated in terms the voltage, V, of an accelerating potential field, its kinetic energy will be equal to the energy of the field, that is eV (energy in electron volts) = V. For velocity significantly below the speed of light, the energy of the moving electron can be stated in terms of Einstein's equation, $e = mc^2$ where e is energy and c is the speed of light. So, $eV = 1/2mv^2$. Since *h* and *m* are constant, they can be rearranged to express the wavelength in terms of the accelerating voltage.

$$\lambda = \frac{1.23nm}{V^{1/2}}$$

Equation 3. Abbe limit for electrons. With an accelerating voltage of 100,000 V, the theoretical resolving limit is 0.24nm, assuming no aberration or distortion.

The wavelength of electrons allows discrimination of features smaller than 5nm and in our images structures like synaptic vesicles (~40nm) and the synaptic cleft

(~10nm) are clear. With this resolution we can make the precise measurements required to quantify the minute changes in ultrastructure that might occur as a consequence of our experimental manipulations.

FINE STRUCTURES

The excitatory synapses onto aspiny dendrites are structurally and biochemically quite similar to those on dendritic spines (Pelkey et al., 2017), though some subtle differences exist, and they share much of the machinery known to be important for expressing lasting, activity dependent plasticity. Experiments looking for evidence of long-term synaptic plasticity in hippocampal interneurons have returned an array of results, with the same stimulation protocols leading to disparate, even opposite, synaptic responses. One possible feature that might account for this variety is the largely unknown detailed distribution of the interneuron subtypes through the extent of the hippocampus. Rather than grappling with possibly dozens of distinct types, we sought to examine the structures they are known to have in common and measure how the induction of potentiation, measured by physiological changes in synaptic potentials in acute brain slice, might be expressed in the synaptic ultrastructure. Synapses on spines follow some regularities in response to functional plasticity; may there also be regularities in synapses that occur on the fine structures of aspiny interneuron dendrites?

What are these structures? Aspiny dendrites display certain conserved motifs in their morphology that seem to be common features regardless of the subtype (Gulyás et al., 1999; Scheuss & Bonhoeffer, 2014). Excluding the 20% that show sparse dendritic

spines, two characteristic patterns of fine structure have been observed—the smooth aspiny dendrite, and the varicose aspiny dendrite (Freund et al., 1996; Ascoli et al., 2008). The appearance of varicose dendrites under light microscopy has been referred to as *beaded*, implying alternating regions of higher and lower diameter. In such varicose dendrites, the often-extreme difference in geometry between varicose regions and the thin, constricted inter-varicosity segments suggests that treating them as distinct structures is worth investigation.

Access to high resolution over a sufficiently large area to measure the ultrastructure of enough synapses to draw valid inferences has previously not been technically feasible. Recent improvements in electron microscopy techniques (Kuwajima et al., 2013) has allowed us to reexamine tissue in which spiny synapses on pyramidal cell dendrites has been extensively characterized (Bourne & Harris, 2011). We know that interneuron dendrites in CA1 stratum radiatum receive the majority of their excitatory inputs from the Schaffer collateral axons (Freund & Katona, 2007a), the same axons supplying excitatory inputs to the adjacent pyramidal cell dendrites measured in this tissue. We therefore know that the aspiny dendrites in the same field received the same stimulation that induced robust potentiation in the slices and an increase in average synapse size on the pyramidal cell dendrites. The various plastic responses found in interneurons to similar stimulation protocols, might, at least in part, be accounted for by differences in the dendritic morphology on which synapses occur. Without the convenient proxy afforded by spines, electron microscopy is the only way to study these synapses quantitatively.

THE INTERNEURONS

Interneurons were first noticed by Santiago Ramon y Cajal in his observations of the human brain (Ramón y Cajal, 1904). He called these "neurons with short axons", noting they were "exceedingly numerous and can be considered peculiar to the human cerebrum…the functional superiority of the human brain is…linked with the prodigious abundance of unaccustomed wealth of forms of the so-called neurons with short axons" (Ramón y Cajal, 1989). Cajal's wealth of forms extends far beyond their morphology. Interneurons are characterized by numerous molecular expression patterns, some overlapping, some exclusive. Earlier interneuron classification schemes based on molecular expression divided them based on the expression of specific calcium binding proteins (Gulyás et al., 1991), parvalbumin (PV), calbindin (CB), and calretinin (CR). PV is encoded by the PVALB gene and is a low molecular weight (9-11kDa) albumin protein structurally related to calmodulin and troponin C. It is most concentrated in muscle tissue and shows high expression levels in numerous types of interneuron (Cates et al., 2002). Calbindin (formally calbindin 1, 28kDa) is encoded by the CALB1 gene and contains four active calcium binding domains. It is expressed in kidney, endocrine cells, at high levels in inhibitory neurons and at lower levels of a subset of principal cells (Kojetin et al., 2006). Calretinin (also known as calbindin 2 or 29kDa calbindin) is encoded by the CALB2 gene. It shares 58% homology with CB, contains six calcium binding domains, and is a member of the troponin C superfamily of calcium binding proteins. CR is rarely expressed outside the brain and its name derives from its discovery in the retina (Rogers, 1987). Of the three, only parvalbumin has not been found in any population of

hippocampal principal cell (Hu et al., 2014). Calbindin can be found in some pyramidal cells as well as dentate granule cells but at much lower concentration (Soltesz & Losonczy, 2018). Calretinin is expressed by pyramidal cells during development and in immature granule cells during adult neurogenesis (Brandt et al., 2003), and it is also found in mossy cells of the dentate. The nature of the "functional superiority" conferred by inhibitory interneurons, rather, the nature of the functions and computations they support, are currently topics of intense scrutiny.

DIVERSITY OF INTERNEURONS WITH DENDRITES IN HIPPOCAMPAL AREA CA1 STRATUM RADIATUM

Interneurons comprise 20-30% of all neurons in the neocortex (Markram et al., 2004) and ~10% in the hippocampus (Bezaire et al., 2013; Freund et al., 1996; Klausberger et al., 2008). In the hippocampal area CA1 alone, at least 23 distinct types of interneurons have been identified on the basis of features including, but not limited to: morphology, protein and peptide expression, location of soma, output specificity, input specificity, developmental origin, and electrophysiological properties (Bezaire et al., 2013; Chamberland & Topolnik, 2012; Defelipe et al., 2013a; Freund & Katona, 2007b; Geiger et al., 1997; Gulyás et al., 1996; Hu et al., 2014b; Igarashi et al., 2014; Jinno et al., 2007; Klausberger, 2009; Kullmann, 2011; Le Roux et al., 2013; Megías et al., 2001; Parent & Parent, 2018; Pawelzik et al., 2003; Pelkey et al., 2017a; Somogyi et al., 2012; Tyan et al., 2014; Wamsley & Fishell, 2017; Wierenga et al., 2010).

Interneurons are generally smaller than pyramidal cells in hippocampus and their soma can appear in a variety of shapes and in any strata. Their dendritic arbors are generally less elaborate than pyramidal neurons with fewer branches, particularly those that run parallel to pyramidal cell dendrites. An interneuron's morphology may not be a perfect proxy for its function, but the extremely non-random specificity of its inputs and outputs is suggestive. Three examples from CA1 will illustrate this.

Oriens-lacunosum moleculare (O-LM) cells have somata in stratum oriens (SO) and send dendrites horizontally which remain in SO. Their primary inputs are from the local collaterals sent from CA1 pyramidal cells. O-LM cells send typically one unbranching axon which makes no synapses until it extensively ramifies in stratum lacunosum-moleculare (SLM) and provides inhibitory inputs to the distal dendrites of pyramidal cells. Since their main excitatory inputs are provided by CA1 axons, which stimulate them to send inhibitory signals to the distal dendrites of the same pyramidal cells, they comprise an example of feed-back inhibition. This modest loop is particularly interesting as O-LM interneurons communicate information about the spiking activity of the CA1 cells themselves to their own electrotonically isolated remote dendrites. SLM is avoided by the Schaffer collateral (SC) axons and receives direct inputs from the entorhinal cortex. The main entorhinal input to hippocampus arrives at the dentate which passes the information via mossy cell outputs to CA3 which in turn sends this information via the SCs primarily to SR and SO. O-LM interneurons are thus able to monitor the responses of CA1 cells to the stronger SC inputs and control or influence the

comparison and integration of the transformed indirect entorhinal information with the direct inputs in SLM.

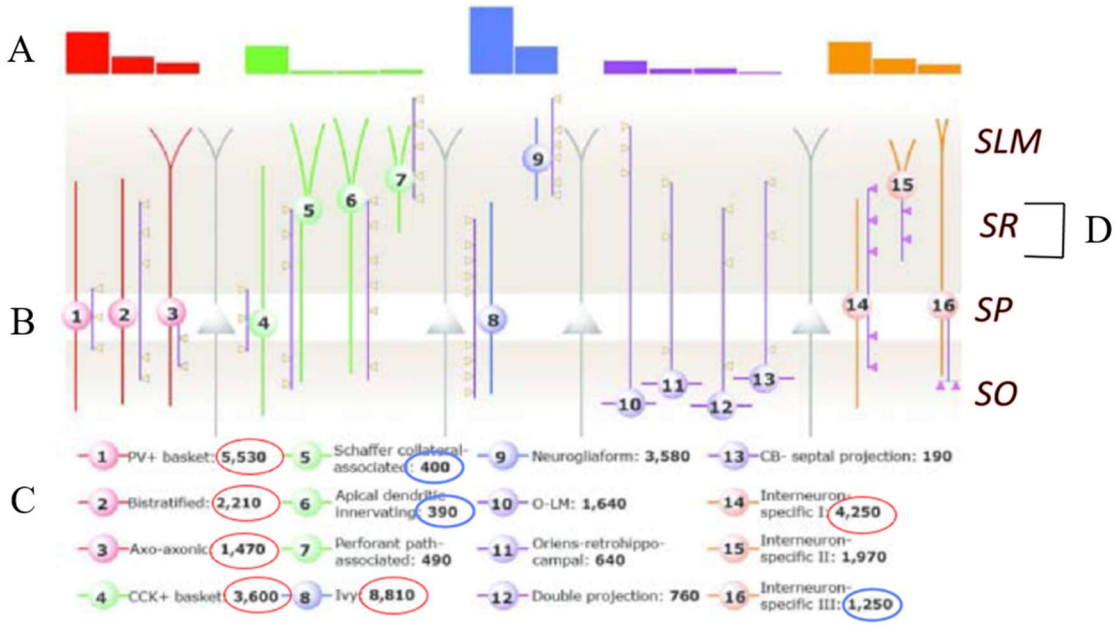

Figure 1. Adapted from Bezaire & Soltesz (2013 (A) Bars represent prevalence of the subtypes below. Red: PV. Green: CCK; blue: neurogliaform cells; purple: SST; orange: CR. (B) The characteristic location of their dendrites and axons. (C) Estimated number of cells. Red circles indicate the most likely source of interneuron dendrites SR. (D) Region of SR where our EM series were obtained.

Two other interneuron types demonstrate the difficulty of distinguishing subtypes by morphology alone using traditional staining techniques. Basket cells and axo-axonic cells appear superficially quite similar with somas in or immediately adjacent to the pyramidal cell layer, stratum pyramidale (SP). Basket cells have long aspiny modestly branched dendrites tending to reach all strata and an extremely dense axonal plexus restricted to SP. Axo-axonic cells have a similar appearance, though their basket is less dense. Only by electron microscopy or multiple immunofluorescent labeling does it become apparent that their targets are distinct—basket cells form 2-12 synapses each on pyramidal cell somata but avoid the axon initial segment (AIS). Axo-axonic cells in contrast form one synapse on each pyramidal cell and exclusively target the AIS (Bezaire et al., 2013).

Figure 1 shows estimated quantities of selected interneuron subtypes in rat CA1. Subtypes are shown with greater precision as to molecular marker expression. Ivy cells are now shown as the most prevalent individual type.

MOLECULAR MARKERS

A more thorough review of biochemical markers used to identify interneurons is useful. Interneurons are primarily characterized by the expression of gamma-aminobutyric acid (GABA), the main inhibitory neurotransmitter in the central nervous system (Gray, 1959). Hippocampal interneurons are grouped broadly into three classes based on expression of the calcium binding proteins mentioned above. These proteins tend not to overlap in their expression in different interneuron subtypes. While this is true

in hippocampus, populations of interneurons co-expressing PV and CB in human temporal lobe exist (Del Río & DeFelipe, 1997), and recently a small population of PV+/CB+ interneurons were found in mouse primary visual cortex (Gonchar, 2008).

Glutamatergic neurons transiently express calretinin during development, and during adult neurogenesis in the dentate sub granular zone adult born granule cells transiently express calretinin with a time course nearly identical to development, i.e., express calretinin for the first week then abruptly switch to expressing calbindin between 1 and 2.5 weeks post mitosis (Brandt et al., 2003; Kempermann et al., 2004).

More recent classification schemes account for the expression of many non-mutually exclusive peptides, enzymes, and receptors largely or entirely absent in principal cells (Pelkey et al., 2017a). The patterns and combinations of molecular markers can be used to distinguish different discrete types within larger CBP classes. The most studied additional interneuron markers are: cholecystokinin (CCK) (Harris et al., 1985), somatostatin (SST or SOM, depending on the author) (Köhler & Chan-Palay, 1982), vasoactive intestinal polypeptide (VIP) (Lorén et al., 1979), neuropeptide Y (NPY) (Finsen et al., 1992), and neuronal nitric oxide synthase (nNOS) (Hope et al., 1991). Hippocampal interneurons of any CBP class can co-express with any one or more of these or other less common molecular identifiers, though PV+/nNOS+ seem to only occur in dentate (Tricoire & Vitalis, 2012). To take a simplistic view, keeping in mind that this list of markers is not complete and that further distinctions can be made based on morphology and innervation pattern which often only weakly correlate with molecular expression, the possible combinations becomes large. With 3 CBPs and the 5 common

markers, simple combinatorics of (1 CBP + any combination of 5 markers) x 3 gives 1,386 unique combinations. Add just one more fairly common marker, such as reelin (Bezaire et al., 2013), and the number grows to 5,148. It is not the case that all possible combinations must occur, and some combinations are known to be significantly more rare than others or have not been found at all (Maccaferri & Lacaille, 2003).

Very little information about the ultrastructure of aspiny interneuron dendrite synapses is available, and none from tissue not specifically labeled for interneuron markers. One early study described the morphology of CCK expressing cells in all layers of hippocampus (Harris et al., 1985) using series of 25-45 sections each. Varicosities were noted but the term was applied to both axons and dendrites. Excellent pseudo-reconstructions along with some shorter 3DEM reconstructions were reported in a study of synaptic densities on dendrites from interneurons from PV, CB, and CR types (Gulyás et al., 1999). They noted mitochondria-filled varicosities and found PV+ dendrites had on average 5x more synapses than CB+ or CR+ dendrites. Aside from Mishchenko et al. (2010), a whole volume reconstruction in which two aspiny dendrites were partially reconstructed (fully reconstructed here), and Kasthuri et al. (2015), an impressive semi-automated full volume reconstruction from cortex in which the existence of 7 aspiny dendrites was noted, unlabeled reconstructions are not available.

Figure 2 shows the results of a novel clustering analysis based on several thousand single cell transcriptome analyses of CA1 interneurons (Harris et al., 2018). 49 clusters were confidently identified, but the authors entertained the idea that categorizing interneurons into types might not be appropriate, suggesting a continua model instead.

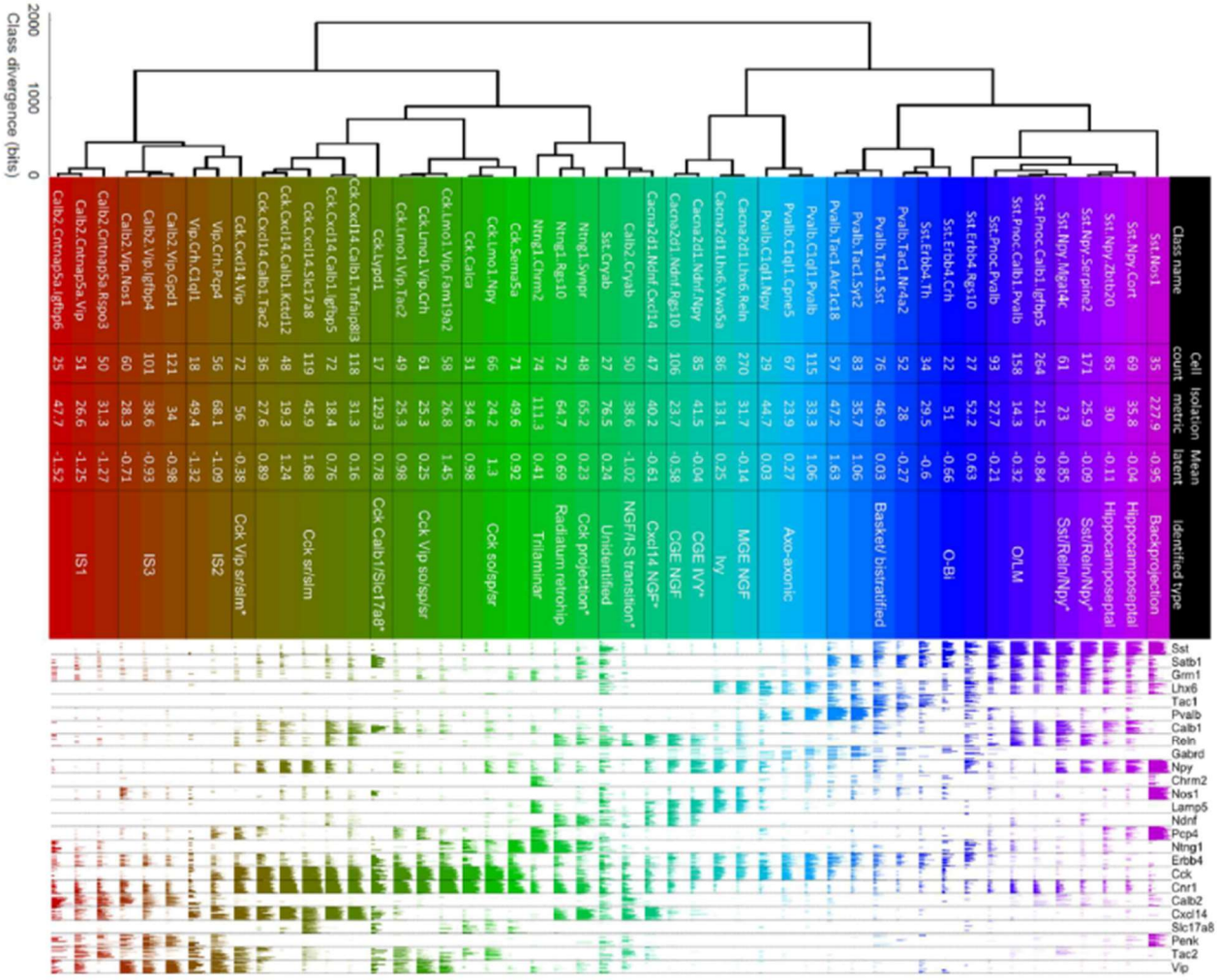

Figure 2. Adapted Harris et al. (2018). More recent cluster analysis based on single-cell transcriptomics of CA1 interneurons identified 49 clusters containing all the previously described subtypes, unifying 3 and finding evidence for an additional 8 previously unknown subtypes. Colors represent gradations of type and intensity of marker expression.

Rather than the few thousand types through combinatorics, they would have infinite types, or at least as many types as there are interneurons. Despite this formidable array of differences identified in interneurons, it is likely an underestimate of the true diversity of operations these cells can participate in.

Some interneurons are capable not only of simultaneously expressing different types of AMPA receptors in highly localized regions of their dendritic arbors, but can even dynamically change the identity and proportion of these receptors in response to activity (Tóth & McBain, 1998). Finally, though not detected yet in hippocampus, a population of VIP+ interneurons has been described in cortex that releases both GABA and acetylcholine (Granger et al., 2017). Though the authors were not able to determine if both transmitters are loaded into the same vesicles, they refer to several types of multi-transmitter neurons in striatum that co-express either glutamate (Glu)/GABA, dopamine (DA)/Glu, or DA/GABA, that can release either from the same vesicle or at distinct synaptic sites per transmitter.

PLASTICITY OF EXCITATORY INPUTS TO INTERNEURONS

Long-term potentiation (LTP) was demonstrated to occur in hippocampal interneurons by Buzsáki & Eidelberg (1982). In anesthetized rat, they identified interneurons as cells that had a spike width of <0.8ms and a spontaneous firing rate of 10Hz or higher, looking both in dentate and CA1. 8/11 identified interneurons displayed increased field potentials lasting up to 120 min (mean 30 min) in response to high frequency stimulation (HFS).

Progress was hampered by the still poorly understood heterogeneity of hippocampal interneurons. A notable negative finding, with the deceptively titled "Long-term potentiation in distinct subtypes of hippocampal nonpyramidal neurons," warned that LTP of pyramidal cells could lead to "passive potentiation" of interneurons detected by LFP (Maccaferri & McBain, 1996). Potentiation of pyramidal cells synapsing on interneurons could be mistaken for potentiation of the interneurons themselves. Their whole-cell and perforated patch recordings from interneurons described here yielded no detectible potentiation.

McMahon & Kauer (1997) described a novel form of plasticity in interneurons. Taking patch recordings from CA1 SR interneurons and delivering 100Hz tetanus to SC axons, they recorded normal potentiated field excitatory post synaptic potentials (fEPSPs) consistent with previous findings on HFS effects in slice but remarkably detected robust LTD (interneuron LTD or iLTD) in the whole-cell patched interneurons. By patching nearby pyramidal cells, they confirmed potentiated EPSP/EPSCs and depressed EPSP/EPSCs in their interneurons and the typical potentiation of fEPSPs. Even more remarkably, they determined that the iLTD induced in interneurons, unlike that in pyramidal cells, did not display input specificity. Using a spaced two electrode design, they showed that the potentiation in patched pyramidal cells was pathway specific, but the depression in interneurons was not. Of cells recorded, 65% of interneurons expressed iLTD and all were filled with biocytin for morphology analysis. Anatomically they identified two types of interneuron which they identified with basket and bipolar cells.

No correlation with iLTD was found between anatomical type and probability of expression.

These results were elaborated by Gibson et al. (2008), using the same methods as McMahon & Kauer (1997). They found the non-specific iLTD was NMDA receptor independent and required presynaptic activation of TRPV1 receptors, as blocking them or using knockout mice lacking TRPV1 failed to express iLTD. Further, they identified the endogenous ligand to be produced by the interneurons themselves—activation of G-protein signaling from post synaptic group I metabotropic glutamate receptors (mGluRI) led to a lipoxygenase dependent production of an eicosanoid metabolite of arachidonic acid acting as a retrograde messenger activating presynaptic TRPV1 receptors. Notable was the finding that even completely blocking all intracellular processes involved in synthesis of the retrograde messenger did not completely occlude all HFS induced iLTD in the patched interneurons. They hypothesized either spillover from other nearby interneurons could activate presynaptic TRPV1Rs sufficiently to induce LTD on other interneurons, or, alternatively, "perhaps the heterogeneity of hippocampal interneurons could account for these data." These recordings were also performed in whole-cell configuration.

Though interneurons share many properties with principal cells relevant to plasticity like expression of NMDA and MGluRs (McBain & Fisahn, 2001), they also display important differences. It was shown that hippocampal interneurons do not express calcineurin or CaMKIIa, though they do express CREB (Washburn et al., 1997). The lack of the CaMKIIa signal pathway together with interneurons' lack of dendritic spines,

tendency to express calcium-permeable AMPA receptors (CP-AMPAR), and heterosynaptic LTD led some to conclude that interneurons were unsuitable to support activity dependent plasticity (McBain et al., 1999). Activity dependent synaptic plasticity is also called Hebbian plasticity, after the Canadian psychologist Donald O. Hebb who clearly described the process in his book *The Organization of Behavior* (Hebb, 1949). The hallmark of a Hebbian process is that coactivation of two neurons, A and B, is such that if the firing of A consistently takes part in causing B to fire, some metabolic or other change will occur, so A's firing becomes more likely to cause B's firing.

The ability of interneurons to precisely restrict calcium transients was shown by Goldberg et al. (2003), indicating that spines might not be necessary for physically constraining calcium. NMDAR-independent LTP was shown in oriens dwelling CA1 interneurons (Perez et al., 2001). NMDAR-dependent LTP was shown in rat CA1 SR-dwelling interneurons (Lamsa et al., 2005) that was pathway specific, demonstrating for the first time that interneurons are capable of homosynaptic plasticity and spines are not required for Hebbian input discrimination; interestingly, only ~50% of recorded interneurons expressed LTP while the rest were resistant to all stimulation paradigms attempted. Further, Lamsa et al. (2007) showed similar NMDAR-dependent LTP in ~50% of recorded CA1 SR interneurons in αCaMKII-T286A mutant mice. The αCaMKII-T286A mutation prevents autophosphorylation and completely occluded LTP in pyramidal neurons without affecting interneuron LTP. Broad spectrum CAMK inhibitors blocked LTP in both interneurons and pyramidal cells in WT mice, suggesting interneurons use some other isoform of CAMKII.

A novel form of LTP, dubbed anti-Hebbian LTP, was described and shown to depend on CP-AMPARs (Lamsa et al., 2007). Anti-Hebbian plasticity should not be confused with LTD. LTD is a Hebbian process, that is, defined by activity dependent synaptic strength modification, positive or negative. The requirement to be Hebbian is that presynaptic neuron activation lead to postsynaptic activation. If the frequency of the presynaptic cell is low, LTD may result, if fast, LTP. Anti-Hebbian is the modification of synaptic strength as a consequence of presynaptic activation and post-synaptic inactivity. The release of presynaptic glutamate binding to postsynaptic receptors while the post-synaptic cell is hyperpolarized can lead to potentiation by this Anti-Hebbian mechanism. NMDARs are biophysically suited for coincidence detection/association aspect of Hebbian plasticity as they pass calcium only when there is sufficient depolarization to remove the magnesium block. CP-AMPARs are blocked by negative polyamines at depolarized potentials and allow calcium influx when the presynaptic terminal releases glutamate and the postsynaptic terminal is hyperpolarized or inactive. Thus, NMDARs are often thought of as a logical AND operation, one type of coincidence detector where input from $x_i \ldots x_n$ AND postsynaptic activity are required together within some window of space or time. The biophysical properties of CP-AMPARs are analogously equivalent to a logical NAND (not AND) operation, a different coincidence detector requiring inputs $x_i \ldots x_n$ AND NOT postsynaptic activity. Although the idea of anti-Hebbian plasticity had been proposed before (Lisman, 1989), the mechanism described by Lisman was a calcium concentration-dependent differential set of phosphorylation states of the ~30 sites on CaMKII. This precise mechanism cannot be ruled out in this interneuron

experiment. Though interneurons do not express alpha-CaMKII, they do express other CaMKs. The inverted coincidence detection by CP-AMPARs with respect to NMDARs was convincingly demonstrated by injecting a sinusoidal current into the patched interneuron and stimulating the axonal inputs either at the peak of the sinusoid (during depolarization) or at the trough (during hyperpolarization). Potentiation only occurred when stimulation coincided with the trough; no change in synaptic potentials occurred when paired with the peak.

An inability of interneurons to undergo Hebbian synaptic scaling with similar temporal dynamics to principal cells is inconsistent with empirical data and theoretical models of local network function (Mariño et al., 2005; Pouille & Scanziani, 2001). Failure to undergo persistent adjustments in synapse weights parallel to those at excitatory-to-excitatory connections would lead to progressive deteriorating integration timing of both principal cell and interneuron dendrites and somata. Healthy brain exhibits dynamically metastable oscillatory synchrony *in vivo,* detectible as shifts in phase and spectral power; interference with LTP via NMDA antagonists is known to alter multiple intrinsic hippocampal oscillations (Deco et al., 2017; Kalweit et al., 2017; Tognoli & Kelso, 2014).

The importance of LTP in inhibitory circuit elements was shown empirically by examining the effects of inhibition on pyramidal dendritic integration (Lamsa et al., 2005). In their study of Hebbian LTP in CA1 radiatum interneurons, Lamsa et al. (2005) also investigated the functional consequences of LTP at glutamatergic synapses onto inhibitory dendrites for network function and computation. They first used gramicidin-

patched pyramidal cells and stimulated independent SC inputs to its dendrites. Simple measurements of dendritic integration can be obtained by adjusting the temporal delay of stimulation at each path and measuring the probability of spiking with respect to the time delay. Stimulation intensity was set so that synchronous stimulation resulted in a 50% spike probability, measurements at non-zero intervals and in the presence of picrotoxin were normalized to the zero-delay probability. Spike probability fell off rapidly as the interval was increased in 2ms steps to ±20ms, reaching less than 5% at the longest intervals. When feed-forward inhibition was blocked with the GABA-A receptor antagonist picrotoxin, spike probability exceeded 100% for intervals close to zero and remained >50% at ±20ms. This confirmed the importance of inhibition for temporal input discrimination. To examine the role of LTP at glutamatergic synapses on interneuron dendrites, they induced LTP only at the patched pyramidal cells by pairing postsynaptic depolarization with low-frequency afferent stimulation of one pathway. Since low-frequency stimulation alone cannot induce LTP in interneurons, excitatory synapses on the pyramidal dendrites potentiated without potentiation of excitatory synapses on their downstream feed-forward inhibitors. They found that after pyramidal-only LTP the integration window expanded significantly, from high probability at 0ms interval and almost zero probability beyond ±1ms to nearly equal probability in the range of ±6ms. If LTP was induced by simultaneous high-frequency stimulation of both pathways, synapses on both pyramidal cells and interneurons could potentiate. In this situation, there was no significant difference in spike probability at different intervals between pre- and post-LTP induction.

The questions of if, why, and how interneurons express synaptic plasticity are more than curiosities. The adaptive responses of inhibitory cells play fundamental roles in shaping nearly all aspects of neuronal network activity and computation (Kullmann et al., 2011).

What are the ultrastructural correlates of plasticity at the more common excitatory shaft synapses on aspiny interneurons? Are there any? Though known to functionally exhibit lasting potentiation and depression, very little is known about the anatomical basis of such changes. Many of the questions relevant to how plasticity is structurally expressed in excitatory cells reappear for interneurons. For example, does LTP cause an increase in the number of synapses or the splitting of synapses (Fiala et al., 2002), or another anatomical reorganization (Bell et al., 2014; Bourne & Harris, 2007; Bourne & Harris, 2011a)? Without the guidance afforded by the spine, structures known to increase or decrease in size or volume in response to potentiation or depression that can be used as a proxy for synaptic strength (Bartol et al., 2015; Harris & Kater, 1994; Matsuzaki et al., 2004), structural changes at aspiny regions might be even more subtle. Synapse size could increase or decrease (Bourne et al., 2011a), synapses might shift location along the aspiny regions, or subcellular organelles like mitochondria may reorganize to support intracellular signaling or increased energy demand important for maintaining functional changes.

Recent advances in opto- and pharmacogenetic manipulation are making it possible to selectively activate or inactivate specific populations with increasing resolution (Basu et al., 2016). Patch recording was used in most of the studies on

interneuron plasticity, but run-down of potentiation, a phenomenon well-known in excitatory cells thought to be caused by the dialysis of some important cytosolic factor by the pipette media, prevents the induction of plasticity, especially if it does not occur quickly after breakthrough (Malinow & Tsien, 1990). The situation is exaggerated in interneurons (Lamsa et al., 2005b), and many investigations using whole-cell configurations yielded conflicting findings (McBain et al., 1999). Perforated patching with gramicidin allows more stable and longer duration single cell recordings (Kyrozis & Reichling, 1995) and has been used successfully in studying interneuron plasticity (Lamsa et al., 2007). However, even with perforation, significant deviations from baseline are seldom reported beyond 40 minutes. Perforation also prevents filling recorded cells with large molecules for post-hoc histological analysis.

The Petilla Interneuron Nomenclature Group identify the three types of dendrites already mentioned: fairly regular and aspiny, irregular and spiny, or beaded and aspiny (Ascoli et al. 2008; Figure 3). Although all three types were found in our dataset, only 4 dendrites could be called irregular spiny and will not be included in the analyses. The term *beaded* will not be used here to refer to the dendrites with clear regions of increased volume and surface area. We chose not to use the term *beaded* due to past negative associations of beading as artifacts of fixation (Gulyás et al., 1999). Rather, we will use the term *varicose*, which has been applied to this morphology in several regions of the brain (Freund et al., 1996; Kawaguchi & Kubota, 1993; Kita et al., 1990). Although the term *varicosity* is often used in the literature on interneurons in reference to their axons (Pelkey et al., 2017), we do not believe using this label here in reference to dendrites will

cause any confusion. Varicose aspiny dendrites have constricted regions between the varicosities which we have called *inter-varicosity regions*. We refer to aspiny dendrite segments without varicosities simply as *smooth*.

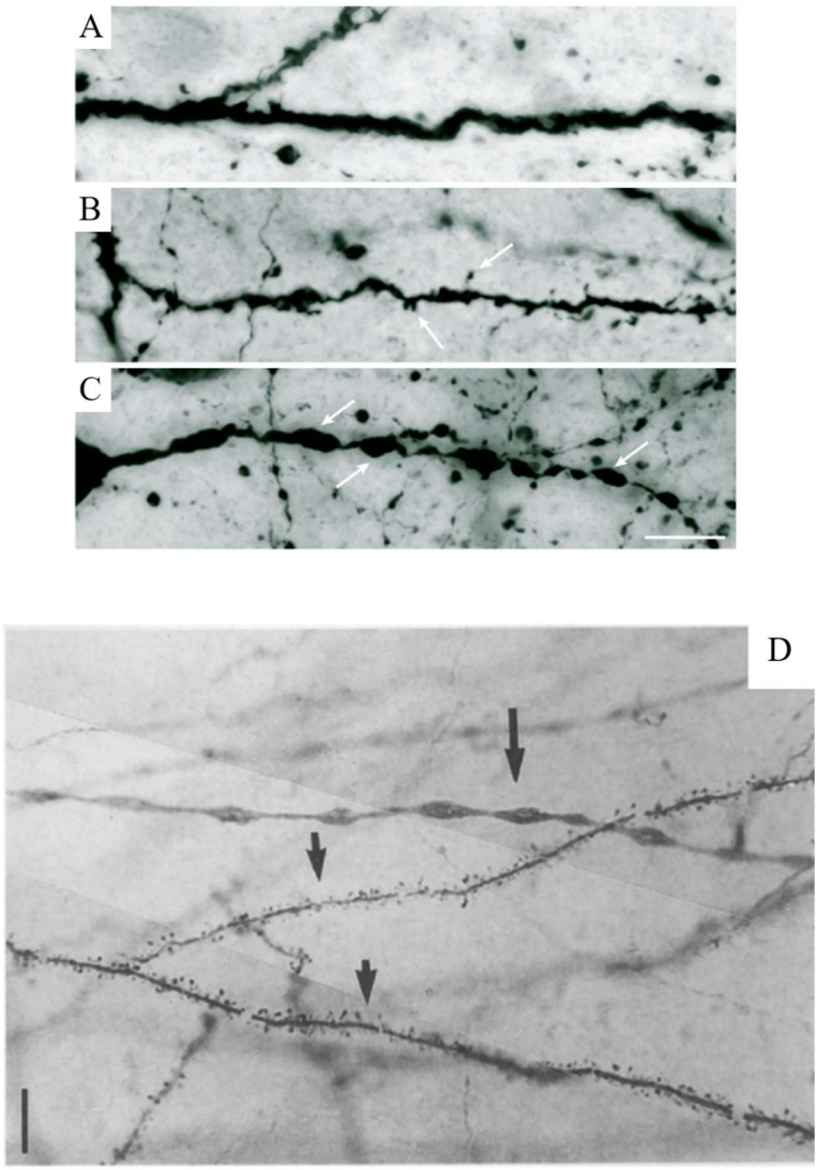

Figure 3. Light microscopy images of recognized fine structures in interneuron dendrites. Adapted from Ascoli et al. (2008). (A) Smooth aspiny dendrite. (B) Sparsely spiny interneuron dendrite. (C) Beaded dendrite, white arrows show sparse spines in (B) and beads in (C). Scale bar for (A-C) is 10µm. (D) Megías et al. (2001). Image takes ~100µm from SP, spiny pyramidal cell dendrites (short arrows) are easily distinguished from aspiny interneuron dendrites (long arrow). Note their varicose appearance. Scale bar, 10µm.

Chapter 2: Methods

PHYSIOLOGY

400 μm thick hippocampal slices were prepared from two young adult male Long Evans rats, animal 1 and 2 (60 days and 61 days old, weighing 323 and 319 g, respectively). Animals were anesthetized with halothane, brains removed, and the hippocampus was quickly chopped using a Stoelting tissue chopper at room temperature (~25C) and placed in wells containing artificial cerebrospinal fluid (ACSF) composed of (in mM): 116.4 NaCl, 5.4 KCl, 3.2 $CaCl_2$, 1.6 $MgSO_4$, 26.2 $NaHCO_3$, 1.0 NaH_2PO_4, and 10 D-glucose. Slices were transferred immediately to filter-paper nets positioned over wells containing ACSF at the interface of humidified O_2 (95%) and CO_2 (5%) and were maintained at 32ºC for an average of 3 h (range: 2.25–3.5 h) *in vitro* before the onset of the recordings. Total time from decapitation to placing slices on the nets was 6 min 21 s and 6 min 19 s. Two concentric bipolar stimulating electrodes (100 μm outside diameter, Fred Haer, Brunswick, ME) were located 300–400 μm on either side of a single extracellular recording electrode placed in the middle of stratum radiatum (glass micropipette filled with 120 mM NaCl) for a total separation of 600–800 μm (Figure 4). A distance of 400 μm between stimulating electrodes is sufficient to stimulate independent populations of inputs to CA1 pyramidal neurons (Ostroff et al., 2002; Sorra et al., 1998). Extracellular field potentials were recorded using IGOR PRO software (WaveMetrics, Lake Oswego, OR). Extracellular field potentials at the recording electrode were acquired by an AxoClamp 2B (Axon Instruments, now Molecular Devices

LLC, San Jose, CA), passed to a Brownlee 410 precision amplifier (Brownlee, now NeuroPhase), then to a National Instruments BNC-2090 AD converter (National Instruments, Austin, TX) with a sampling rate of 10kHz. The slope (mV per ms) of the field excitatory postsynaptic potential (fEPSP) was measured for 400 μs along the steepest segment of the negative field potential beginning 170–250 μs after the stimulus artifact and measured at the same position before and after LTP induction. An input–output (I/O) curve determined the range of responsiveness of the slices and the stimulus intensity was set just below population spike threshold and held constant throughout the remainder of the experiment. Stimulations were alternated between the control and TBS electrode once every 2 min at a 30 s interval between electrodes.

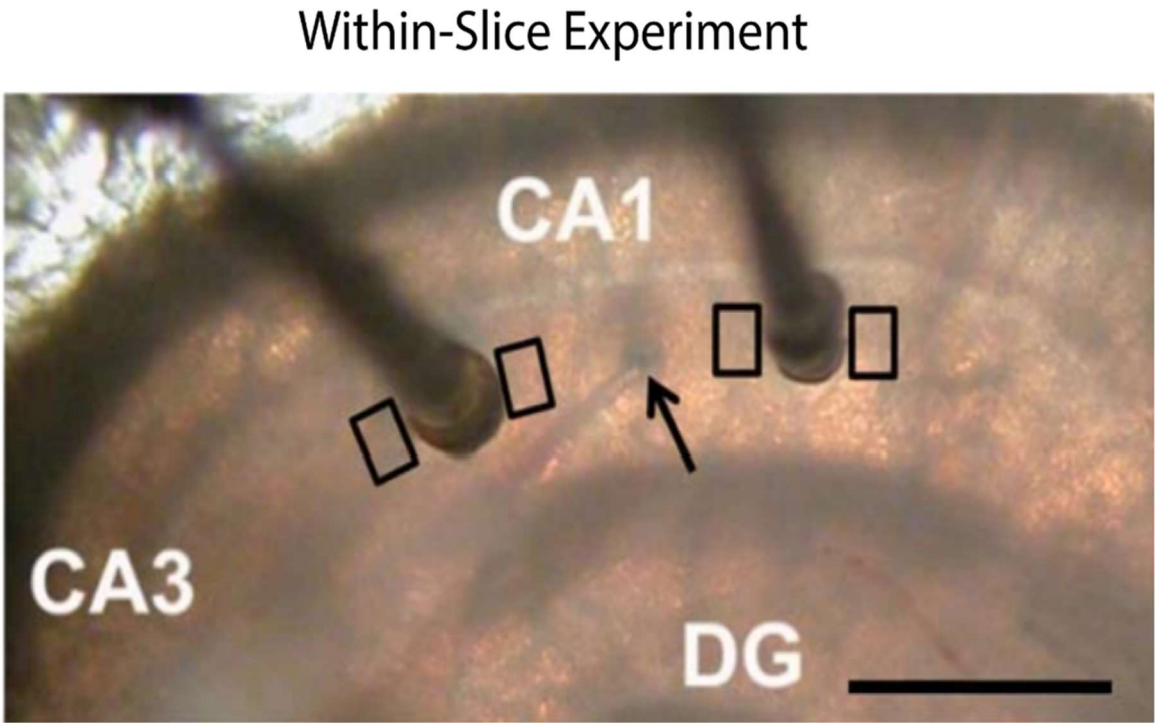

Figure 4. Image showing the configuration of the two-electrode within-slice control paradigm for LTP induction. Recording electrode (black arrow) placed in middle CA1 stratum radiatum equidistant between control and theta burst-delivering electrode. Black boxes show location of tissue collected for serial sectioning and analysis, scale bar = 0.5mm, adapted from Bourne & Harris (2011).

TBS-LTP

One slice was used per animal. A stable baseline was established for at least 30 min (Figure 5) before theta burst stimulation (TBS) (8 trains of 10 bursts at 5 Hz of 4 pulses at 100 Hz delivered 30 s apart, requiring 3.5 min in total) (Figure 6) was delivered to one stimulating electrode while the control electrode received no TBS stimulation. The

positions of the control and TBS-LTP electrodes were alternated between the proximal (CA3) and distal (subicular) side of the recording to balance any effect that might occur as a function of distance from CA3. Responses from the control and TBS stimulating electrodes were monitored for 2 h after the first train of TBS. Tissue was fixed and processed for electron microscopy only for slices demonstrating stable physiological responses and sustained potentiation.

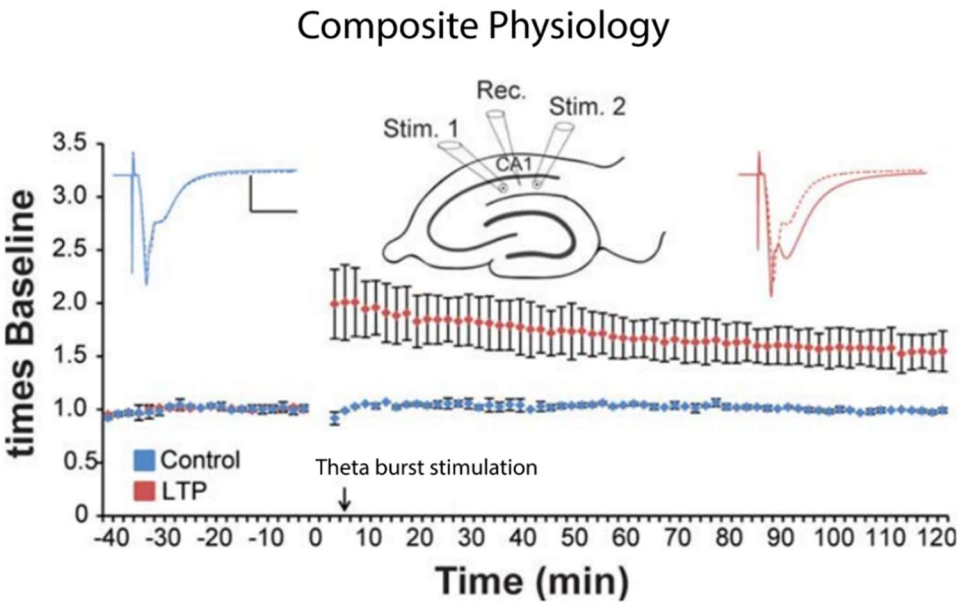

Figure 5. Composite physiology recorded from the slices used in this experiment. Control side shows no change from baseline for the duration of the 2-hour recording post-induction (blue dots, top left blue inset traces show averaged field EPSPs before (dotted blue line) and after (solid blue line) LTP induction at the other electrode). LTP side shows significant and persistent increase in field EPSP slope lasting until experiment was terminated and rapidly preserved (red dots, top right red inset traces show averaged field EPSPs before (dotted red line) and after (solid red line) TBS-LTP), image adapted from Bell et al. (2014).

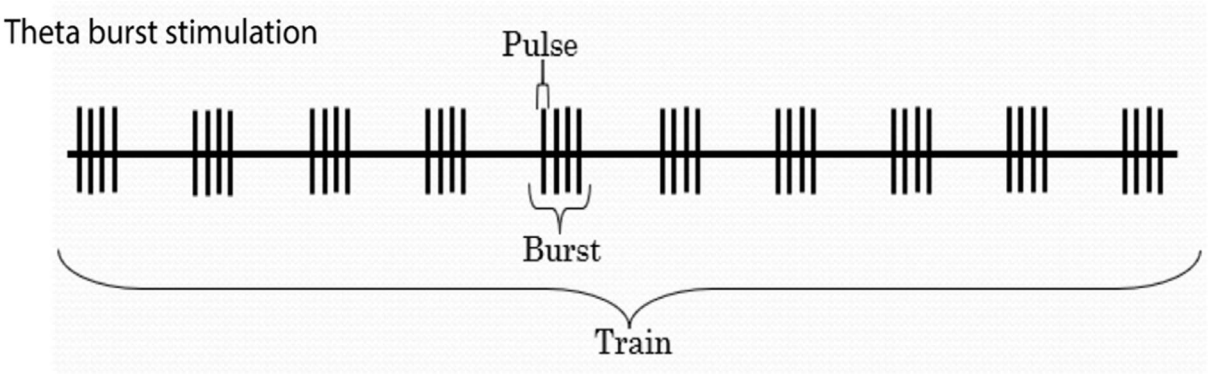

Figure 6. Schematic of theta-burst paradigm. 8 trains delivered with ISI of 30 seconds. A train consists of 10 bursts (ISI of 200ms) at 5Hz, each burst consists of 4 pulses (ISI of 10ms) at 100Hz. Adapted from Gao & Harris (2012).

FIXATION AND PROCESSING FOR SSTEM

Slices were preserved within a few seconds after the end of each experiment using rapid microwave enhanced fixation (Jensen & Harris, 1989). See Harris et al. (2006) for detailed description of the process and Figure 7 to see the steps involved.

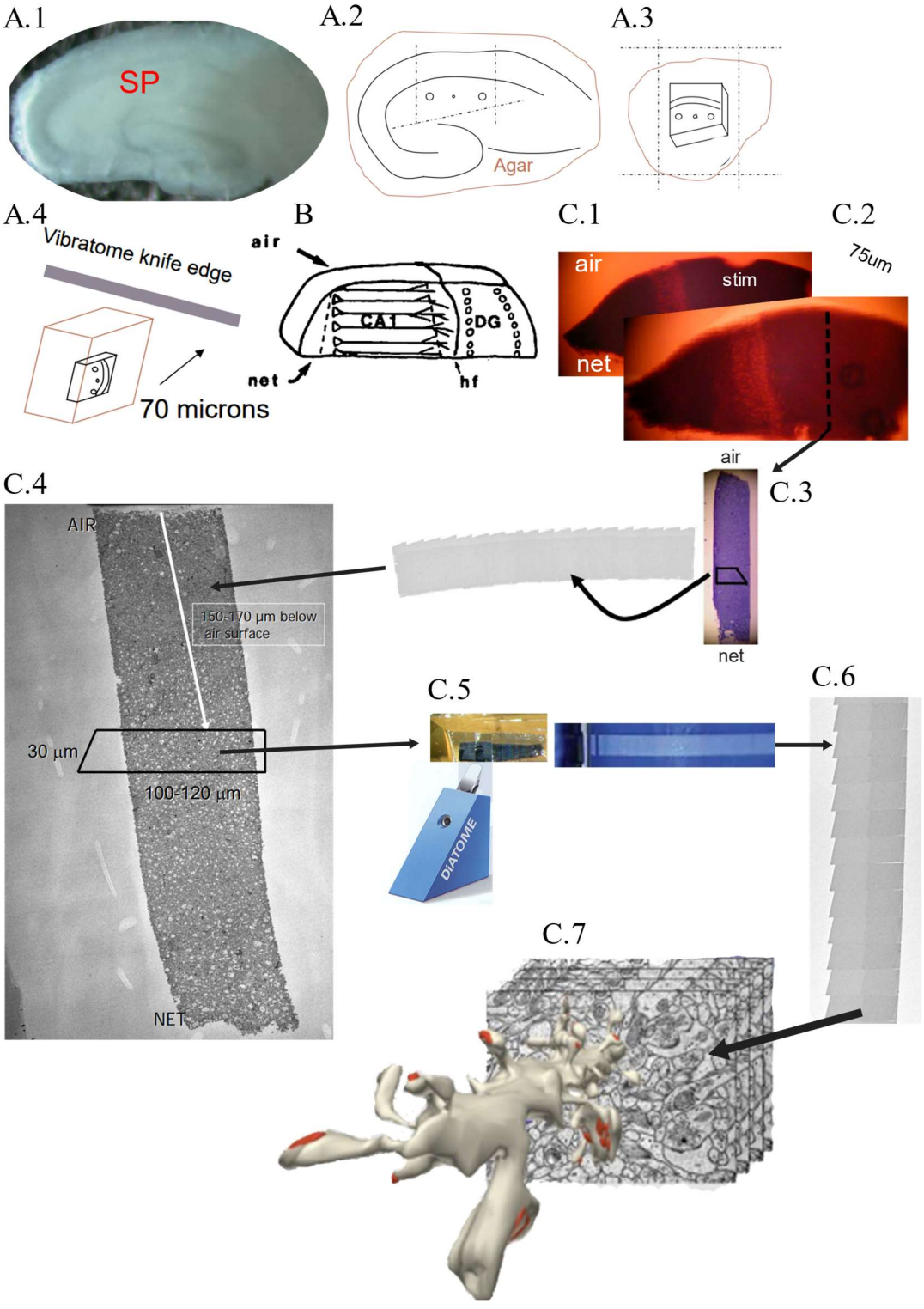

Figure 7. EM prep, cutting, and section acquisition.

Figure 7. EM prep, cutting, and section acquisition. (A.1) Slice after rapid microwave-enhanced fixation still on interface chamber net, red line is pyramidal cell layer of CA1. (A.2) Diagram of slice embedded in agarose (orange line) with region of interest containing stimulation electrode positions (large circles) and recording electrode (small circle) enclosed in dashed lines. (A.3-4) Region re-embedded in agarose and positioned for vibratome sectioning perpendicular to transverse axis of hippocampus. (B) Diagram of 70µm vibrasection, pyramidal cells and apical dendrites visible (hf, hippocampal fissure). (C.1-2) Vibrasections embedded in epoxy resin. (C1) Section containing depression left by stimulating electrode, (C2) adjacent section without compression from electrode, dashed line shows location for test thin slicing. (C.3) Toluidine blue-stained thick section is used to guide placement of cutting region. (C.4) Test thin image used to assess tissue quality, trapezoids identify region for serial thin sectioning. (C.5) Vibrasection embedded in epoxy with trimmed trapezoid containing region of interest positioned over diamond knife, to the right is a ribbon of ultrathin sections cut on a different diamond knife floating on water. (C.6) Low magnification TEM image of 12 serial sections. (C.7) Schematic of the reconstruction process using serial sections with partially 3D reconstructed dendritic segment emerging. (A) and (C) adapted from Harris et al. (2006) and (B) adapted from Jensen & Harris (1989).

HIGH QUALITY

Test thin (Figure 7.C.4) sections spanning the depth of the slice from air to net surface were evaluated from each experiment. Only those slices with a band of high quality tissue preservation spanning a depth of at least 100 μm were included in these analyses.

REIMAGING THE TISSUE

The sections used in this study were first cut and photographed in 2004. Series from this tissue has been used before to find novel ultrastructural consequences of LTP in pyramidal cell dendrites (Bell et al., 2014; Bourne et al., 2011a; Chirillo et al., 2015). Epoxy embedded serial ultrathin sections are extremely durable when properly stored. Unlike other methods for obtaining nanometer scale volumetric data of brain tissue such as serial block-face and focused ion-beam milling (Helmstaedter et al., 2008), serial sectioning does not destroy the sample. Rather, high quality tissue obtained at significant labor is preserved, awaiting the development of more advanced tools.

The primary impediment to EM reconstruction of unlabeled interneuron dendrites in hippocampal neuropil was articulated in the first paper to report plasticity in hippocampal interneurons (Buzsáki et al., 1982). The pyramidal cells make up 96-98% of the neuropil of Ammon's horn. The series we used for reconstruction had previously been imaged with a transmission electron microscope (TEM) with individual section fields of around 8x8 μm. Of the 11 original TEM series, containing regions from the LTP and control regions of both two-hour slices, 4 aspiny dendrites were found. Existing serial

sections were reimaged on scanning microscope in transmission mode, see Kuwajima, Mendenhall, & Harris (2013) for detailed description of the imaging protocol. tSEM yielded four series with field sizes of ~50x50 µm. From these we reconstructed 60 aspiny dendrites to determine whether ultrastructural modifications occur at excitatory synapses onto these interneuron dendrites two hours after the induction of LTP.

From other published data (Mishchenko et al., 2010) we were able to find 4 comparable aspiny dendrites from perfusion-fixed tissue from a similar region in adult rat hippocampus. Perfusion-fixed brain is considered as a benchmark for ultra-anatomy (Roberts et al., 1990). Direct introduction of aldehyde fixatives to the brain via trans-cardial perfusion preserves native structure, as traumatic brain injury is avoided. Room temperature chopping and sufficient recovery time in an interface chamber resulted in ultrastructure not significantly different from perfusion fixation in the 2 hour control regions for pyramidal cell dendrites (Bell et al., 2014). These data allowed comparison between control dendrites and non-sliced, unstimulated perfusion-fixed dendrites. Series ranged from 50-204 serial sections with thicknesses from 49nm-56nm. Figure 8 (red box overlaps with Figure 9) shows a tSEM field (50x50µm) imaged from the same section that was earlier imaged with TEM. Figure 10 shows the adjacent serial section to Figure 8 in which 14 aspiny dendrites were found. We counted 350 spiny dendrites in this image, so 4% of dendrites were aspiny, in agreement with the earlier estimation. Figure 11 shows the region captured on TEM in Figure 9 but here shown in its tSEM image at the same scale, no aspiny dendrites were found in this smaller field.

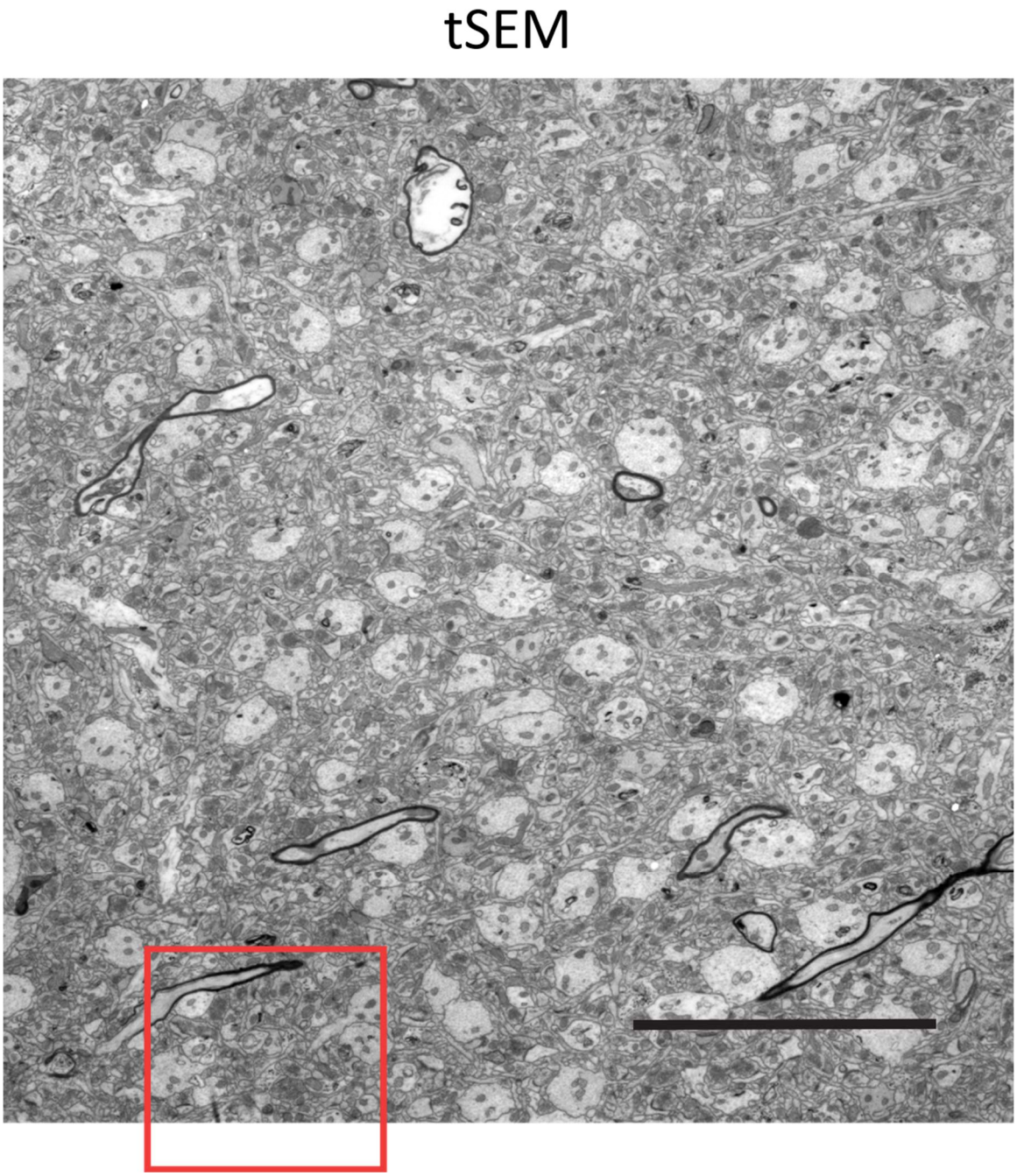

Figure 8. tSEM image acquired in 2016 partially containing region shown in Figure 9 (red square). Scale bar = 10µm. Pixel size = 2.09nm.

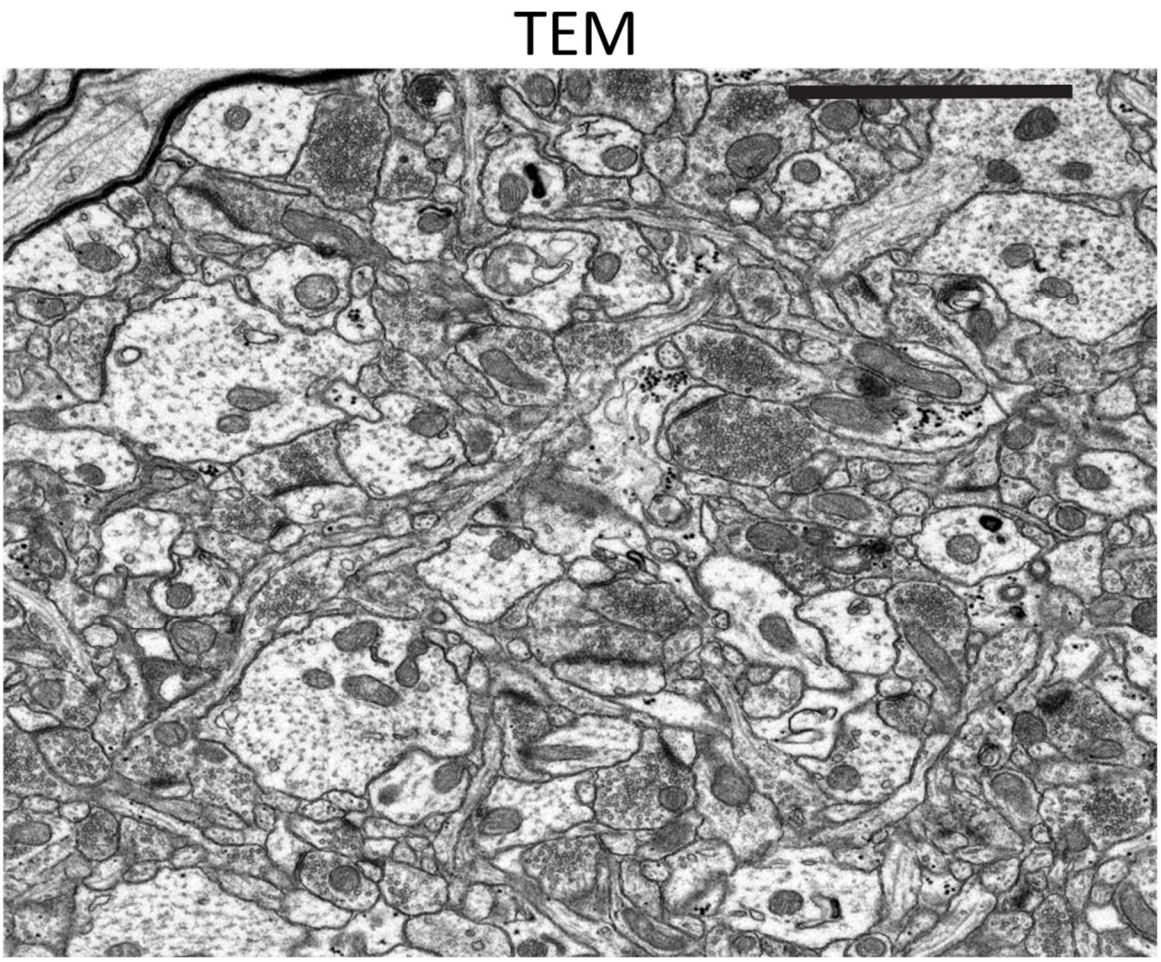

Figure 9. TEM image showing part of the same physical section in Figure 8. Image acquired in 2008. Scale bar = 2.5µm. Pixel size = 2.23nm.

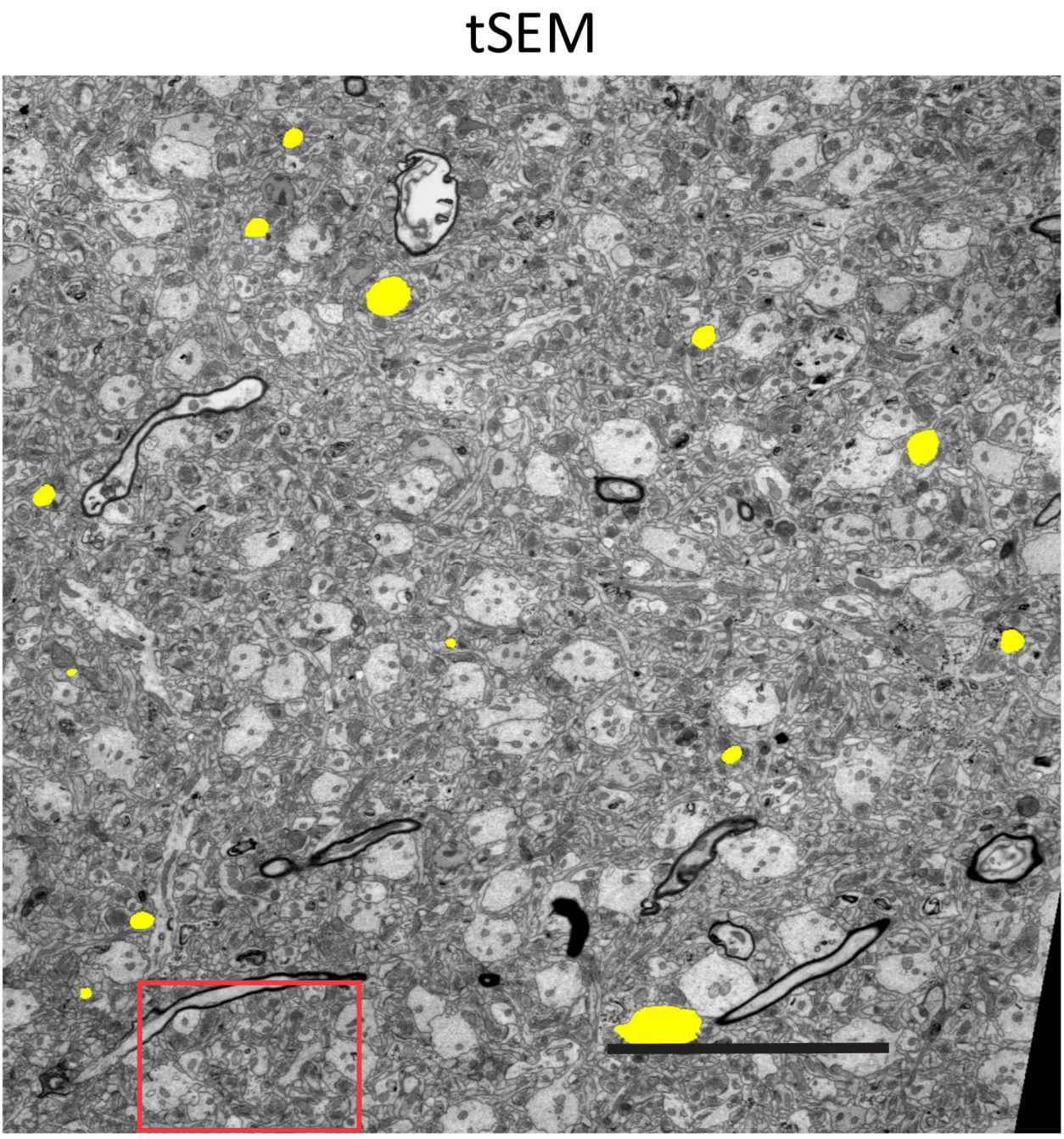

Figure 10. The adjacent tSEM serial section to Figure 8, all aspiny dendrites highlighted in yellow. Red square contains Figure 11. Scale bar = 10µm. Pixel size = 2.09nm.

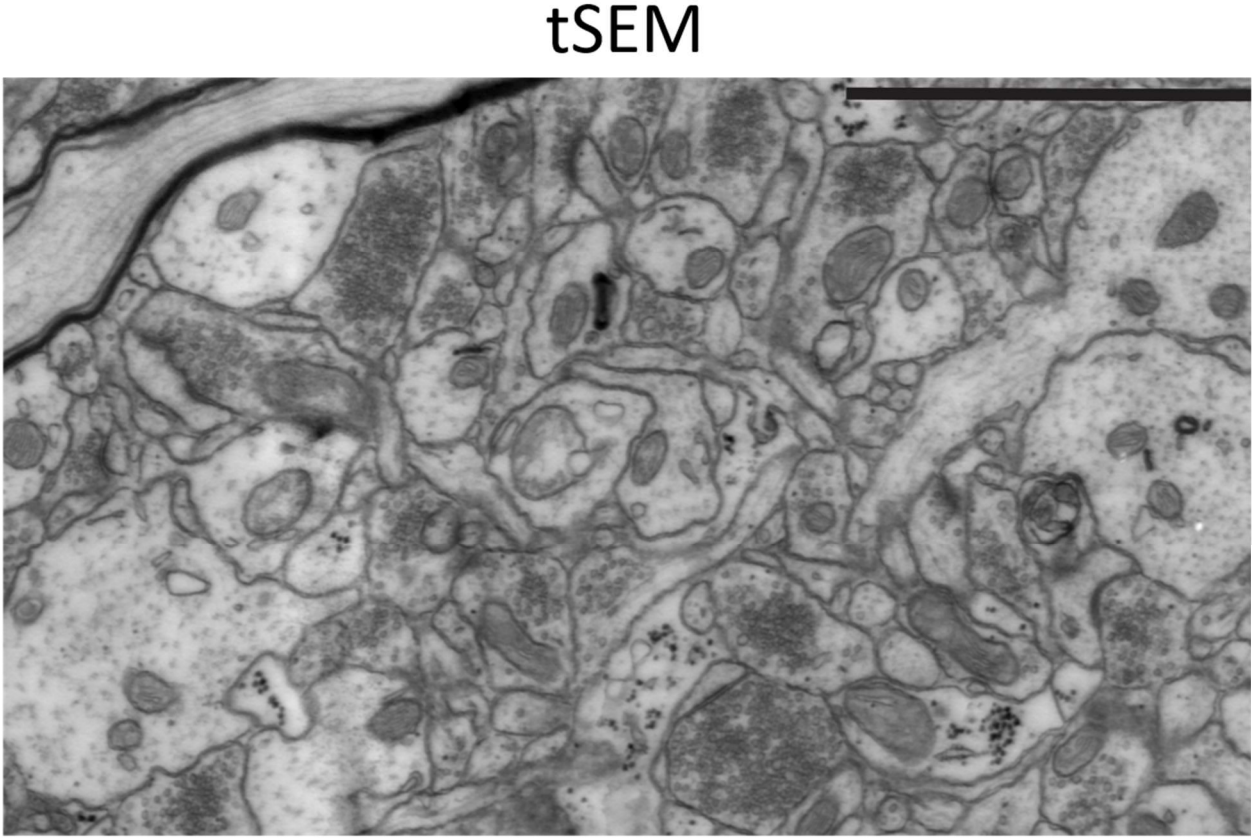

Figure 11. Field from Figure 10 red square enlarged to show no resolution loss by the tSEM compared with TEM. Scalebar = 2.5µm. Pixel size = 2.09nm.

THREE DIMENSIONAL RECONSTRUCTIONS AND MEASUREMENTS

Images from a series were given a five-letter code to mask the identity of experimental conditions in subsequent analyses. The serial section images were aligned and dendrites were traced using the Reconstruct software [available for free download at http://synapseweb.clm.utexas.edu (Fiala, 2005). Section dimensions were calibrated using

a diffraction grating replica (Ernest Fullam, Latham, NY) imaged with each series and the cylindrical diameters method was used to compute section thickness (Fiala & Harris, 2001). The calculated section thicknesses ranged from 49 to 56 nm. The area of a cross-sectioned synapse was calculated by measuring its length on each section and multiplying by section thickness for each section it traversed. All traces were curated after initial tracing was completed. Curator was also blind to condition.

DATA ANALYSES AND STATISTICS

Reconstructions were obtained from Reconstruct (Fiala, 2005) which generates quantitative measurements of the traces made on the calibrated images. Data organization was done using the Python programming language with the Pandas, SciPy, NumPy, and Sci-kit learn modules. Statistical analyses were done in the STATICSTICA software package (StatSoft, Tulsa, OK). All comparisons between control and TBS conditions were by structure type within the individual slices. All data are shown as mean ±SEM unless otherwise noted and significance was accepted at $p < 0.05$. Specific statistical tests used for each comparison are indicated in the text, and means, p-values, and partial-η^2 are indicated in the text or figure legends.

Chapter 3: Results – Aspiny Dendrite Fine Structure

PHYSIOLOGY – TWO SLICES

The TBS paradigm successfully induced LTP in both slices, shown in Figure 12. Although it was noted previously that the induction electrode was alternated between slices, the actual placement of the stimulating electrodes was not outside of what is considered medial CA1. Extrahippocampal inputs to CA1 are known to differ between proximal and distal regions and often specifically target interneurons (Cembrowski et al., 2016; Igarashi et al., 2014; Sun et al., 2018). There is no definitive atlas of interneuron type distribution across the proximo-distal axis (because there is no definitive identification of interneuron types), and no evidence of significant heterogeneity in interneuron types across the horizontal axis exists. We were aware of potentially complex effects of antidromic stimulation on feed-forward and feedback inhibition (Bukalo et al., 2013). It is unlikely that this is a significant source of variation for two reasons. First, the position of the tissue acquired for EM reconstruction was on the distal side of the electrode for both conditions in both slices and the minimum 800μm separation of the electrodes is far enough to ensure that axons stimulated by one diverge sufficiently to not stimulate dendrites adjacent to the other electrode. Therefore, the tissue was positioned to receive only orthodromic stimulation. Second, the temporal coordination of forward and backward inhibition is configured for conditions that obtain in intact, living brain. The flow of information goes from CA3 to CA1 and the precise timing of inhibitory elements in this stream depends on this directionality. However, this pertains to the effects of

inhibition on upstream pyramidal cells. As we are examining the direct excitatory inputs to the interneurons themselves, only monosynaptic excitation occurs, the reception of the action potentials is direct so the distinction of orthodromic and antidromic is not relevant.

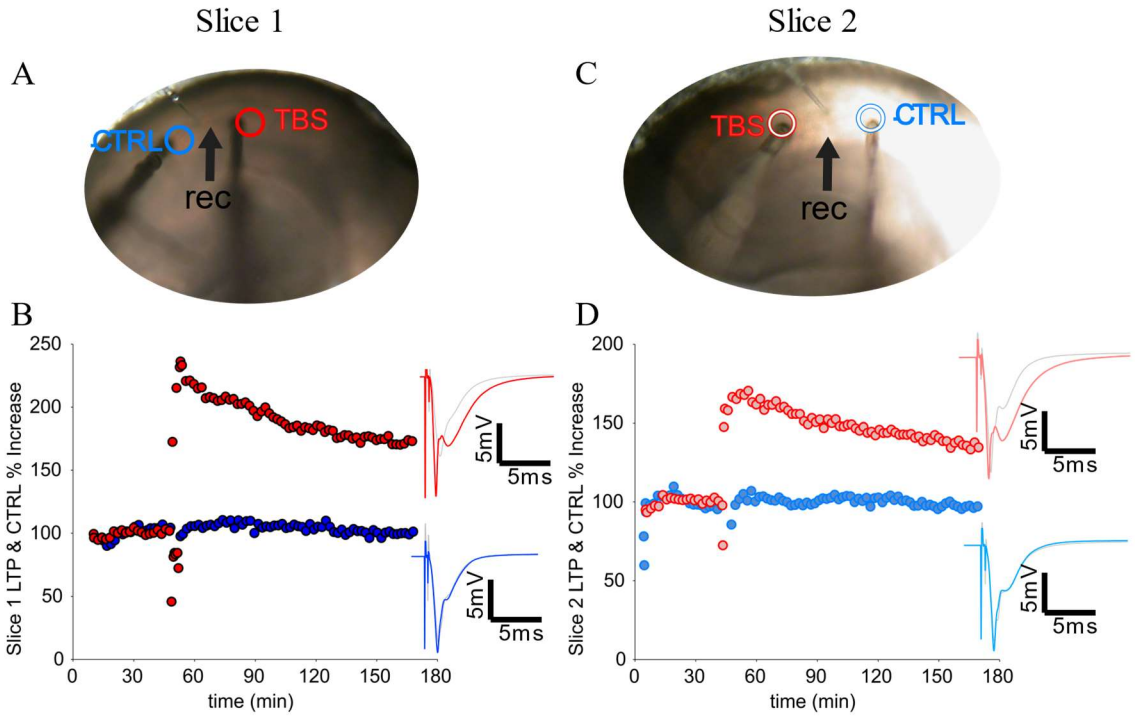

Figure 12. Individual slice physiology. (A-B) Shows images of the slices used for reconstruction and the positions of the two electrodes on the slices. (C-D) Shows the recorded physiology from each slice from both the TBS (red circles) and control (blue circles) electrodes. Y-axis shows the percent increase of the fEPSP slope compared to the 30-minute baseline. TBS stimulation caused significant increase in potentials as measured for two hours (X-axis); control stimulation did not cause a change. Inset are average traces from before and after potentiation induction.

IDENTIFYING AND DISTINGUISHING INTERNEURON DENDRITE REGIONS IN EM VOLUMES

The first feature we looked for was a lack of dendritic spines across multiple sections. If a dendrite showed no spines for ~2µm it was unlikely to show any, though 4/68 of our dendrites were sparsely spiny with a low density similar to that reported in (Scheuss et al., 2014). Another distinguishing feature became apparent: aspiny dendrites in both slices had significantly higher quantities of glycogen particles than spiny dendrites. Though astrocyte processes in this tissue still displayed higher levels of glycogen than aspiny dendrites, astrocytic processes were not mistaken for dendrites. Details of glycogen distribution and relation to synapses can be found in chapter 6.

We asked if there were reliable quantitative anatomical parameters that could be used to distinguish smooth from varicose aspiny dendrites. Visual appraisal of the 3D reconstructions revealed striking differences in morphology as seen in Figure 13. These structures are consistent with those reported at the light microscope level.

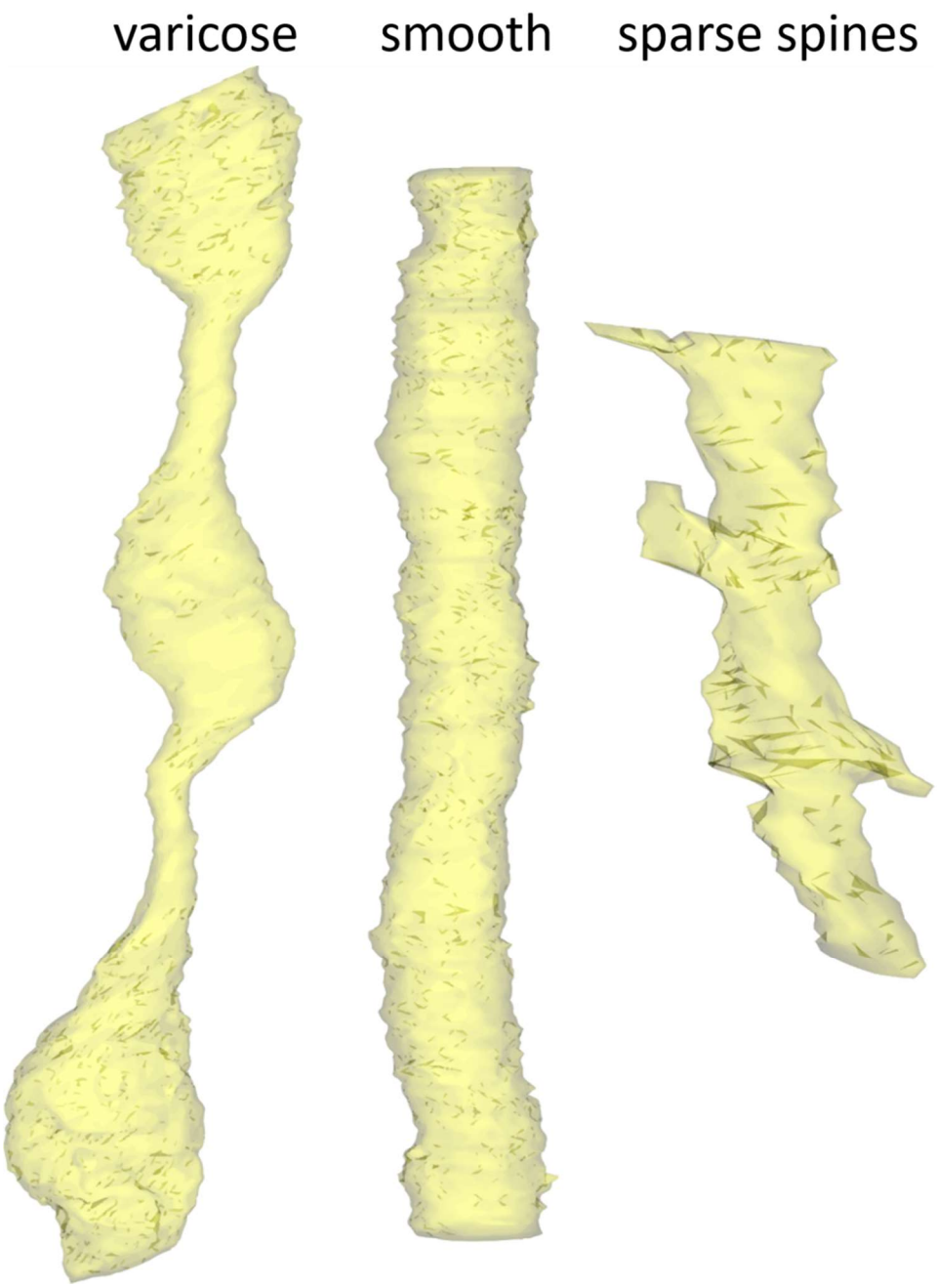

Figure 13. Example of the three types of interneuron dendrite described by Ascoli et al. (2008). Sparsely spiny interneuron dendrites were too few for analysis and are not included.

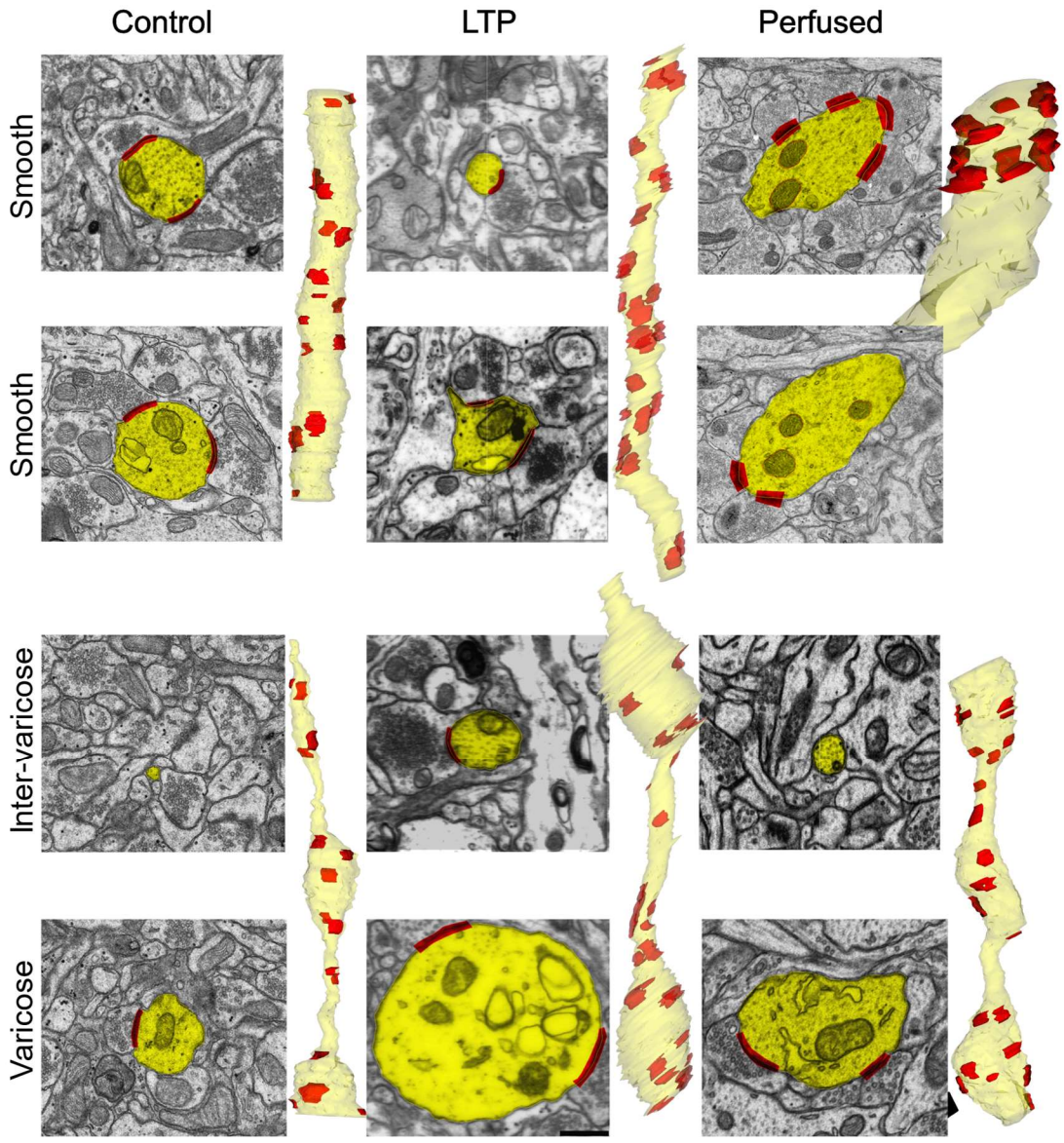

Figure 14 shows example reconstructions of smooth and varicose dendrites from all conditions. Dendrites are highlighted in yellow, PSD are the filled red contours. Mitochondria, synaptic vesicles and spiny dendrites are all visible in the EM images. Figure 14. Examples of smooth and varicose dendrites from all conditions.

EXCITATORY INPUTS

Previous work on this tissue found that by 2 hours following induction of LTP in these slices, synapses on pyramidal cell dendritic spines were significantly larger than synapses in control conditions, that smaller spines became less frequent, and that presynaptic nascent zones increased in frequency and area (Bell et al., 2014; Bourne et al., 2011). Figure 15 shows where previously reconstructed spiny dendrites share the same axons delivering excitatory inputs to the aspiny dendrites reconstructed for this study.

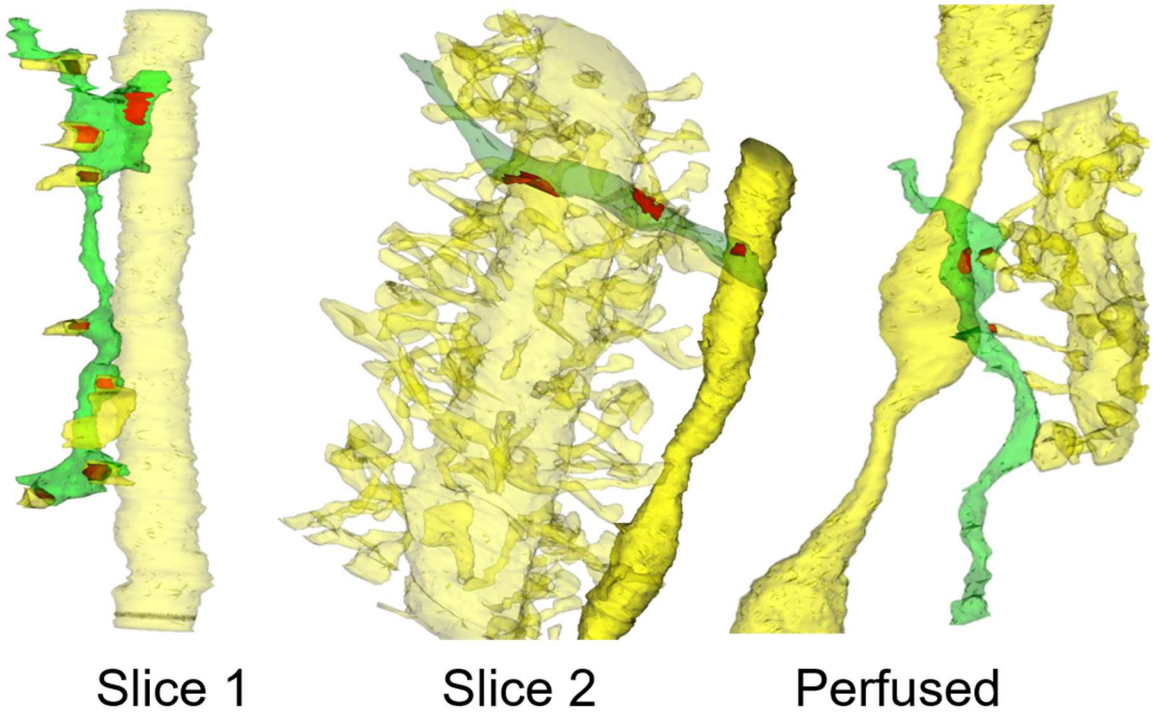

Figure 15. Example aspiny dendrite reconstructions from both slices and perfused tissue showing the excitatory inputs (axons, green) are the same as those that synapse onto adjacent pyramidal cell dendrites (transparent yellow, with spines; slice 1 shows multiple reconstructed spines on afferent axon to smooth dendrite). Synaptic contacts shown in red.

REGION IDENTIFICATION PARAMETERS

We analyzed complete regions, defined as either a varicosity (var) between two inter-varicosities (inter) or an inter between two vars. Smooth dendrites were smooth across the entire series. Prior to quantification, each dendrite was visually assigned to either the smooth or varicose categories. To quantify the visual differences in appearance

we divided the trace with maximum area by the trace with minimum area across the entire segment for each dendrite to obtain a ratio. All visually identified smooth dendrites were found to have a ratio of < 3.5 and all varicose dendrites had a ratio > 3.5. Varicose dendrites had ratios ranging from 5-80. Figure 16 shows the ratios of each dendrite and the proportion of each type in the two slices.

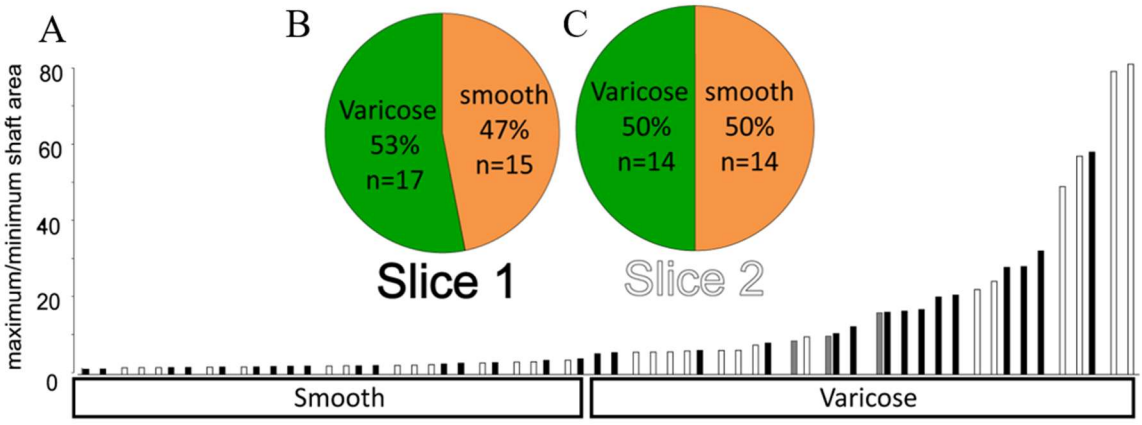

Figure 16. (A) Across the entire length of a reconstruction quantification showed all visually identified varicose dendrites display maximum/minimum section area ratio > 3.5 and smooth < 3.5. (B-C) The number and proportion of the two dendrite types in slice 1 and 2.

EM series are limited in height by the number of serial sections that can be collected and their thickness. Our longest series was 13 µm in height and the shortest was 4 µm. Figure 17 shows example reconstructions of dendrites where a structure was terminated by the end of a series.

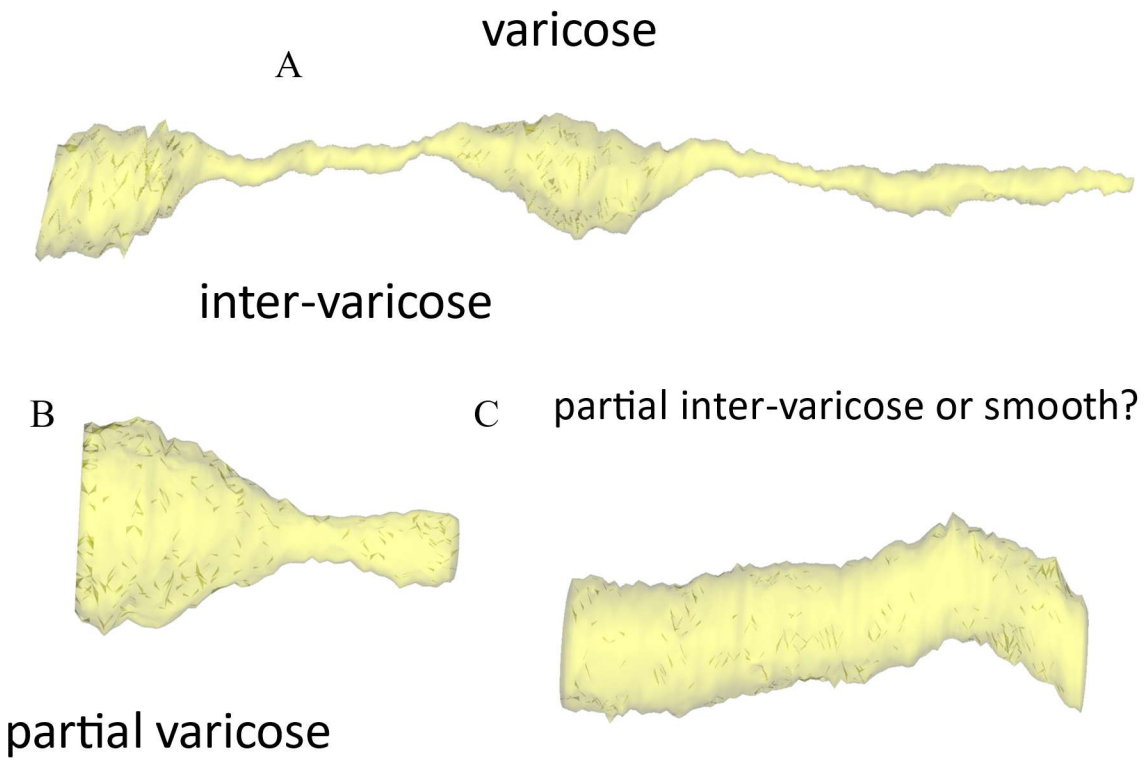

Figure 17. (A) Reconstruction of a varicose dendrite with complete varicose and inter-varicose regions. (B) Reconstruction of a varicose dendrite with the varicosity partially terminated by the end of the series. (C) Reconstructed smooth dendrite traversing the extent of its series. Complete varicose region shown in (A) is 2.02 µm long, segments to scale.

To make accurate determinations of which fine structure was being examined, we analyzed the total set of complete structures to identify parameters that could reliably distinguish them. We compared our sets of complete smooth (n=29), var (n=27), and inter (n=21) regions using several parameters and found they could be distinguished by a minimal combination of two as seen in Figure 18.

Maximum/minimum section area within complete regions was significantly larger in varicose and inter-varicose compared with smooth. The mean lengths of complete varicosities (2.2μm) and inter-varicosity (1.88μm) regions was not significantly different. The length of a smooth region was limited by the series, with nearly all smooth dendrites running perpendicular to the section plane in cross section, Figure 18.A.

Smooth are distinguished by a high cross-sectioned area, a low ratio, and low variance; varicose regions by a high cross-sectioned area, high ratio, and high variance; and inter-varicose by low cross-sectioned area, high ratio, and low variance, Figure 18.B. The variance of the section areas within a region was significantly different between smooth and inter-varicose, and varicose. Mean section area within complete regions was significantly different between smooth and inter-varicose, and varicose and inter-varicose. Mean section area of varicose was significantly larger than smooth when not restricted to complete regions (Figure 18.C), while 18.D shows the lengths of complete regions are similar. See Figure 18 for statistics and significances.

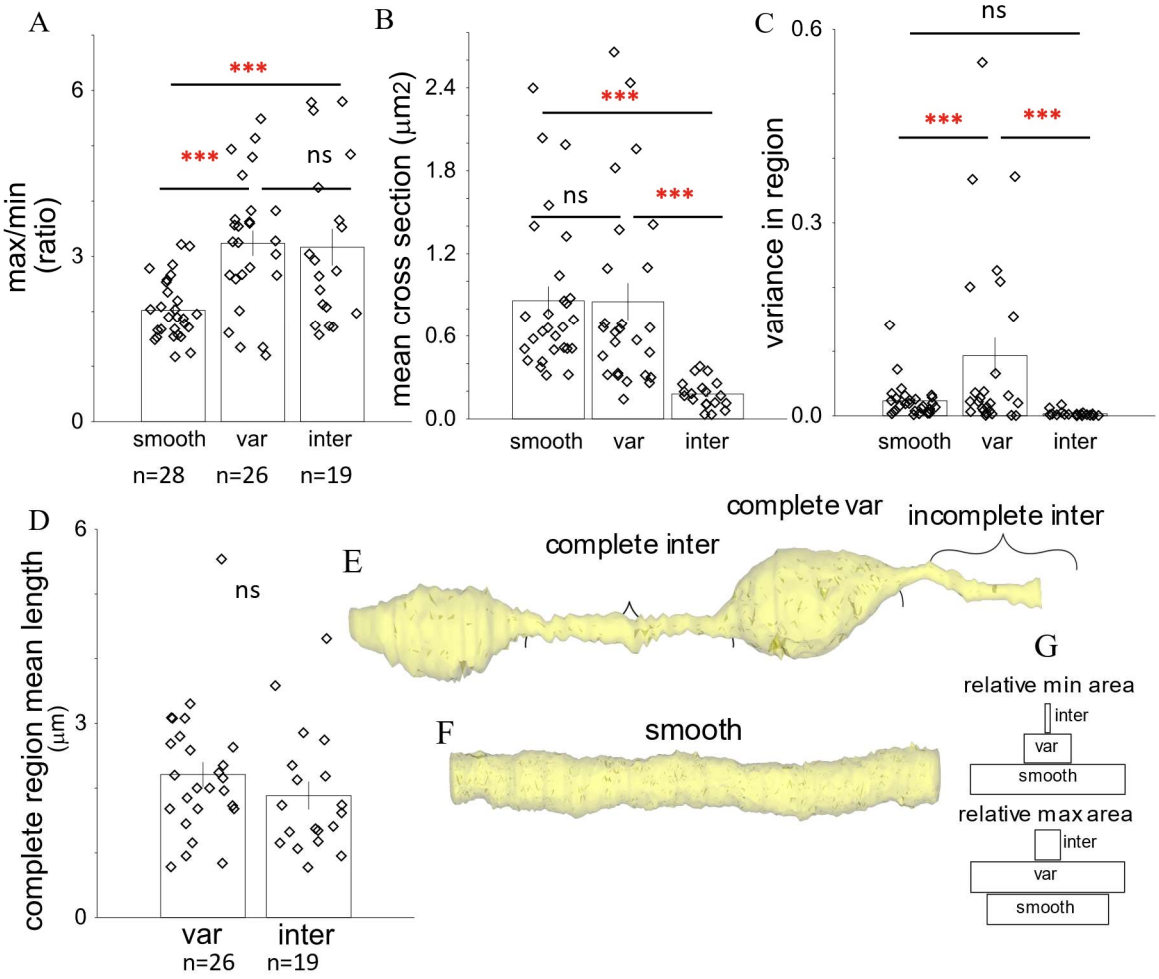

Figure 18. Fine structure quantification.

Figure 18. Fine structure quantification. Comparison of anatomical parameters of complete smooth (n=29), varicose (n=27), and inter-varicose (n=21) regions. Natural logarithm transformations were applied to normalize the distributions of the data sets for hypothesis testing. (A) Mean plots of maximum to minimum ratio of cross-sectional areas of complete regions. Ratios were significantly different between regions (ANOVA, $F_{2,73} = 10.7$, $p = 0.00008$). Varicose regions had significantly higher ratio vs. smooth and inter-varicose while smooth and inter-varicose were not different (mean varicose 3.39±0.225, mean smooth 2.026±0.221, $p < 0.001$; smooth vs. mean inter-varicose 3.134±0.255, $p < 0.001$; varicose vs. inter-varicose, $p > 0.1$, post-hoc Tukey HSD). (B) Mean cross-sectional areas of smooth, varicose and inter-varicose regions were significantly different (ANOVA, $F_{2,73} = 42.3$, $p < 0.00001$). Smooth and varicose regions did not significantly differ (mean smooth 0.859μm^2± 0.0998, mean varicose 0.845μm^2± 0.102, $p = 0.75$). Both smooth and varicose were significantly larger than inter-varicose regions (mean smooth 0.86 μm^2 ± 0.0998, mean inter-varicose 0.174 μm^2± 0.115, $p < 0.001$; mean varicose 0.845 μm^2± 0.102, mean inter-varicose 0.174 μm^2± 0.115, $p < 0.001$). (C) The variance in trace area per section within region was significantly different between types (ANOVA, $F_{2,73} = 22.12$, $p < 0.00001$) with varicose significantly higher than inter-varicose and smooth regions (mean varicose 0.0924±0.017, mean smooth 0.023 ± 0.0163, $p = 0.01$; varicose and mean inter-varicose 0.003± 0.019, $p = 0.0019$; smooth and inter, $p > 0.1$). (D) Mean length of varicose (2.21±0.182μm) and inter-varicose (1.82±0.206μm) regions were not significantly different (ANOVA, $F_{2,46} = 2$, $p = 0.16$). (E) Example complete regions.

Figure 19 shows example reconstructions and a graphical representation of how values per section relate to each other within and between dendrites.

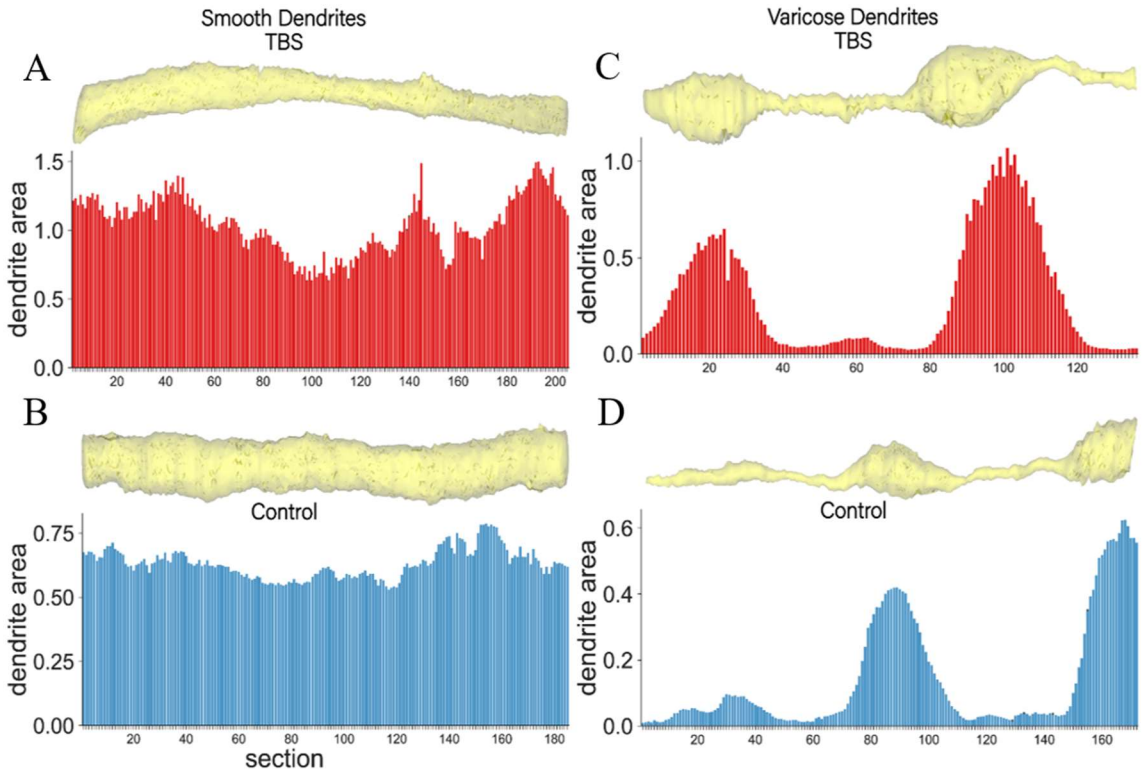

Figure 19. Reconstructions of smooth and varicose dendrites from control and TBS conditions. Y-axis shows the area in microns of the trace of the dendrite shaft on an individual serial section. X-axis shows the section on which the measurement was made. The varicose and inter-varicose regions are easily seen in the plots as are the smooth regions. (A-B) Smooth TBS (red) and control (blue). (C-D) Varicose TBS (red) and control (blue).

ASSIGNMENT OF SYNAPSES TO REGIONS

Exactly which section divides an inter-varicose region from a varicose region was not always obvious. We developed a method that could be applied uniformly to all dendrites. By dividing the area of each section of a dendrite by the mean section area across the entire segment we obtained the ratio of each section to the average. We defined inter-varicose sections as those with a ratio of < 0.5 to the average and varicose sections as those with a ratio of > 0.5 to the average. Smooth dendrites were defined by the ratio of maximum/minimum area across the whole segment, but if analyzed per section in the same way, smooth dendrites always had a section area/mean area ratio close to 1, varicose regions had ratios ranging from 0.037-4.8. See Figure 20.

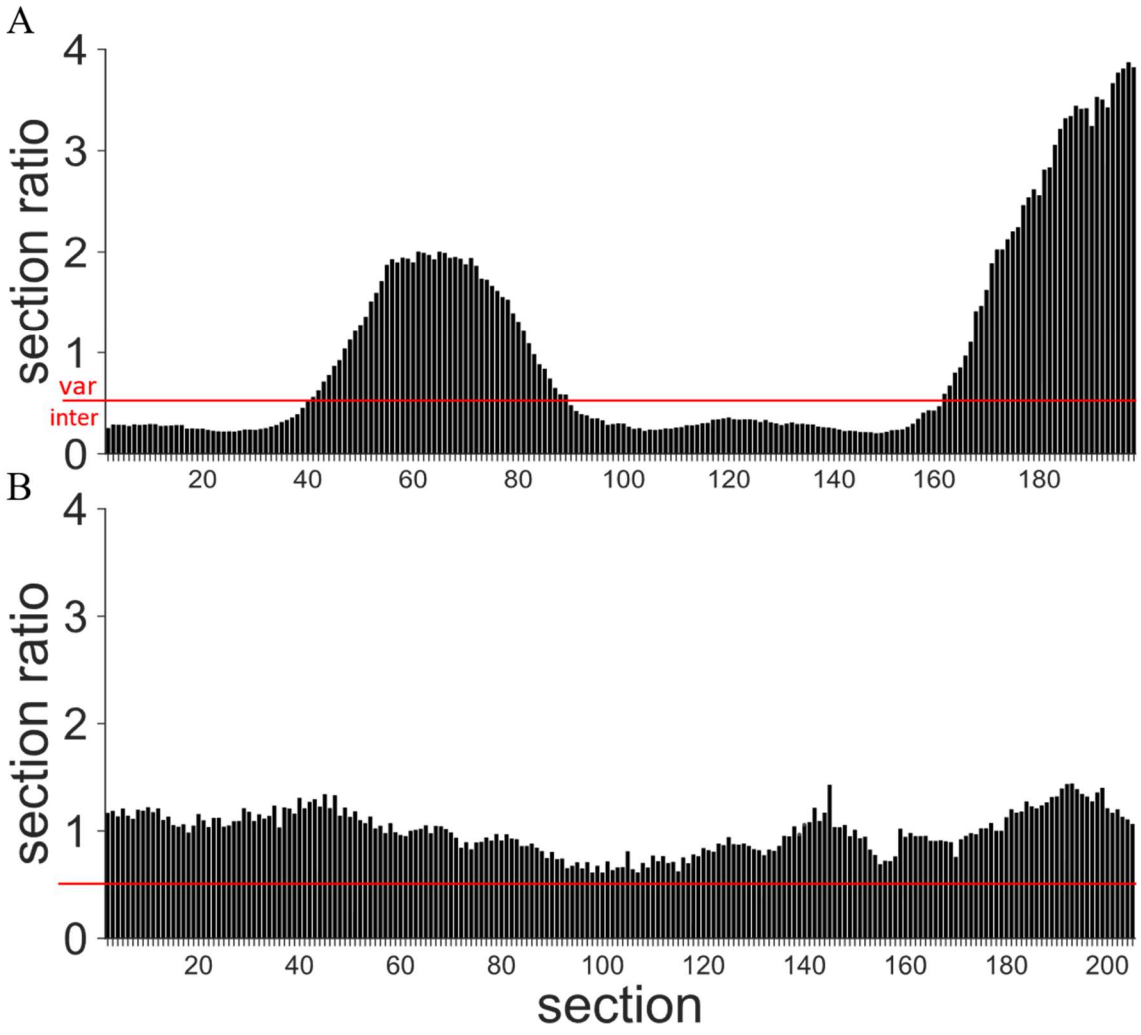

Figure 20. Assigning sections to a region type. (A) varicose dendrite example. Y-axis is the ratio of the section area to the mean area of that entire dendrite. Red line shows cut-off ratio of 0.5. Above this value sections were defined as varicose, sections below the value were defined as inter-varicose region. (B) Same analysis applied to a smooth dendrite. Section ratios never go below 0.5, remaining near 1.

COMPARISON OF FINE STRUCTURES

The morphological properties of dendritic spines on pyramidal neurons are well known to change in response to synaptic plasticity (Bourne & Harris, 2012; Bowden et al., 2012; Zhou et al., 2004). They increase in surface area after undergoing potentiation or decrease after depression. The coupling between PSD size and spine volume is so strong that spine volume is considered an accurate proxy for synaptic strength (Bartol et al., 2015). The dendritic spines from these series were shown to express significantly different morphologies when compared to their within-slice controls at the 2 hour post-TBS time point, with fewer but larger spines and an increase in mean PSD area (Bourne et al., 2011).

There is some evidence from the striatum that PV interneuron dendrites are smooth near the cell body and become varicose as they radiate outwards. No systematic quantification of varicosity likelihood by distance was given, but Kita et al. (1990) show varicosities are clearly present at ~50µm from the soma but closer regions are obscured in the figure (Kawaguchi, 1993; Kita et al., 1990). The lengths reported by Kita are outside the available range of our series. We therefore asked if the fine structures underlying excitatory synapses on aspiny dendrites exhibited any changes in either mean section area for smooth dendrites or in varicosity and inter-varicosity lengths between conditions within a slice. We found no significant changes in the mean cross section area in smooth dendrites, or the lengths of varicose and inter-varicosity regions. Further, these features did not significantly differ from those of perfused dendrites, suggesting the distances from interneuron cell bodies could be similar (Figure 21).

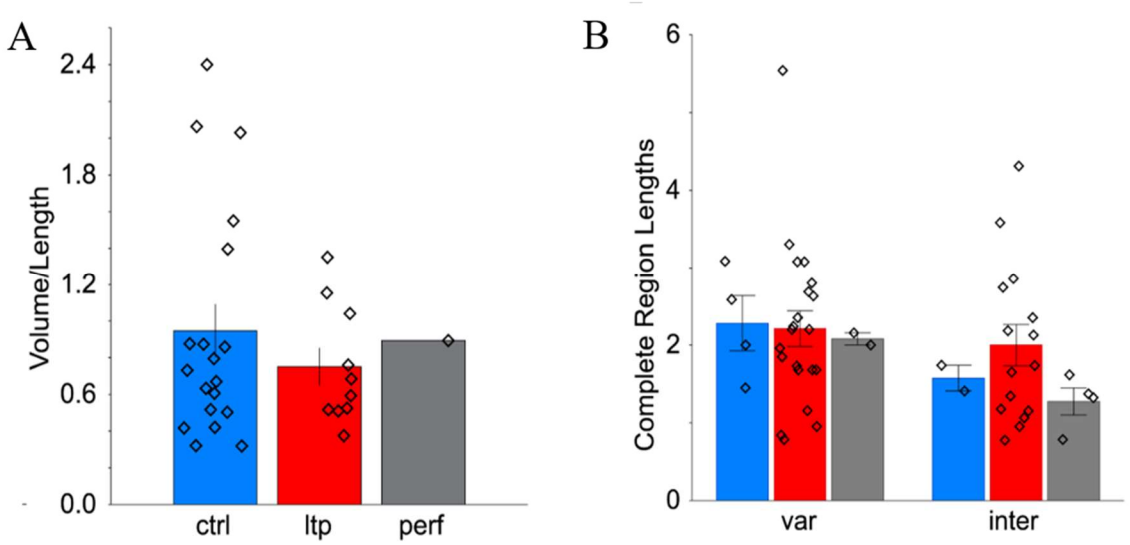

Figure 21. (A) Length of complete varicose and inter-varicose regions was not significantly different between conditions overall (ANOVA, $F_{2,42} = 0.33$, $p = 0.72$); or by type across condition—varicose control (n=4, 2.28± 0.48µm), TBS (n=21, 2.21± 0.21µm), perfused (n=2, 2.07± 0.68µm), (ANOVA, $F_{2,24} = 0.03$, $p = 0.97$); inter control (n=2, 1.574± 0.68µm), TBS (n=15, 2± 0.25µm), perfused (n=4, 1.27± 0.48µm) conditions, (ANOVA, $F_{2,18} = 1.07$, $p = 0.37$). (B) One smooth dendrite was found in perfused tissue thus cannot be statistically compared to control and TBS, and further it was sectioned obliquely while all other dendrites were perpendicular to the slice plain—so trace area would overestimate diameter, shown are plots of volume/length avoiding diameter overestimation, n's are same as above, control (0.95± 0.126), TBS (0.75± 0.174), (ANOVA, $F_{1,27} = 0.72$, $p = 0.7$), perfused (n=1, 0.893).

The proportion of smooth and varicose was evenly split in each slice (Figure 16), though they were not evenly split between control and TBS regions within-slices. That the split between smooth and varicose per side per slice was not even suggests a sampling limitation. Further work with larger samples will be required to determine if there truly is a difference in dendrite types as distance from the proximal or distal CA1 decreases in the middle of SR.

SUMMARY OF STRUCTURES

Establishing objective quantitative analyses allowed consistency in defining these fine structures and their extent across different dendrites. Clearly demarcating the transition points between varicose and inter-varicose regions in the varicose dendrites was necessary to test any hypothesis based on the location of synapses or subcellular structures in relation to them. Further, we showed that basic features like average cross-sectional area or the lengths of varicosities and inter-varicose regions did not change in response to TBS, unlike dendritic spines.

With the analyses and definitions given we were able to objectively assign synapses to the appropriate location and investigate what effects aspiny dendrite fine structure may have on synapse structure and subcellular resources.

Chapter 4: Results – Excitatory Synapses on Aspiny Dendrites

Overall differences in synapse size at different locations

Synapses at smooth locations were the largest on average across all conditions, both slices and perfused. Varicose synapses were intermediate overall, between smooth and inter-varicose on average but had the largest variability and the largest individual synapses in the dataset were found here. Inter-varicose synapses were the smallest and exhibited the lowest variability.

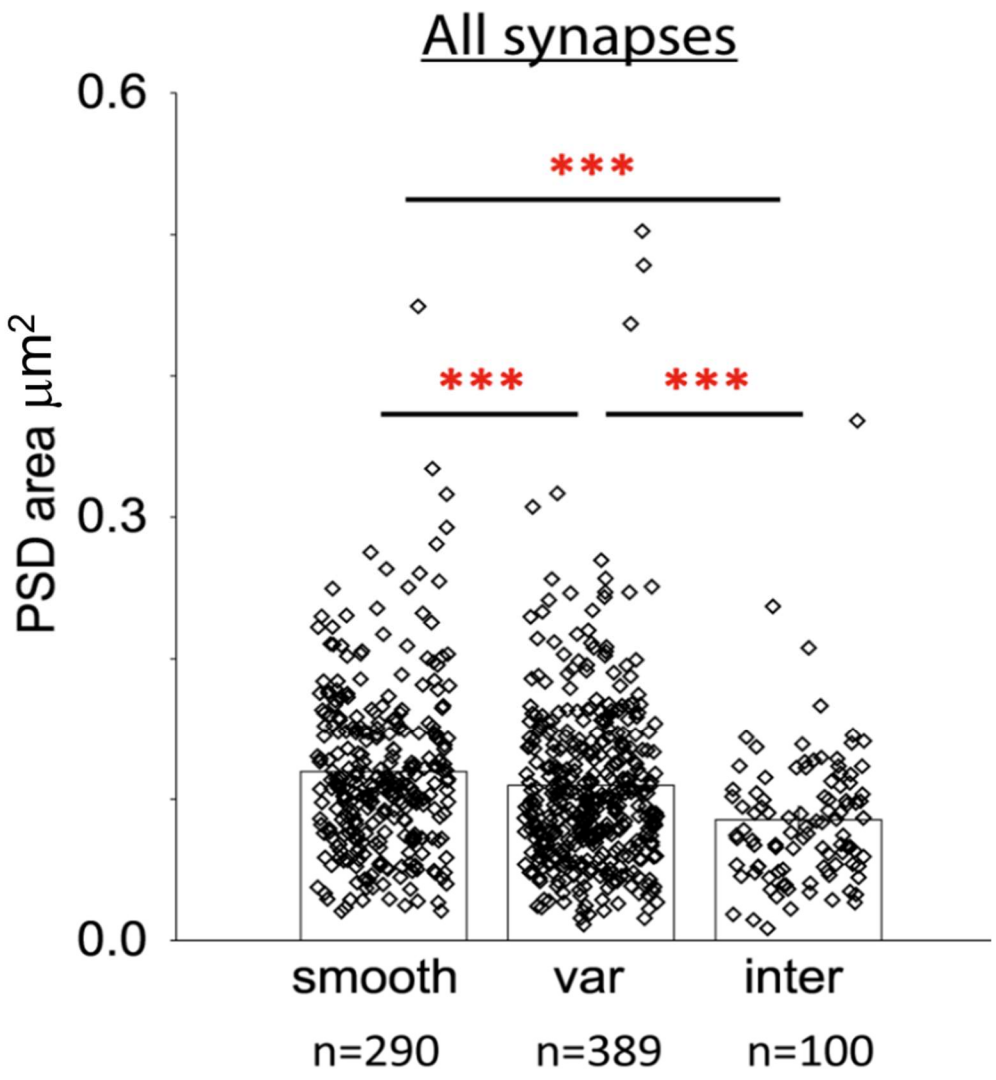

Figure 22. Synapses are largest on smooth regions, intermediate on varicose regions, and smallest on inter-varicose regions in general. All significance tests done on log-transformed PSD area. (A) Synapse size is significantly different by region (ANOVA, $F_{2,776} = 15.33$, $p < 0.00001$). Smooth (n=290, 0.1195± 0.004µm^2), varicose (n=389, 0.1098± 0.003µm^2), inter-varicose (n=100, 0.0085± 0.006µm^2). All pairwise comparisons, $p < 0.05$, Tukey HSD.

VARICOSE REGIONS HAVE MORE SYNAPSES THAN INTER-VARICOSE REGIONS

Do fine structures affect synapse distribution? First, some details about what is known. PV cells receive a significantly higher density of excitatory inputs than CB or CR cells (Gulyás et al., 1999), and they receive the overwhelming majority of these inputs from the Schaffer collaterals making them important feed-forward inhibitors (they do form rare synapses with other interneurons as well as having a high prevalence of autapses, especially bistratified PV cells (Chamberland et al., 2012)) . PV interneurons were long thought to be the most common type in CA1. Though there is still some debate, it is now clear that they are probably exceeded in quantity by nNOS expressing neurogliaform cells, particularly ivy cells—notable for their slow spiking and tendency to form gap junctions with other ivy cells and non-ivy interneurons and are also known to form autapses (Armstrong et al., 2012; Bezaire et al., 2013). CCK SR/SLM cells are known to receive specific excitatory and inhibitory inputs from LEC (Basu et al., 2016) and O-LM cells in oriens are known to receive significant feedback excitation from CA1 pyramidal local collaterals (Lamsa et al., 2007).

3DEM reconstruction provides the resolution to examine the ultrastructural details of connectivity. Why would so many types of interneurons conserve the smooth and varicose morphologies, and why do so few contain spines? What can a varicose dendrite do that a smooth dendrite cannot? What is the role of the dramatic constriction seen between varicosities? While we cannot answer these questions from our data, we can shed some light on the detailed distribution of synapses in relation to these structures, which may suggest links between form and function. Only excitatory synapses are

included in this dataset. It has been estimated that synapses on interneuron dendrites in radiatum are overwhelmingly excitatory, 94% on PV cells (Gulyás et al., 1999). Very few of the synapses found in this dataset met the criteria for classification as symmetric (17/849 complete synapses), and those that did were excluded.

QUANTIFYING SYNAPSE DISTRIBUTION ON VARICOSE DENDRITES

The ratio method described above for identifying individual section traces as smooth, varicose, or inter-varicose made synapse assignment automatic and unbiased. No inter-varicose or varicose synapse was obliquely sectioned, so determination of their area was straightforward. To review, the area of a synapse is the length of the PSD trace times the section thickness for every section on which it appears. Therefore, it was possible for one synapse to appear on sections labeled either varicose or inter-varicose. If a synapse occurred near the transition from a varicose region to an inter-varicose region or vice versa, it was assigned to the region on which more than 50% of its area occurred. If exactly 50% was split across regions it would be assigned at random, but this did not occur in the complete synapses we analyzed.

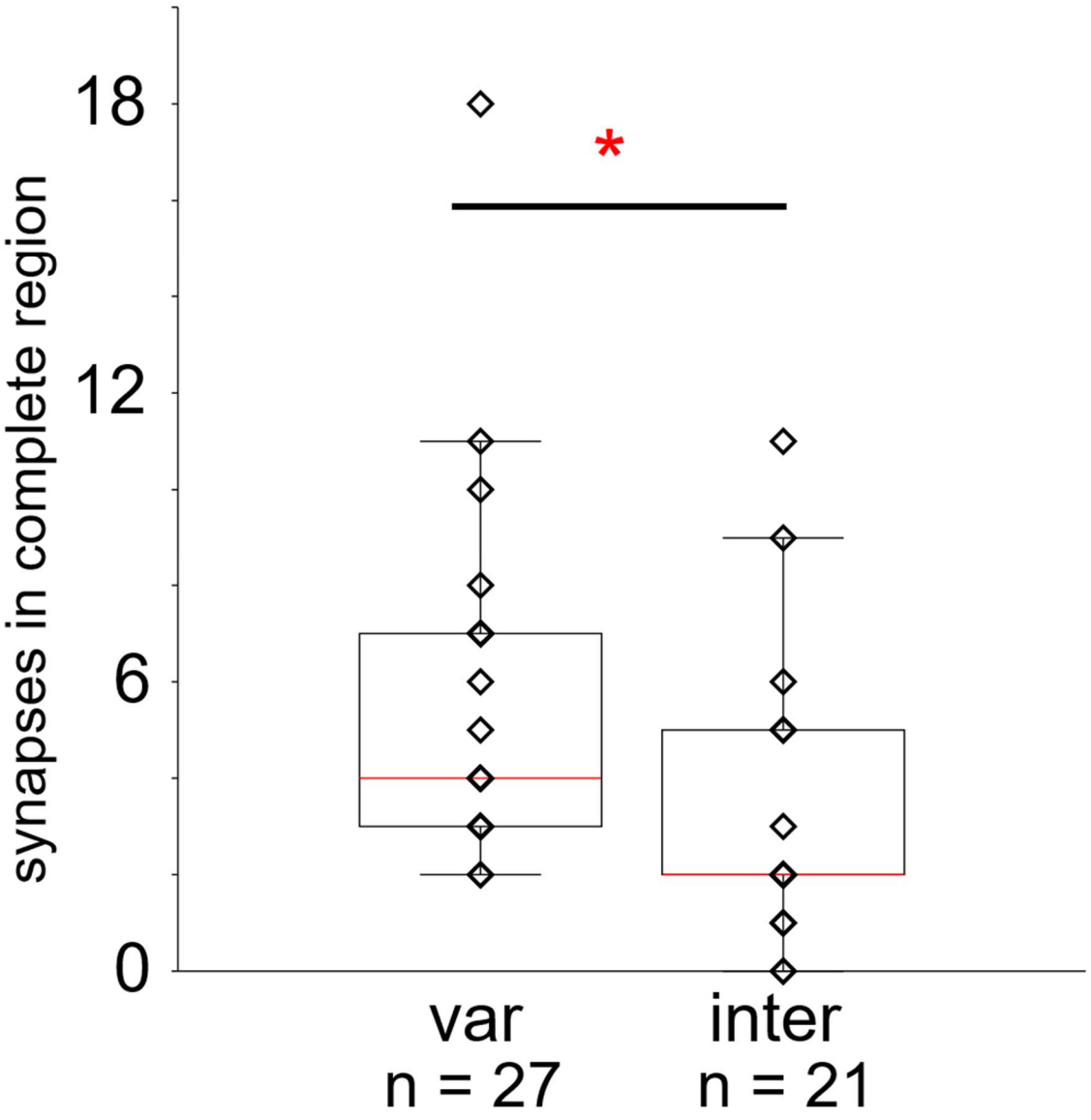

Figure 23. Number of synapses per complete varicose and inter-varicose regions. Varicose regions had a significantly higher number of synapses 5.407±0.614 than inter-varicose regions 3.09±0.696 (ANOVA, $F_{1,46} = 6.203$, $p = 0.016$, partial-$\eta^2 = 0.119$).

First, we analyzed the number of synapses on every complete varicose and inter-varicose region, see Figure 18 for their non-synaptic properties. Complete varicose regions had more synapses than complete inter-varicose regions (Figure 23). This was across all conditions. Control, TBS, and perfused are all represented.

Figure 24 shows a graphical representation of the preference for synapses to occur on varicose regions.

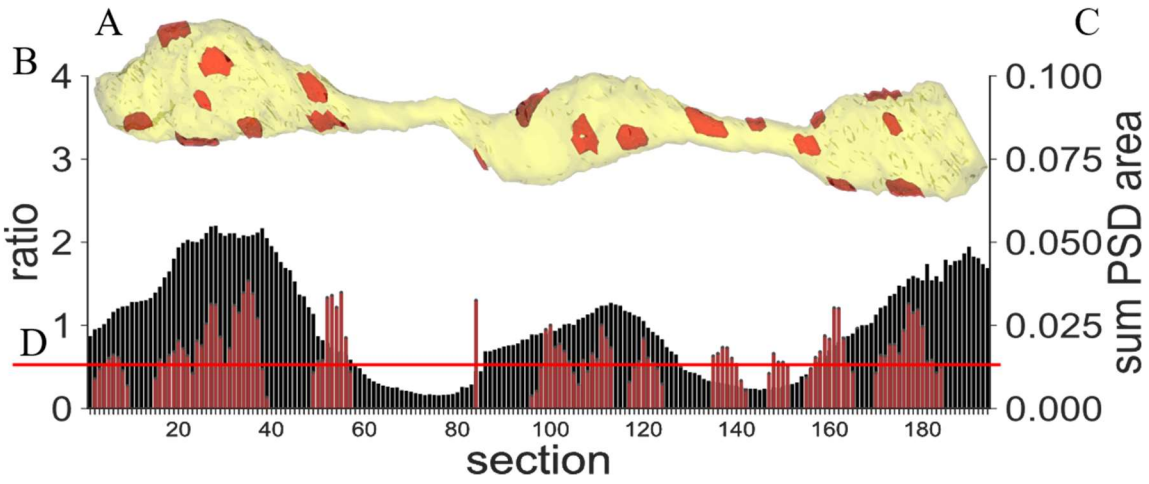

Figure 24. Per section plot showing the majority of synapses occur at varicose regions. (A) Reconstruction of a varicose dendrite from perfused tissue shown in yellow. Red patches are the synapses. (B) The ratio of individual section area to the mean section area. (C) Summed PSD length (dark red) on the same sections as shown in B, if more than one synapse occurred on the same section the length of all PSD traces was added to give one value per section. (D) The dividing line between varicose and inter-varicose as shown above. Most of the PSDs occur on sections where the ratio value is above the cut-off line.

The proportion of synapses on varicose regions vs inter-varicose regions was remarkably consistent, with ~80% of synapses occurring on a varicosity (Figure 25). This distribution was not significantly different between the control and TBS side within each slice or between each slice compared to perfused. The proportion of varicose to inter-varicose synapses was more variable within individual dendrites and most variable within

the TBS condition but did not reach significance. Some had no synapses on inter-varicose regions.

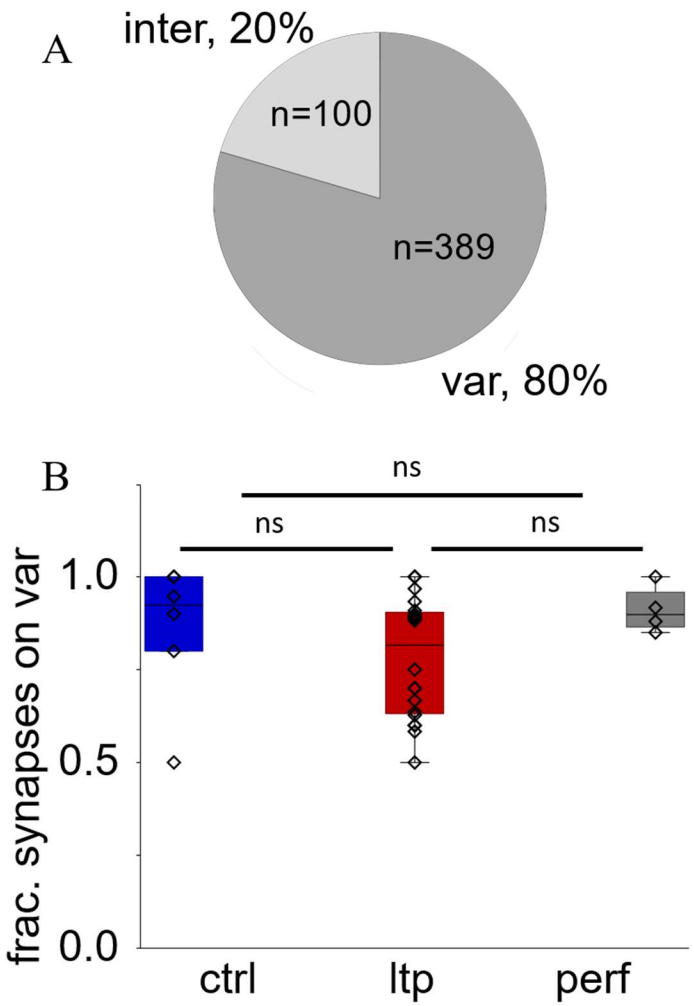

Figure 25. (A) Total number of synapses on inter and var regions across all conditions. (B) Graph of dendrites in each condition combined across slices, data points are dendrites, Y-axis is fraction of synapses on varicosity for each dendrite (ANOVA, $F_{2,27} = 1.39$, $p = 0.264$), control (n=6, 85±0.06%), TBS (n=20, 78±0.03%), perfused (n=4, 91±0.08%), $p > 0.3$ for all pairwise comparisons, Tukey HSD.

Smooth dendrites displayed a greater variability in the number of synapses per micron length or per square micron of surface area. No clustering of synapses was detected along the segments.

COMPARISON OF SYNAPSES IN CONTROL REGIONS AND PERFUSED TISSUE

The effects of TBS on the structural plasticity of excitatory synapses onto interneurons only become apparent in the context of the morphologically distinct fine structures. Before examining the effects of LTP induction on the aspiny dendrite synapses, we compared synapses between control regions and the perfused tissue.

By cutting slices at room temperature and allowing recovery within the warm humidified interface chamber for at least 3 hours prior to recording previous experiments have found that by this protocol pyramidal cell spine properties are comparable to perfusion-fixed brain (Bell et al., 2014; Bourne et al., 2011a; Fiala et al., 2003; Kirov et al., 1999). We compared the synapses on aspiny dendrite regions from the control condition of each slice and the perfused controls. Figure 26 shows the position of the control electrode in each slice. The box and whisker plots of synapses from each region compared to the same region between slices and perfused (see figure caption for p-values and details of tests used). Raw data is shown on top of the boxes to illustrate the variance in each group, the median of each sample is shown as a black line in the boxes. No significant difference was found in the mean (white box with black outline) size of

synapses between any of the aspiny region types across control conditions and perfused tissue.

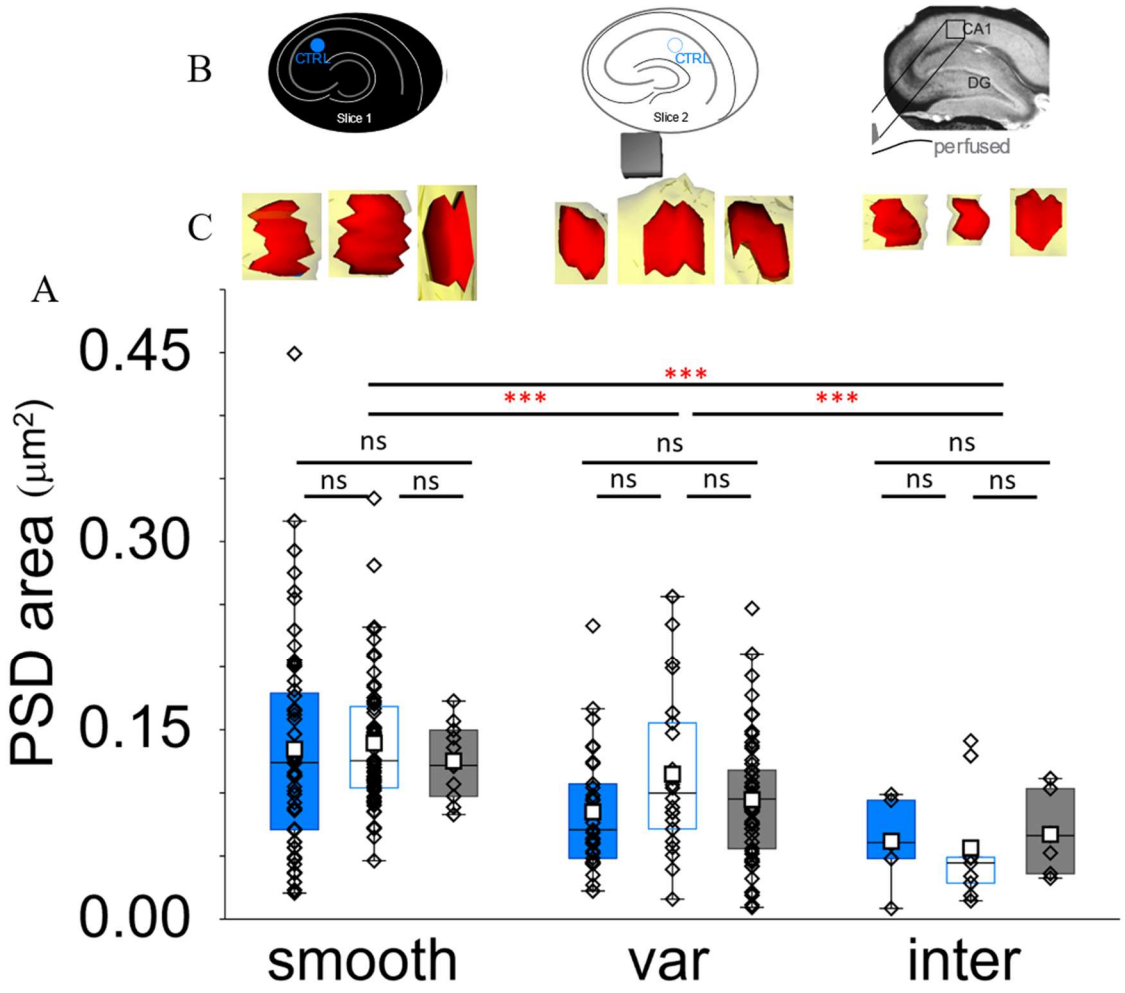

Figure 26. (A) Control synapses were compared with each other and perfusion-fixed tissue by type. No differences were found between synapses on the same dendrite regions across slices and perfused (ANOVA, synapse position*condition, $F_{4,235} = 0.88$, $p = 0.474$). (B) Diagrams of the position of the control electrode in each slice. (C) Example reconstructions of synapses of each location from slice control regions and perfused. The reconstructions are the median example from each distribution, scale cube = 200nm on a side.

Slice control comparisons: slice 1 (n=56) vs. slice 2 (n=60) smooth control (slice 1: 0.135±0.0084μm^2 – slice 2: 0.139±0.0081μm^2, p = 0.775), slice 1 (n=31) vs. slice 2 (n=24) varicose control (slice 1: 0.085±0.011μm^2 – slice 2: 0.125±0.013μm^2, p = 0.587), slice 1 (n=6) vs. slice 2 (n=8) inter control (slice 1: 0.062±0.026μm^2 – slice 2: 0.057±0.022μm^2, p = 0.99). Slice 1 control vs. perfused: slice 1 (n=56) vs. perfused (n=11) smooth control (slice 1: 0.135±0.0084μm^2 - perfused: 0.125±0.0189μm^2, p = 0.999), slice 1 (n=31) vs. perfused (n=42) varicose control (slice 1: 0.085±0.011μm^2 - perfused: 0.096±0.007μm^2, p = 0.988),), slice 1 (n=6) vs. perfused (n=6) inter control (slice 1: 0.062±0.026μm^2 - perfused: 0.072±0.025μm^2, p = 0.992). Slice 2 smooth vs. perfused smooth (p = 0.999), slice 2 var vs. perfused var (p = 0.964), slice 2 inter vs. perfused inter (p = 0.881).

We did not pool the control condition data from the two slices when comparing TBS conditions vs control, a standard practice when analyzing pyramidal cell dendrites between slices if no systematic significant differences exist between slices. Slices from different animals can have inherent variability that makes pooling invalid. However, by using tissue from the same position in the hippocampus of animals very close in age and weight, this variability is limited. The homogeneity of pyramidal cell dendrites and axons within middle SR often allows for pooling both the control and LTP conditions of slices from multiple animals. Several publications using TEM data acquired from these series found that pooling was warranted in regards to the specific features being studied—including, but not limited to, spiny dendrites and polyribosomes (Bourne et al., 2011b), synaptic nascent zone dynamics (Bell et al., 2014), axons and vesicles (Bourne et al.,

2013), and smooth endoplasmic reticulum (Chirillo et al., 2015). However, when dealing with interneurons we are presented with an unknown distribution of subtypes. When analysis of variance was performed as mentioned in Figure 26, a significant interaction by slice was found. Effect of slice on control synapse size, $F_{1,215} = 4.67$, $p = 0.032$, therefore we did not pool across experiments.

THETA BURST AND STRUCTURAL SYNAPTIC PLASTICITY

Previous works on interneuron plasticity have found a variety of responses from inhibitory cells in response to numerous induction protocols that reliably induce lasting changes in synaptic responses at excitatory cells. Findings have ranged from no changes at all, to non-pathway specific LTD in response to HFS that induces LTP in fEPSPs, NMDAR-dependent LTP, and NMDAR-independent Anti-Hebbian LTP. Of all the varied protocols and results from the many experiments on interneuron synaptic plasticity discussed in chapter 1, there is one latent finding they all have in common. All the studies made note of this, usually in passing and a few mentioned it more than once. The common feature is that regardless of the results (for the papers reporting results), plasticity, by whatever protocol, only occurred in a portion of the recorded cells. Looking closer we find that Lamsa et al. (2005) reported a homosynaptic NMDAR-dependent LTP in radiatum where 16/30 interneurons expressed LTP with a paired stimulation protocol and 17/45 interneurons expressed LTP when depolarization was held constant and one input pathway stimulated at low frequency. Lamsa et al. (2007) reported 25/31 SO interneurons expressed Anti-Hebbian NMDAR-independent LTP. McMahon et al.

(1997), the first report of iLTD found 32/49 radiatum cells depressed, 14/49 did not change, and 3/49 potentiated—in response to 100Hz tetanus that caused LTP in adjacent pyramidal cells. A later experiment by the same group reported iLTD in the majority of interneurons in 26/29 experiments, though total number of unsuccessful cells was not reported (Gibson et al., 2008). Something that must be kept in mind about the iLTD experiments was that all recordings were made in the whole-cell patch configuration. The experiments reporting LTP all used perforated patch.

By two hours after the induction of LTP by TBS, pyramidal cell dendritic spines appear quite different from their within-slice controls. Aspiny dendrites by definition lack spines; however, the fine structures they exhibit that we described above appear to have a significant effect on how their synapses respond to the increase in excitatory drive to pyramidal cells as measured by the robust increase in fEPSP slope (see Figure 12 for the physiological responses of each slice).

Figure 27 shows the responses of aspiny synapses to LTP induction in the slice. Both slices exhibited significant changes in their synapse sizes compared to within-slice controls after TBS. Smooth and varicose type synapses responded differently in each slice. Intriguingly, inter-varicose type synapses significantly increased in size in both slices. Smooth region synapses in slice 1 did not significantly change compared to control while both varicose and inter-varicose region synapses significantly increased in size—varicose by 34% and inter-varicose by 30%. In slice 2 the size of synapses on smooth dendrites significantly decreased compared to controls by 29%. Varicose region synapses

in slice 2 synapses did not change and the inter-varicose region synapses showed the largest change relative to control of all groups, increasing by 75%.

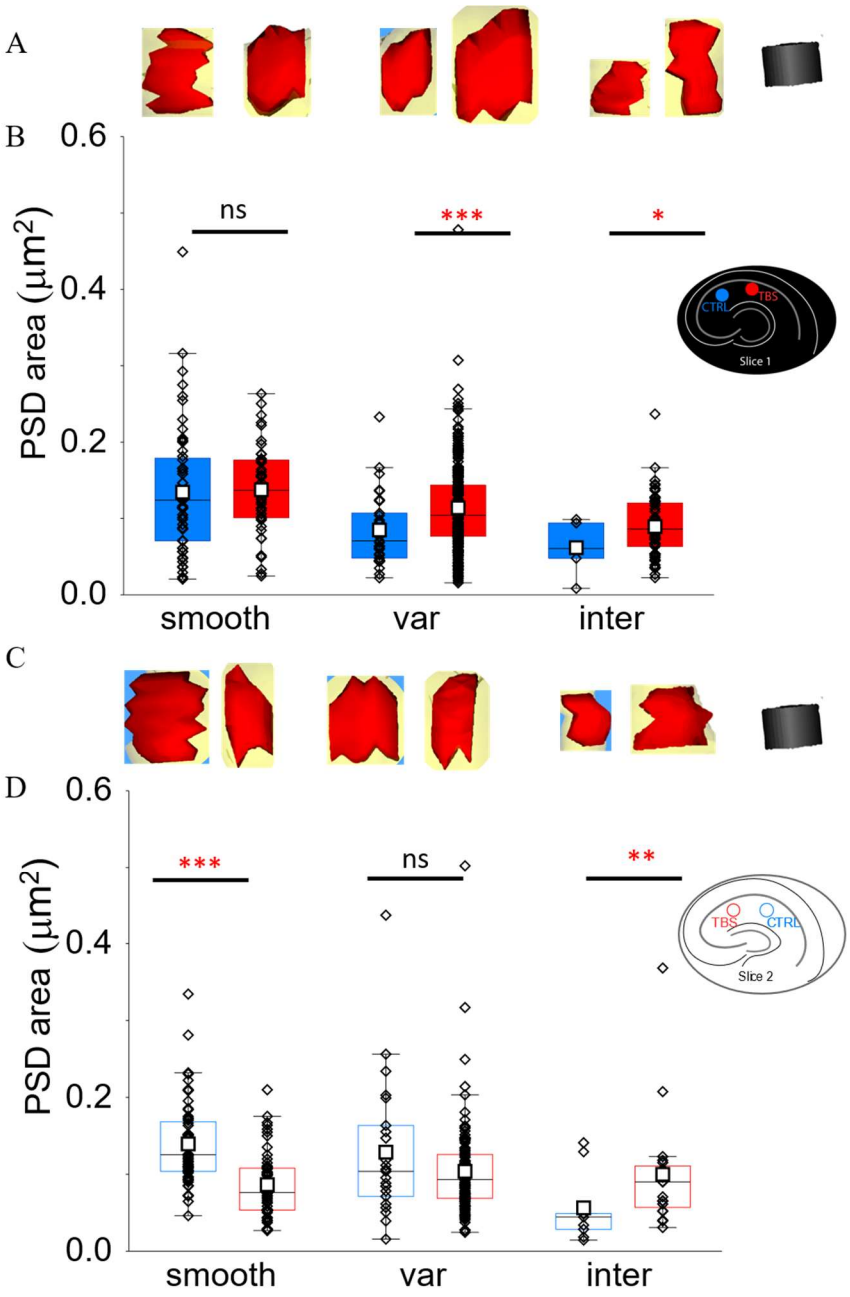

Figure 27. Effects of TBS on synapse size in each slice. (A, C) Reconstructions of synapses at the mean of each distribution. Scale cube = 200nm on a side. (B, D) Box plots of control (slice 1 solid blue, slice 2 empty blue) TBS conditions (slice 1 solid red, slice 2 empty red), median is black bar, mean is white square.

Figure 27 clearly shows the different effect TBS has on the different regions in the different slices. Slice 1 TBS region compared with its within-slice control showed consistent increases at synapses on varicose dendrites, but not on smooth. Overall, condition had a significant effect on PSD size in slice 1 (nested ANOVA, synapse position(condition), $F_{4,439} = 8.28$, $p < 0.00001$). One-way ANOVA was performed on the log-transformed PSD areas between control and TBS regions for each synapse location. Smooth synapses did not significantly change in size. Varicose and inter-varicose synapses were significantly larger after TBS. Slice 1 control (n=56) smooth vs. TBS (n=44) smooth (control: 0.135±0.0084μm^2 - TBS: 0.138±0.0088μm^2, ANOVA $F_{1,98} = 0.78$, $p = 0.378$), varicose (n=31) control vs. varicose (n=248) TBS (control: 0.085±0.011μm^2 - TBS: 0.114±0.004μm^2, ANOVA $F_{1,277} = 8.91$, $p = 0.00308$, partial-$\eta^2 = 0.0312$), inter (n=6) control vs. inter (n=60) TBS (control: 0.062±0.026μm^2 - TBS: 0.088±0.008μm^2, ANOVA $F_{1,64} = 4.74$, $p = 0.033$, partial-$\eta^2 = 0.069$). The average varicose synapse area increased by 34%, inter synapses increased by 30%, and smooth were non-significantly only 2% larger. Slice 2 TBS region synapses compared with their within-slice controls showed different effects from slice 1, in both smooth and varicose dendrites. Again, condition also had a significant effect on PSD size in slice 2 (nested ANOVA, synapse position(condition), $F_{4,296} = 8.78$, $p < 0.00001$). Smooth TBS synapses significantly decreased in size compared to control while varicose did not change and inter significantly increased. Slice 2 control (n=60) smooth vs. TBS (n= 119) smooth (control: 0.135±0.0084μm^2 - TBS: 0.0949±0.0005μm^2, ANOVA $F_{1,177} = 37.18$, $p < 0.0001$, partial-$\eta^2 = 0.174$), varicose (n=24) control vs. varicose (n=44) TBS (control:

0.125±0.013μm^2 – TBS: 0.106±0.009μm^2, ANOVA $F_{1,66}$ = 0.64, p = 0.428), inter (n=8) control vs. inter (n=20) TBS (control: 0.057±0.022μm^2 – TBS: 0.100±0.013μm^2, ANOVA $F_{1,26}$ = 6.18, p = 0.019, partial-η^2 = 0.192). Smooth synapses decreased by 29%, varicose synapses non-significantly decreased by 15%, and inter-varicose synapses increased by 75%.

STRUCTURAL PLASTICITY – SUMMARY

The varicosities host the majority of synapses in both control and TBS conditions as well as in perfused tissue. Whether this is simply due to the greater surface area they provide cannot be answered with these data alone. The lack of spines, particularly in PV interneurons, has been suggested to be an adaptation to facilitate the rapid propagation of electrical potential to support fast spiking, especially since interneurons seem to lack some of the voltage dependent channels used for active propagation of sodium and calcium waves seen in spiny pyramidal dendrites (Hu et al., 2014a). This does not explain any functional differences that varicose aspiny dendrites may support aside from what smooth aspiny dendrites may be doing.

The increase in inter-varicose synapse area was consistent across both slices. What is more interesting is that the varicose synapses did not behave the same way. This is important because the varicose and inter-varicose synapses occur on the same dendrites. This suggests at least the possibility of independent response at varicosities and inter-varicose regions over distances as short as 2μm, the average lengths of these structures.

In the next chapter we will examine the distribution of some subcellular resources with respect to the fine structures. These analyses will provide some elaboration on the possible roles of varicosities and inter-varicosity regions in the function of aspiny dendrites.

Chapter 5: Results – Mitochondria

Mitochondria are ancient subcellular organelles that all[1] eukaryotic cells depend on to live. Beyond their necessary role in generating ATP, mitochondrial presence in both dendrites and axons can affect synaptic functions through their ability to buffer calcium (Mattson et al., 2008; Smith et al., 2016). Mitochondria and known to redistribute toward dendritic protrusions in response to synaptic stimulation and it has been shown that interfering with mitochondrial motility by inhibiting dynamin motor-proteins leads to a dramatic decrease in spine density (Li et al., 2004). Active synapses require high levels of energy and produce calcium transients, and the mitochondria frequently found in boutons are uniquely capable of providing ATP and absorbing excess calcium. Axonal mitochondria are more motile than dendritic mitochondria, but there is evidence that dendritic mitochondria change the direction of their motion more frequently, consistent with the idea that they relocate in response to synaptic activity (Overly et al., 1996).

Mitochondria are active organelles that behave dynamically in response to local and global conditions within the cells where they reside. Mitochondria themselves are highly energized, actively maintaining an electrical potential of ~-150mV with respect to the cytosol (Kann & Kovacs, 2006) and aid in sculpting the precise spatial and temporal extent of calcium transients in both presynaptic and postsynaptic terminals (Brocard et al., 2001; Sparagna et al., 1995). Hypometabolism and changes in cerebral blood flow

[1] Only one known eukaryotic organism is known to completely lack mitochondria, *Monocercomonoides sp.* (Karnkowska et al., 2016).

that can accompany or precede epileptic seizures have been linked to dysfunction of mitochondrial ability to both regulate their own energy demands and respond properly to those of the neurons where they reside (Tanaka et al., 1990).

The brain is a very power-hungry organ, and fast-spiking interneurons have even higher energy requirements to sustain steady firing rates that can exceed 100Hz (Buzsáki et al., 2007). For more on energy supply and energy utilization, see chapters 6 and 7. Studies of interneurons that mention dendritic varicosities usually note that they tend to contain mitochondria (Freund et al., 1996). As with dendritic spines, dendritic varicosities provide a visual landmark for studying the organization of fine structures but also subtly bias observations towards these obvious structures and away from regions that are both more difficult to observe and define. Studies of mitochondria in inhibitory interneurons has usually focused on gross distribution using techniques like staining for cytochrome oxidase C (Gulyás et al., 2006) using light microscopy, so dendritic varicosities present structure that is large enough to measure with some degree of accuracy. Other studies on interneuron mitochondria have focused on the presynaptic mitochondria, describing their distribution and ultrastructure in exquisite detail (Takács et al., 2015). Though smooth aspiny regions may seem superficially less interesting, we will show that mitochondrial association is no less dynamic. Further, the relationship between mitochondria and the inter-varicose regions has received almost no attention in the literature, likely because quantifying their distribution is impractical without 3DEM reconstruction and, as we have found, under basal conditions mitochondrial association

with inter-varicose regions is dramatically lower than tissue in which LTP has been induced.

Some beautiful EM images from varicose interneuron dendrites cut parallel to the plane of the arbor have been published, in particular a study on reactive mitochondria distribution in the hippocampus (Kageyama & Wong-Riley, 1982). Here we describe the appearance and extend of mitochondrial ultrastructure with respect to the fine structures of aspiny dendrites, what relationships exist between mitochondria and synapses, and the effects of functional LTP induction and maintenance on their characteristic distribution.

OVERALL DISTRIBUTION OF MITOCHONDRIA IN ASPINY DENDRITES

The total mitochondria area per section was taken by summing the areas of every separate mitochondrial trace in that section in square microns. Figure 28.A shows two separate mitochondria traces in purple. Figure 28.B shows that smooth aspiny regions had the most sum mitochondria area per section of the region types. Varicose region sections had an intermediate amount of mitochondria area, the highest variability, and the largest range of sizes. Inter-varicose region sections had the least mitochondria area.

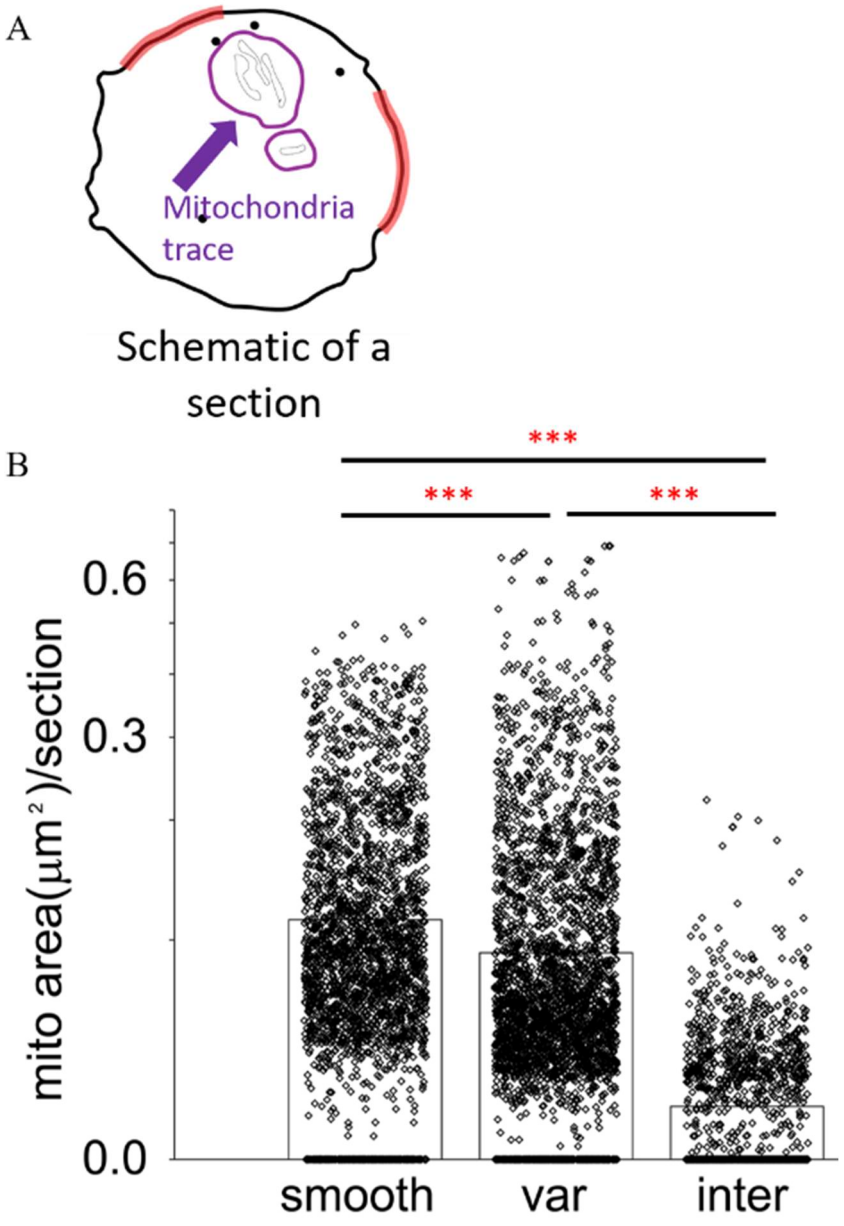

Figure 28. (A) Diagram of the structures in a section of dendrite. (B) Mean mitochondria area in all sections of each type (ANOVA, $F_{2,7115} = 643.2$, $p < 0.00001$). Mean smooth (n=1779) 0.114±0.002µm^2, varicose (n=2475) 0.092±0.0015 µm^2, inter (n=656) 0.017±0.0002 µm^2, smooth vs. varicose vs. inter, $p < 0.0001$ for both, varicose vs. inter, $p < 0.0001$.

MITOCHONDRIA DISTRIBUTION BY SLICE AND CONDITION

Using the per section display we can see that mitochondria distribution tends strongly to overlap with synapse distribution. Simply, there are few synapses without any mitochondria within the same sections where they occur. This distribution changes in the TBS condition compared to slice controls, with significant changes in all regions and the biggest changes in the inter-varicose regions of both slices. Figure 29 shows example per section graphs with dendrite reconstructions of both varicose and smooth dendrites in both conditions.

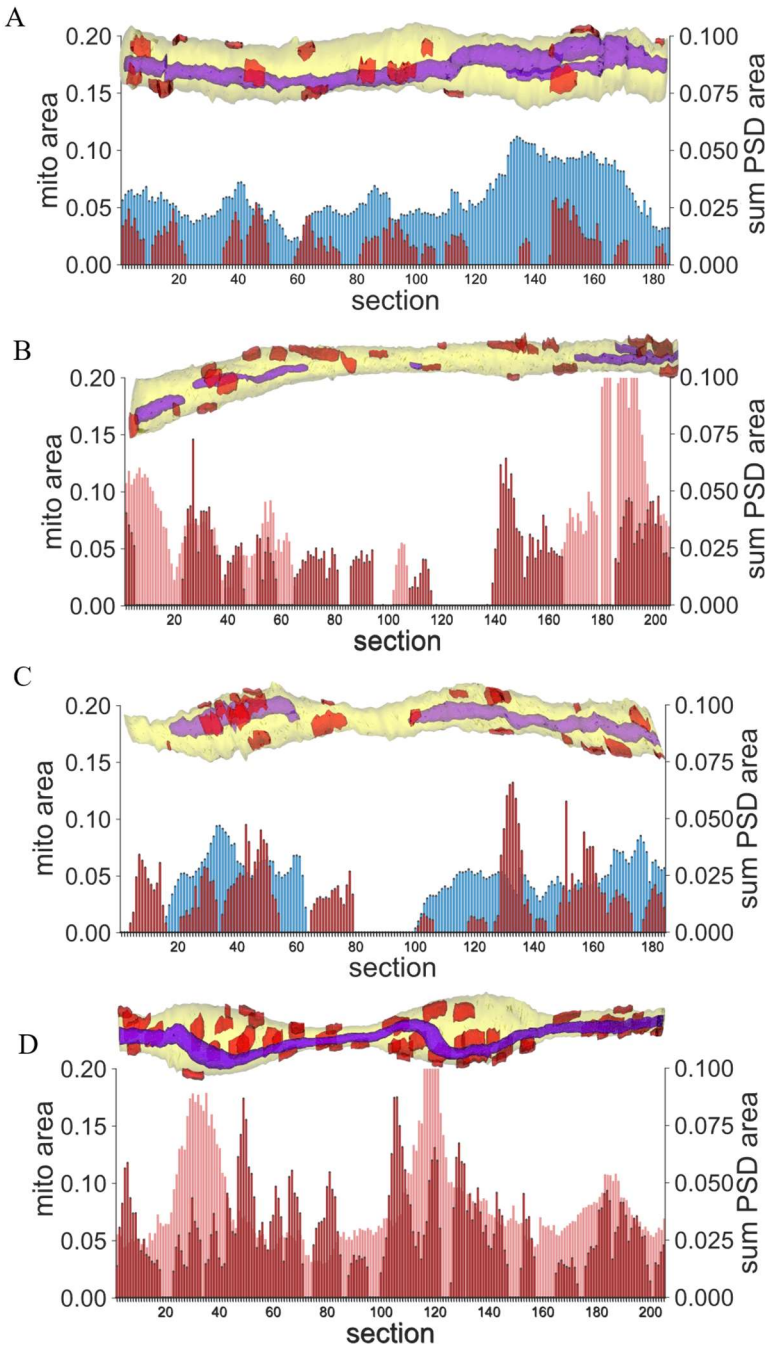

Figure 29. (A-B) Example smooth dendrites from control (mitochondria area per section—blue) and TBS (mitochondria area per section—red), mitochondria in reconstructions are purple, PSDs are dark red. (C-D) Example varicose dendrites from control and TBS (colors are same as A-B).

Figure 30 shows the change in mitochondrial distribution after TBS. Smooth region controls in both slices had almost no sections without mitochondria present, 96% of sections had mitochondria in slice 1 and 98.4% of traces had mitochondria in slice 2. These proportions dropped significantly after TBS in both slices—to 63% in slice 1 and 88% in slice 2. Curiously, mitochondria porportion changed in opposite directions in the varicose region sections of each slice, from 77% to 91% in slice 1 and fell from 93% to 84%. Inter-varicose region sections in both slices showed a dramatic increase in the proportions containing mitochondria, from 6% to 49% in slice 1 and from 12% to 33% in slice 2. These changes in mitochondria distribution do not completely track the changes in synapse size seen after TBS in the different regions in each slice, but they also do not appear completely unrelated. Mitochondria portion rose in all conditions where PSDs significantly enlarged and declined in regions where PSDs either decreased or did not change. All changes in mitochondria distribution were significant by χ^2 test. Smooth control (33/829), TBS (150/408), $p < 0.00001$; varicose control (58/247), TBS (154/1712), $p < 0.0001$; inter-varicose control (5/81), TBS (437/901), $p < 0.00001$. Slice 2 smooth control (7/430), TBS (66/536), $p < 0.00001$; varicose control (16/219), TBS (97/595), $p = 0.0035$; inter-varicose control (18/145), TBS (116/349), $p = 0.0002$.

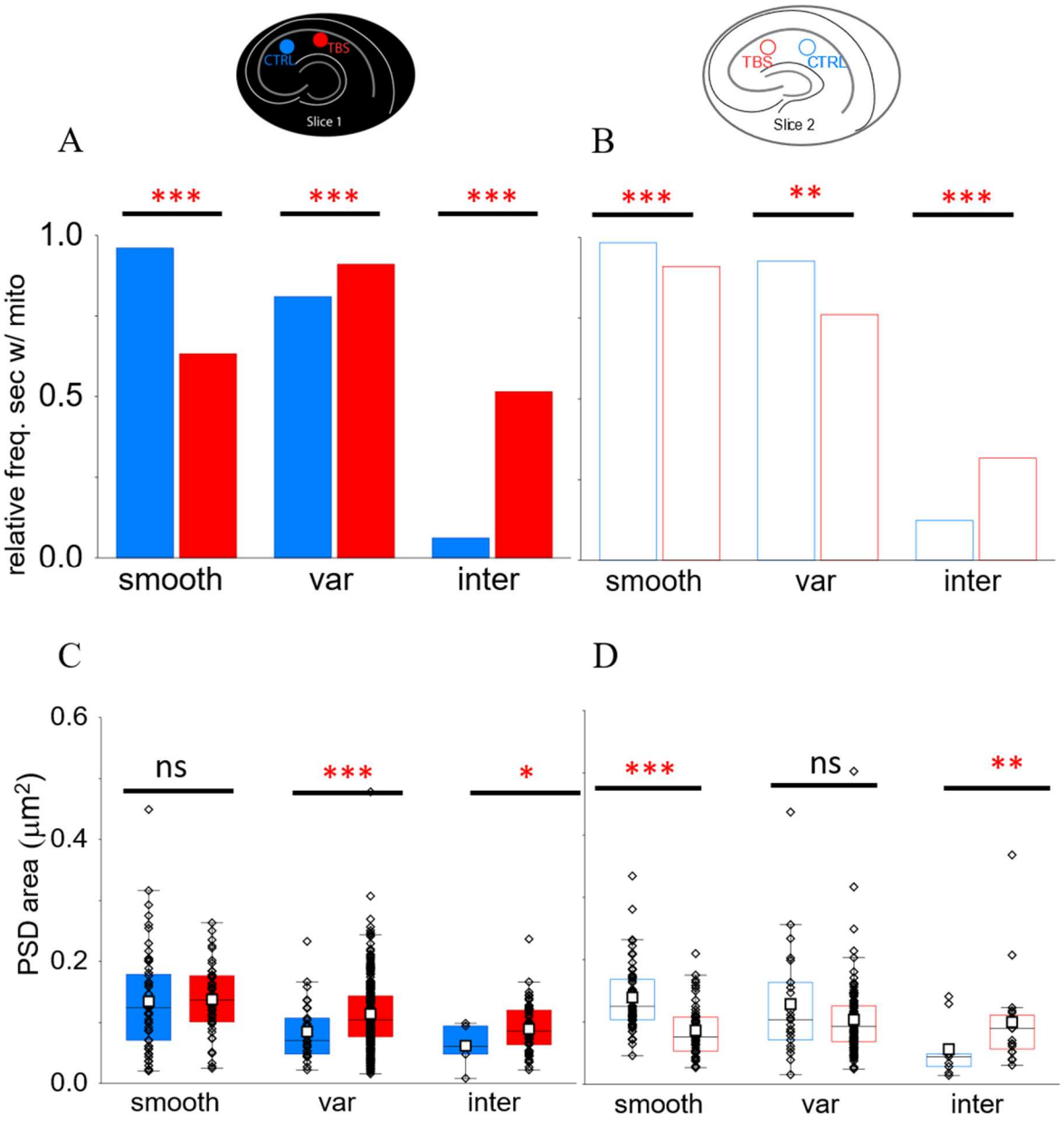

Figure 30. (A-B) Significant change in proportion of sections containing mitochondria in the different regions before and after TBS. (C-D) The changes in synapse area in the same conditions and regions as A-B. Mitochondria proportion increased in all regions where synapses increased. Mitochondria decreased where synapses got smaller or did not change compared with control.

Figure 31 shows a summary of the strong preference of synapses to occur close to mitochondria. Very few sections contained a synapse trace while also containing no mitochondria traces. The change in sections with synapse but without mitochondria mirrors that seen in the overall sections with mitochondria before and after TBS seen in Figure 30.

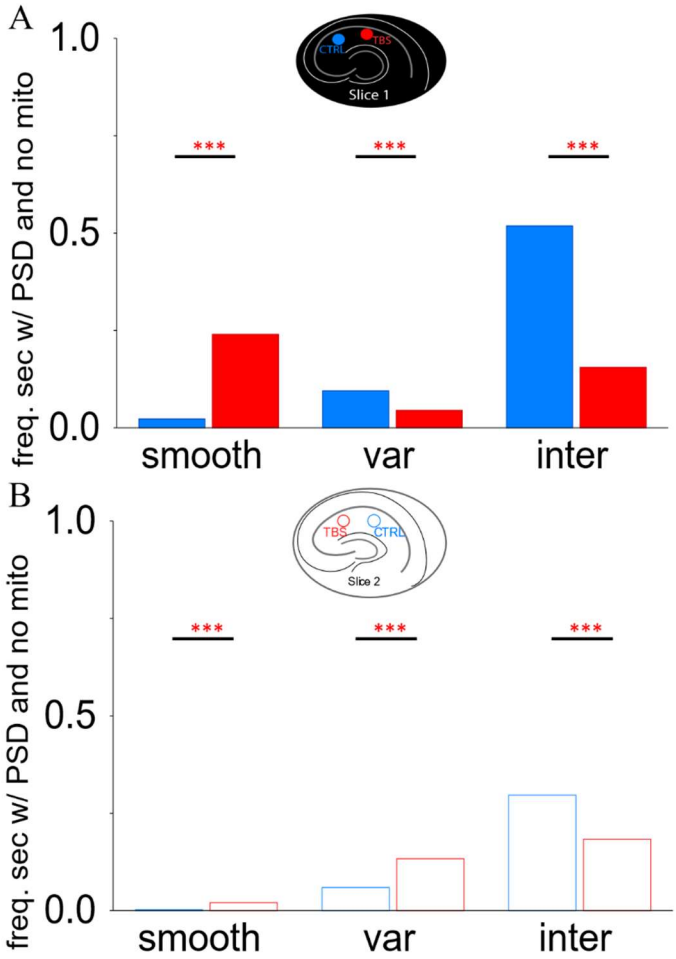

Figure 31. (A-B) Sections with synapse but without mitochondria are uncommon. The change in their proportions mirrors that seen in overall sections with mitochondria before and after TBS. Significance assessed with χ^2 test.

MITOCHONDRIA ADJACENT TO SYNAPSES

We showed in chapter 5 how the synapses changed compared to controls after TBS. We wanted to know if the total mitochondria volume adjacent to synapses, also changed. Comparison of slice controls to perfused tissue showed no significant differences between either slice controls or between controls and perfused. Curiously, no significant difference was found between control and TBS conditions in any region in either slice. Synapses with no mitochondria adjacent were excluded from this analysis.

No synapses with adjacent mitochondria were found in slice 1 control, two synapses with mitochondria were found in slice 2 control. Mitochondria volumes were log-transformed to obtain normal distributions for analysis of variance. Slice (including perfused) had a significant interaction with mitochondria volume/synapse (ANOVA, mito vol/synapse*slice, $F_{2,230} = 3.06$, $p = 0.049$). Slice 1 (n=81), slice 2 (n=85), perfused (n=69) smooth control (1: 0.028±0.005μm^3 – 2: 0.307±0.047μm^3 –perf: 0.0295±0.004μm^3 ; 1vs.2, p = 0.652; 1vs.perf, p = 0.999; 2vs.perf, p = 0.999), slice 1 (n=27), slice 2 (n=23), perfused (n=41) varicose control (1: 0.027±0.006μm^3 – 2: 0.04±0.004μm^3 – perfused: 0.031±0.0094μm^3; 1vs.2, p = 0.519; 1vs.perf, p = 0.997; 2vs.perfused, p = 0.823), slice 1 (n=0), slice 2 (n=2), perfused (n=6) inter control (2: 0.023±0.023μm^3 –perfused: 0.011±0.007μm^3 ; 2vs.perfused, p = 0.999). Slice 1 TBS region compared with its within-slice control. Mitochondria area per synapse was significantly different between positions (nested ANOVA, synapse position(condition), $F_{3,376} = 7.03$, $p = 0.00013$). Smooth control (n=54) 0.042±0.0044μm^3, smooth TBS (n=31) 0.031±0.006μm^3 $p > 0.1$; varicose control 0.027±0.006μm^3, TBS.041±0.002μm^3

$p > 0.1$; no inter control, TBS inter $0.019 \pm 0.005 \mu m^3$. No significant difference between conditions. Slice 2 TBS region compared with its within-slice control. Mitochondria volume per synapse was significantly different between positions (nested ANOVA, synapse position(condition), $F_{4,239} = 16.78$, $p < 0.00001$). Smooth control (n=60) $0.04 \pm 0.0044 \mu m^3$, smooth TBS (n=114) $0.047 \pm 0.0045 \mu m^3$ $p > 0.1$; varicose (n=23) control $0.041 \pm 0.0067 \mu m^3$, TBS $0.048 \pm 0.003 \mu m^3$ $p > 0.1$; inter (n=2) control $0.023 \pm 0.023 \mu m^3$, TBS inter (n=8) $0.013 \pm 0.011 \mu m^3$ $p > 0.1$. No significant difference between conditions. See Figure 32 for summary plots.

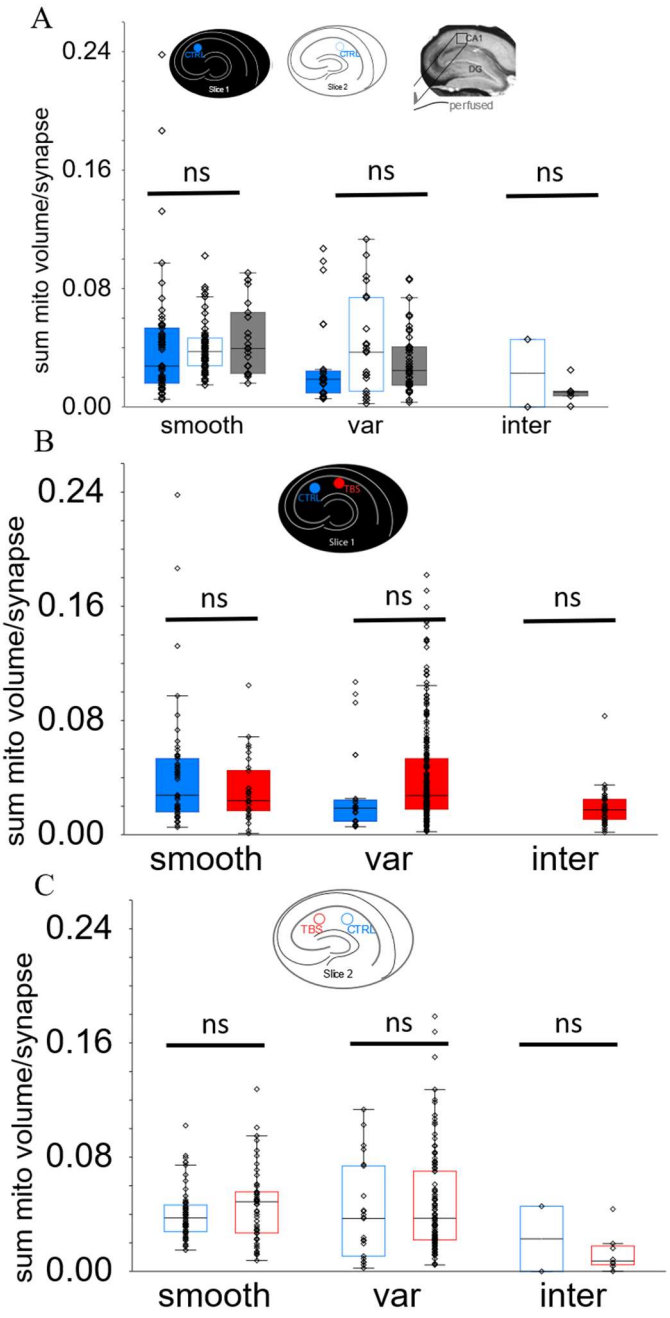

Figure 32. (A) No significant difference in mitochondria volume/synapse between control regions. (B-C) No significant differences in mitochondria volume/synapse between conditions by region. Inter-varicose regions are shown but the main finding was the increase in mitochondria presence after TBS.

SYNAPSE SIZE AND ADJACENT SUMMED MITOCHONDRIA AREA ARE CORRELATED

Since mitochondrial presence has been shown to affect synaptic plasticity (Todorova & Blokland, 2017) and correlate with synaptic activity and LTP in pyramidal cells, we asked what relationship might exist between synapse size and adjacent mitochondria. Figure 33 shows the linear relationship between synapses and mitochondria in perfused control tissue for smooth, varicose, and inter-varicose regions.

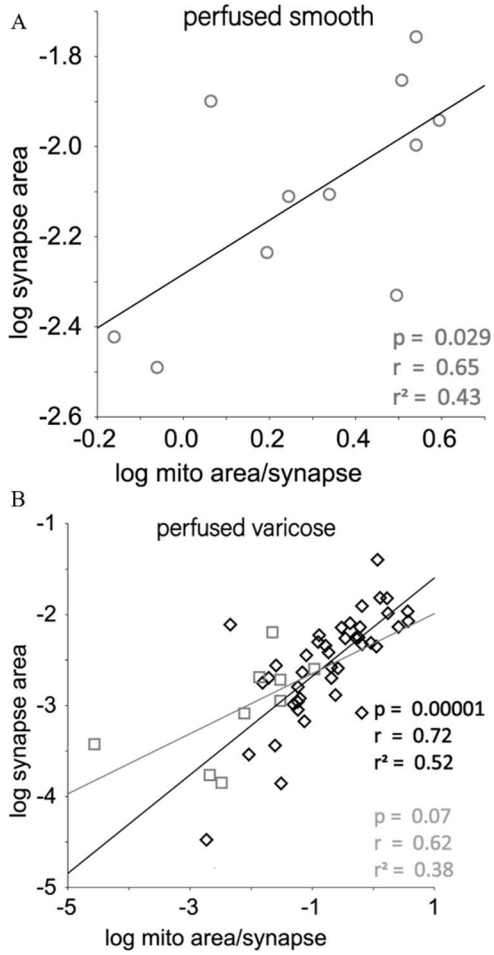

Figure 33. (A) Regression analysis between synapse area and adjacent mitochondria for perfused smooth dendrites. (B) Regression analysis between synapse area and adjacent mitochondria for perfused varicose region and inter-varicose region dendrites.

For all regions the correlation is positive. In both smooth and varicose regions, the correlation is also significant, and the large r^2 values (see Figure 33) indicate a large portion of the variance in synapse size is accounted for by the variation in adjacent mitochondria. This suggests a strong coupling between mitochondria and synapse size, at least in the unstimulated perfused tissue.

TBS CHANGES THE CORRELATION BETWEEN MITOCHONDRIA AND SYNAPSE SIZE

The near complete lack of mitochondria in inter-varicosities occurring in control conditions prevented comparing the effect of TBS on these regression analyses; nevertheless, comparison of the TBS inter-varicose relationship with perfused is possible. For all regions of perfused dendrite there was a significant positive linear relationship between synapse size and mitochondria. All slice control regions had significant had similar correlation coefficients to perfused. Figure 34 shows the regions where significant changes in the correlation between synapses and mitochondria occurred. These changes are interesting given that total mitochondrial volume adjacent to the synapses did not significantly change in any region after TBS and the total quantity was not different between control conditions in slice or perfused tissue.

In slice 1 smooth regions, the synapse size did not change after TBS, but the sections containing mitochondria decreased. The significant correlation in control condition was no longer significant after TBS. For the slice 1 varicose region synapses which were significantly larger after TBS, the correlation became stronger. In slice 2 smooth region synapses, which were smaller after TBS, the correlation and determination coefficients decreased only slightly. See Figure 34 for relevant r-, r^2-, and p-values.

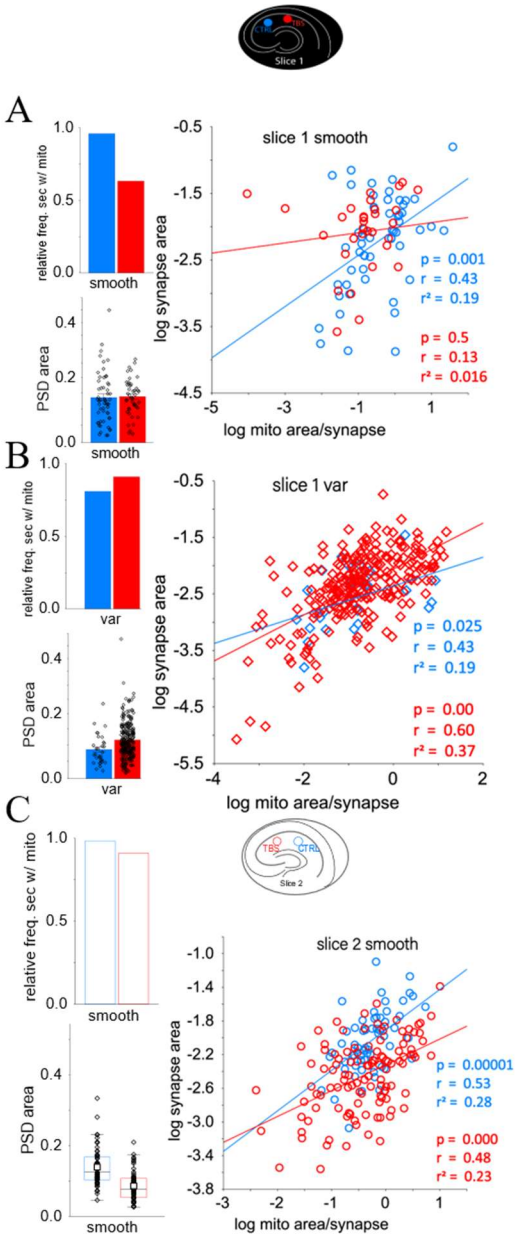

Figure 34. (A) Slice 1 smooth, no change in synapses, decreased sections with mitochondria, the correlation lost significance. (B) Slice 1 var, synapses increased, sections with mitochondria increased, correlation and determination coefficients both increased. (C) Slice 2 smooth, significant decrease in synapse size, decrease in sections with mitochondria, significant positive correlation remained, both coefficients slightly decreased.

MITOCHONDRIA – SUMMARY

The association between varicosities and mitochondria has been remarked upon many times in the literature (Freund & Buzsáki, 1998; Kawaguchi et al., 1993). We found that mitochondria are in fact more common at smooth regions, though their association with varicose regions is very strong. Interestingly, the relationship between mitochondria and inter-varicosity regions may prove the most revealing. In control conditions in slice, mitochondria were rare between varicosities, but after LTP was induced in the slice the portion of inter-varicose sections containing mitochondria increased drastically. This finding is consistent with previous reports that mitochondria actively move towards activated synapses (Li et al., 2004), but the snapshots afforded by EM reconstruction cannot distinguish if mitochondria are relocating, expanding, or if some other mechanism is responsible for their increase in inter-varicose regions.

Yet these data concur with numerous findings describing an important role for mitochondria in supporting synaptic activity in interneuron dendrites (Ichas et al., 1997; Kann, 2012; Kann et al., 2011, 2006; Müller et al., 2005; Sparagna et al., 1995). It is known that fast spiking interneurons have exceptionally high energy demands (Buzsáki et al., 2007). In the next chapter we will examine the relationship between energy reserves stored in the neurons as glycogen and how this relates to dendrite structure, mitochondria distribution, and synapses.

Chapter 6: Results – Glycogen

INTRODUCTION TO GLYCOGEN

Glycogen is a randomly hyperbranched glucose polymer. Glucose is a six-carbon hexose sugar molecule and serves as an important source of fuel for most organisms, from bacteria to humans. Its use for energy generation can be aerobic, as when it is used by mitochondria for the generation of ATP via oxidative phosphorylation, or anaerobic as in fermentation. Glucose is the primary energy source used in brain tissue (Carlson et al., 2018). The transformation of glucose molecules into glycogen is critical for maintaining neutral osmolarity, as the ~55,000 glucose residues that form a typical β-particle eliminates the osmotic pressure difference that would occur if all glucose molecules were dissolved (Carlson et al., 2018).

The generation of glycogen from glucose depends on the cooperation of glycogen synthase, glycogenin, and glycogen branching enzyme. Glycogen synthase is the only enzyme in the mammalian genome capable of catalyzing the linkage of glucose residues (Valles-Ortega et al., 2011). It cannot accomplish this alone, as it requires a pre-existing chain of 4 or more α1,4-linked glucose residues in order to bind and extend the chain (Roach et al., 2012). Glycogenin forms the nucleus of every glycogen particle as its structure mimics the linked glucose chain. Glycogenin contains a glycogen synthase binding domain that is extremely conserved, enough so that human glycogenin is capable of binding both human and yeast glycogen synthase. Glycogen branching enzyme randomly induces α1,6-linkages which glycogen synthase then extends via continuing

α1,4-links (Roach et al., 2012). When fully elaborated by glycogen synthase and glycogen branching enzyme, the resultant β-particles contain ~55,000 glucose residues and comprise a rough spheroid measuring from 10-40nm in diameter in muscle and brain tissue (Marchand et al., 2002). These dimensions are consistent with the glycogen particles found in astrocytes and those we describe here in interneuron dendrites.

Glycogen has been called the depot into which excess glucose is stored in mammals and acts as a source of rapidly available energy substrate (Waitt et al., 2017). Most glycogen is stored in the liver, but other cell types, especially muscle and endocrine tissue, are known to contain the enzymes necessary for its synthesis and metabolism. Astrocytes in the brain have long been known to store glycogen particles and are often believed to be the primary means of moving glucose from the blood and making it available to neurons in the form of the lactate shuttle (Mangia et al., 2009). Several neurological disorders are characterized by the pathological accumulation of glycogen, particularly Lafora disease (Turnbull et al., 2012; Valles-Ortega et al., 2011). Neural diseases associated with glycogen abnormalities and the inability of traditional assays to detect the low concentrations of glycogen in neurons had led many researchers to doubt any active role for glycogen in normal operations of neural cells.

However, it has recently been shown that neurons express both glycogen synthase (GS) and an isoform of glycogen phosphorylase—brain glycogen phosphorylase (bGP), the enzyme necessary for hydrolyzing glucose residue linkages and making glucose available for metabolism. Neurons thus possess all the machinery necessary for the metabolism of glycogen (Saez et al., 2014). Astrocytes express both bGP and muscle GP

while neurons exclusively express bGP. When cultured with media containing high glucose concentration, astrocytes accumulate glycogen in proportion to the levels of glucose. In contrast, neurons similarly cultured in high glucose media maintain a constant level of glycogen, suggesting more complex regulatory mechanisms (Saez et al., 2014). Further, for several of experiments conducted by Saez et al. (2014), parvalbumin expressing neurons were used because they are known to express high levels of GS (Valles-Ortega et al., 2011). PV interneurons are the most common type of fast-spiking cells and high frequency oscillations, which are sensitive to behavioral states and mnemonic processes, depend on their function (Sohal et al., 2009).

Gamma oscillations are a group of high frequency (~25-100Hz) intrinsic rhythms detectible in many areas of the mammalian brain including the hippocampus, and they reflect the synchronized activity of large numbers of neurons (Colgin, 2016). Interneurons are known to discharge at gamma frequency and basket cells, most of which express PV, are phase locked to the fast oscillations of the local field potential, while pyramidal cell discharges are not (Penttonen et al., 1998).

It has been shown that glycogen depletion almost completely suppresses gamma rhythms in hippocampal slice and slice cultures (Galow et al., 2014) when neurons are deprived of glucose in their support media. Gamma oscillations can persist for ~30 minutes following complete glucose deprivation, suggesting the neurons responsible for entraining gamma maintain a reserve of energy. That this energy reserve is specifically in the form of glycogen was shown by inhibiting glycogen phosphorylase. Under these conditions, where the cells are unable to liberate glucose residues from glycogen

polymers, gamma is completely suppressed by 8 minutes following glucose deprivation. Further, supplying lactate or pyruvate does not recover the oscillations unless given at significantly higher concentrations, even then gamma shows significantly lower power as well as frequency abnormalities (Galow et al., 2014). We mentioned the high energy requirements of fast-spiking interneurons (Kann et al., 2014) in chapter 6 with regards to mitochondrial ATP supply, yet mitochondria require both oxygen (Huchzermeyer et al., 2013) and glucose to support cellular respiration and generate energy. Interneurons are uniquely capable of controlling both oxygen availability and glucose supply. Traditionally, the link between neural activity and blood flow was thought to be mediated by the glia (Magistretti, 2017; Magistretti, 2011) although alternative hypotheses based on the presence of neural metabolites is common (Kleinfeld et al., 2011; Moore & Cao, 2008; Roy & Sherrington, 1890). Of the major neuropeptides used to classify interneuron subtypes, four of the most common are capable of directly influencing local hemodynamics by acting on the vasculature. Nitric oxide and vasoactive intestinal peptide are vasodilators, acting to increase local blood flow. Somatostatin and neuropeptide Y are vasoconstrictors, acting to decrease it (Desai et al., 2011). Remarkably, it has recently been shown that the specific activation of PV-expressing neurons by restricted expression of channelrhodopsin caused robust changes in local blood vessel diameter, usually constriction. These findings in the somatosensory cortex of mouse also confirmed earlier reports that a small set of pyramidal cells outside of the hippocampus also express PV and their activation was also tightly linked to blood dynamics (Urban et al., 2012).

With their high energy demand and the highly contingent dynamics of local blood flow, it is not unreasonable to think that neurons with constitutively high activity should have some mechanism to hold necessary energy reserves in the face of variable blood supply.

We report our findings on glycogen prevalence in aspiny dendrites, its distribution, and how these features respond after the induction LTP.

GLYCOGEN IS ENRICHED IN ASPINY DENDRITES

While looking carefully for interneuron dendrites in these EM series, one striking feature rapidly became apparent—these aspiny dendrites in fact exhibited high levels of glycogen. This feature was so striking that identifying interneuron dendrites by finding the glycogen was far easier than looking across 1-2 μm only to find a spine.

The appearance of glycogen in ultrathin brain sections is well known from astrocytes, and astrocytic processes are not easily mistaken for dendrites. Figure 35 shows examples of identified glycogen particles in an astrocytic process taken from the Atlas of Ultrastructural Neurocytology.

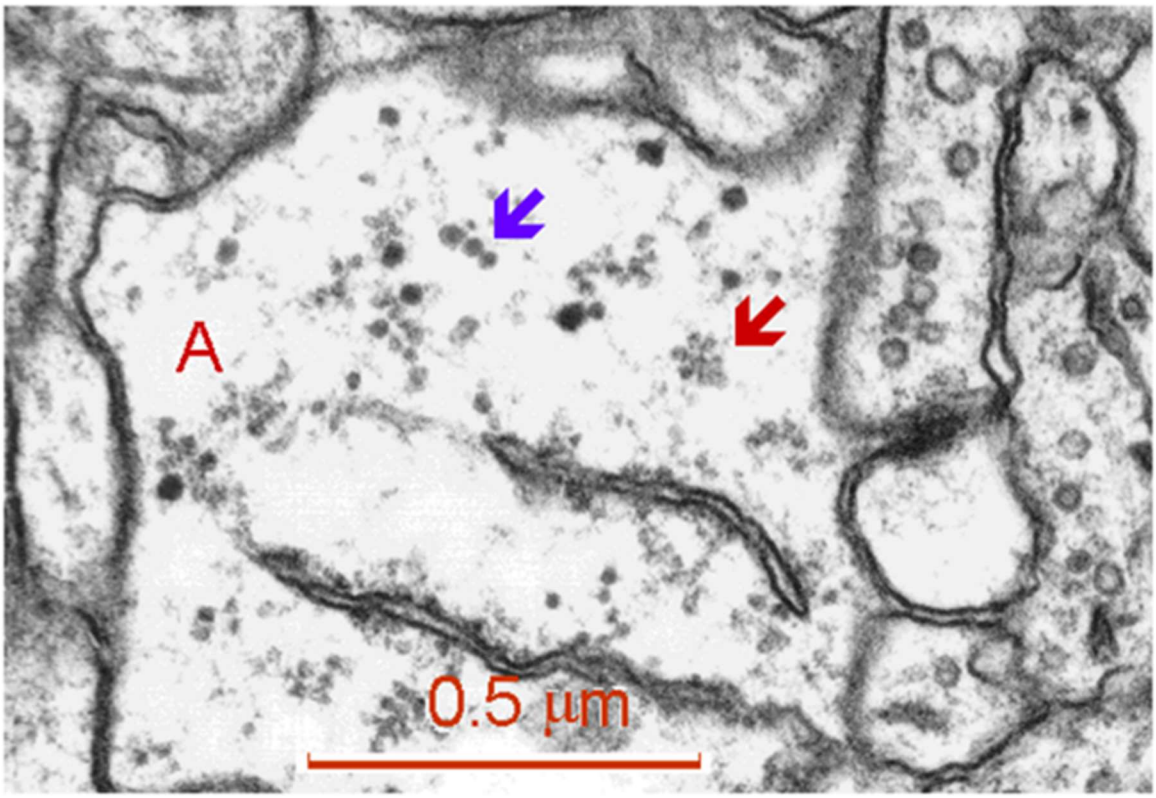

Figure 35. Elementary glycogen granules (blue arrow) are similar in appearance and size with ribosomes (red arrow). A - the cytoplasm of the astrocyte process. Scale = 0.5µm. Adapted from Atlas of Ultrastructural Neurocytology, http://synapseweb.clm.utexas.edu/atlas.

Glycogen particles were extremely enriched in interneuron dendrites compared to nearby pyramidal cell spiny dendrites. Figure 36 shows an example of the drastic difference in glycogen concentration between inhibitory and excitatory neuron dendrites.

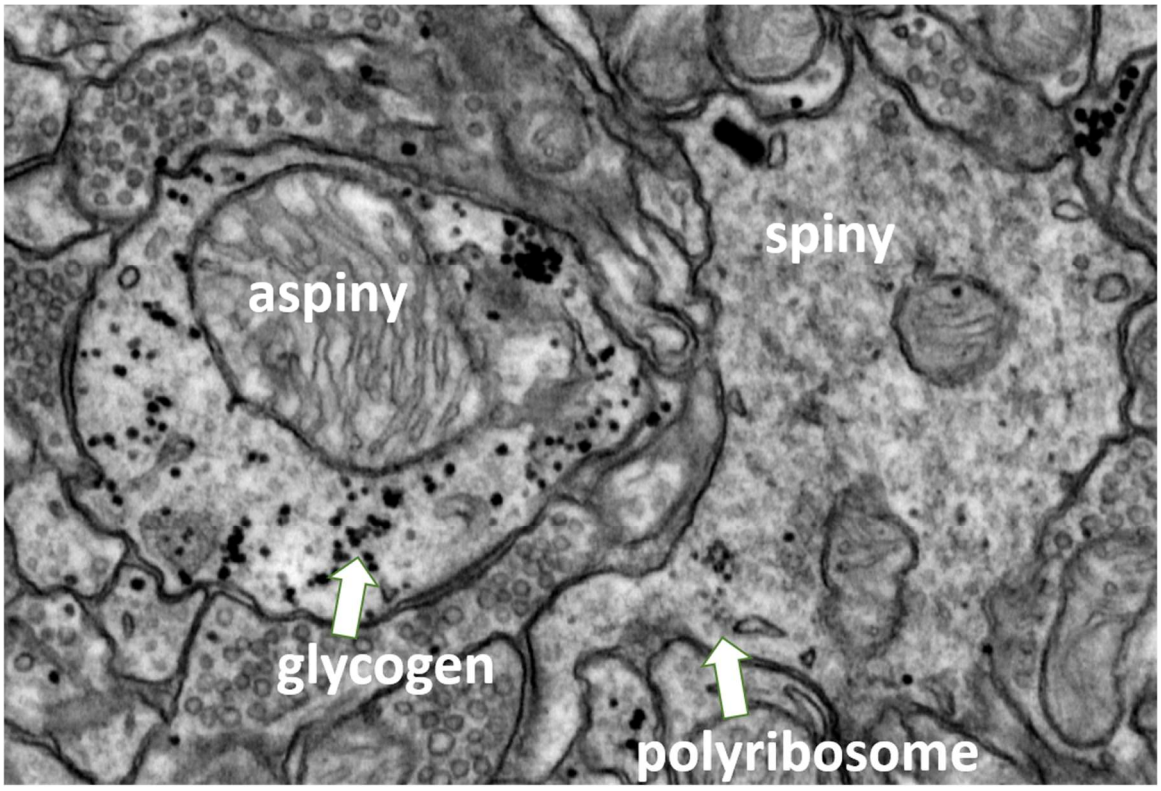

Figure 36. The labeled aspiny dendrite contains numerous glycogen particles similar in appearance to glycogen identified in astrocytes. Glycogen tends to appear in the vicinity of mitochondria, the large membrane bound structure within the aspiny dendrite. An adjacent spiny pyramidal cell dendrite shows little or no glycogen by contrast. Polyribosomes are labeled in the spiny dendrite.

Glycogen was enriched in both smooth and varicose aspiny dendrites (Figure 37). The presence of mitochondria was associated with the probability of finding glycogen.

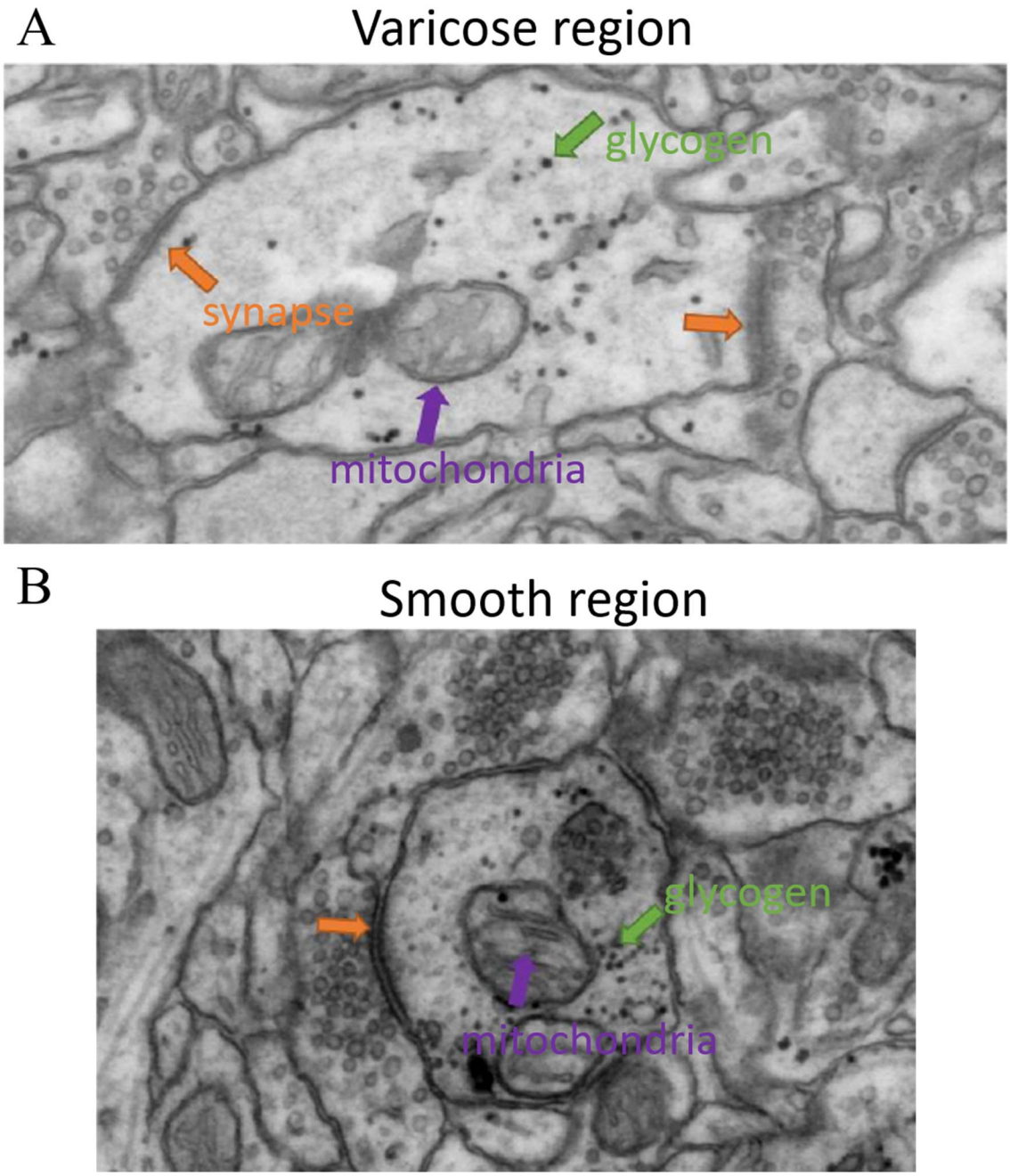

Figure 37. Glycogen is enriched in both varicose (A) and smooth (B) aspiny dendrites. Glycogen was frequently found near both synapses (orange arrows) and mitochondria (purple arrows).

Glycogen concentration was different between region types. Smooth regions consistently had the most glycogen particles per section with varicose region sections showing an intermediate quantity and inter-varicose regions showing the least. Figure 38 shows the quantity of glycogen per section per region.

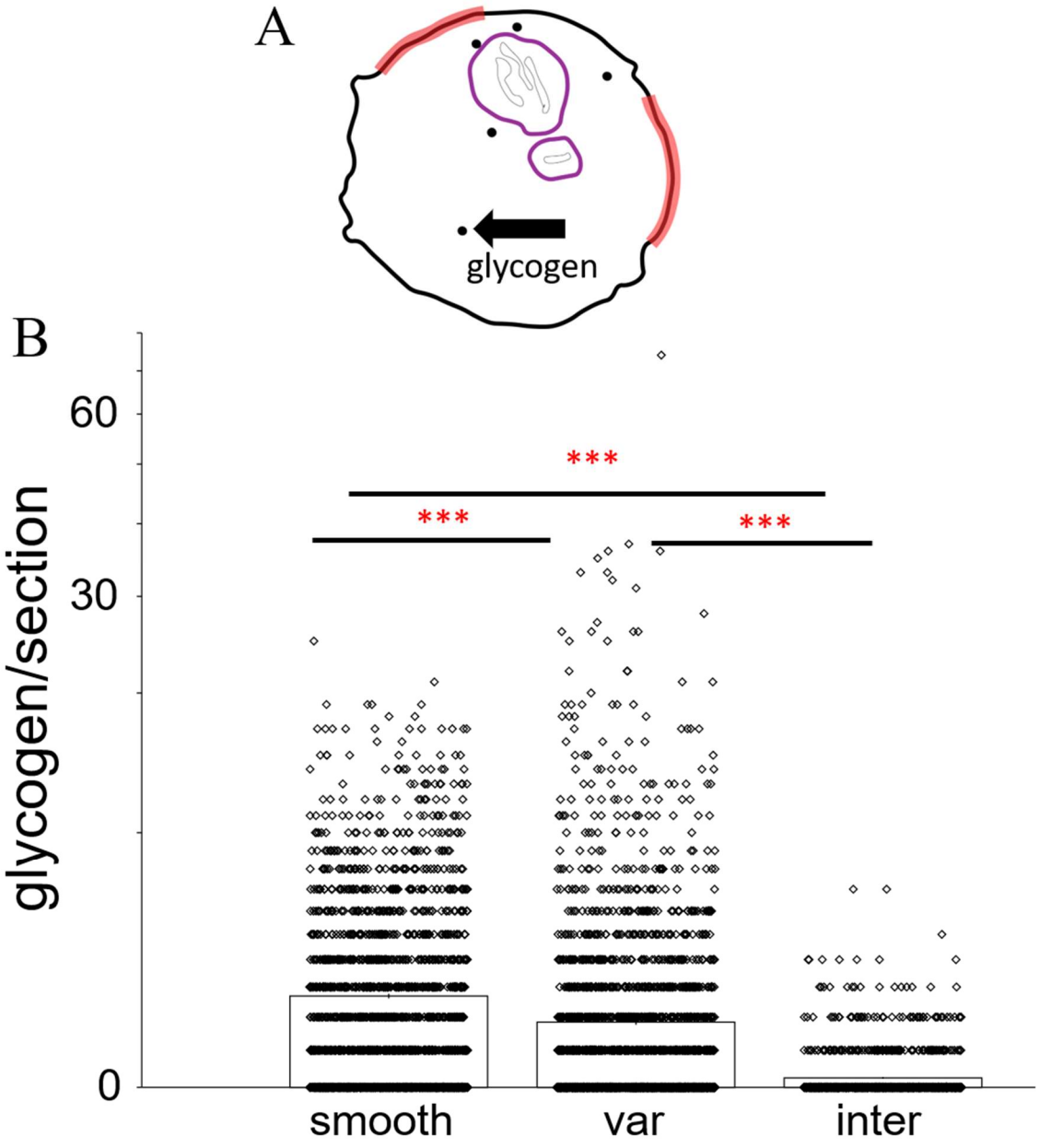

Figure 38. (A) Schematic of a section here showing glycogen particles. (B) Region types has different quantities of glycogen on average. Smooth regions have the highest glycogen abundance, significantly higher than varicose and inter-varicose regions. Varicose regions have higher glycogen than inter-varicose.

Glycogen significantly differed by region type (ANOVA, $F_{2,5725} = 193.75$, $p < 0.00001$). Means and standard errors of glycogen per section are as follows. Smooth region (n = 2008), 2.6±0.077; varicose region (n = 2484), 1.9±0.07; inter-varicose region (n = 1236), 0.244±0.098; $p < 0.00001$ for all pairwise comparisons, Tukey's HSD.

Glycogen tended to occur in sections that also contain mitochondria. Figure 39 shows example per section plots showing the coincidence of mitochondria and glycogen per section.

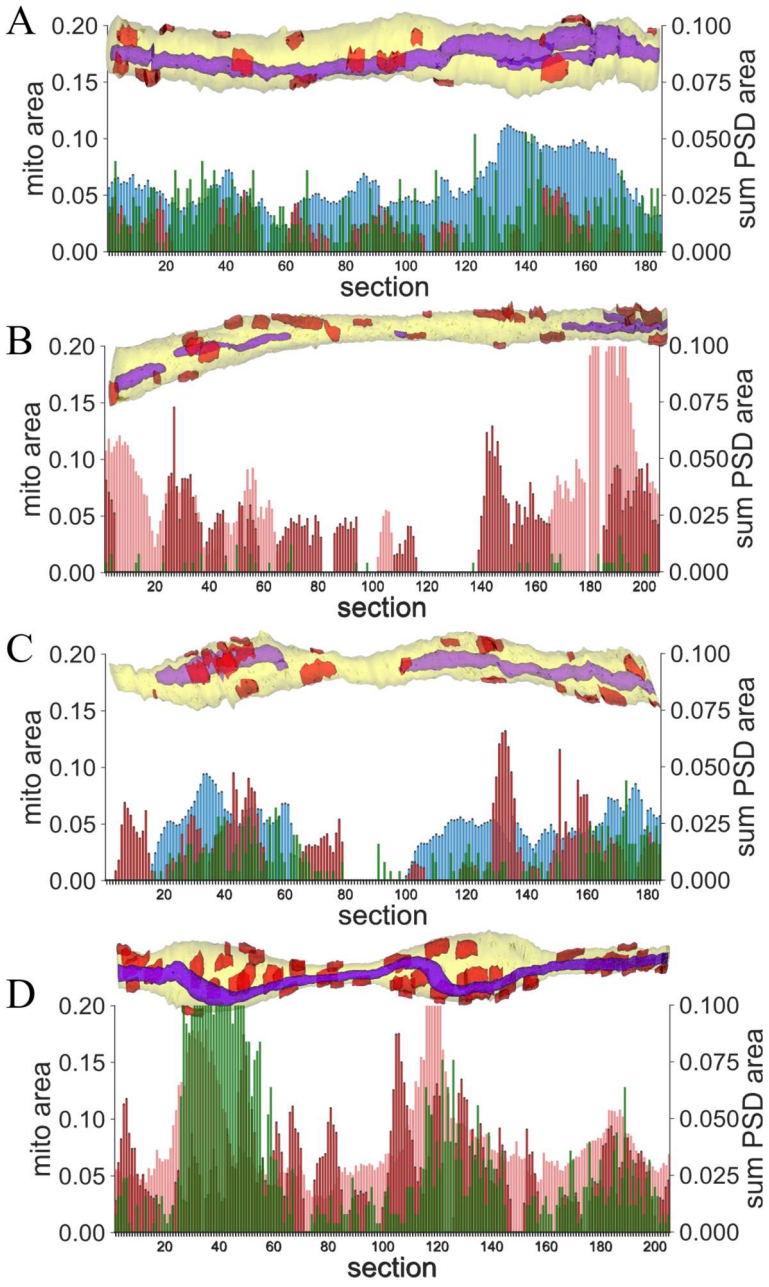

Figure 39. Example section plots with dendrite reconstructions. (A-B) Smooth control and TBS. (C-D) Varicose control and TBS. Blue and light red bars are mitochondria area per section. Dark red bars are PSD length per section. Glycogen quantity are green bars, scale is related to the X-axis in particles/section, i.e., 0.2 = 20 particles.

Figure 40 shows a summary of the portion of sections that contained no mitochondria and no glycogen, mitochondria with no glycogen, and glycogen with no mitochondria.

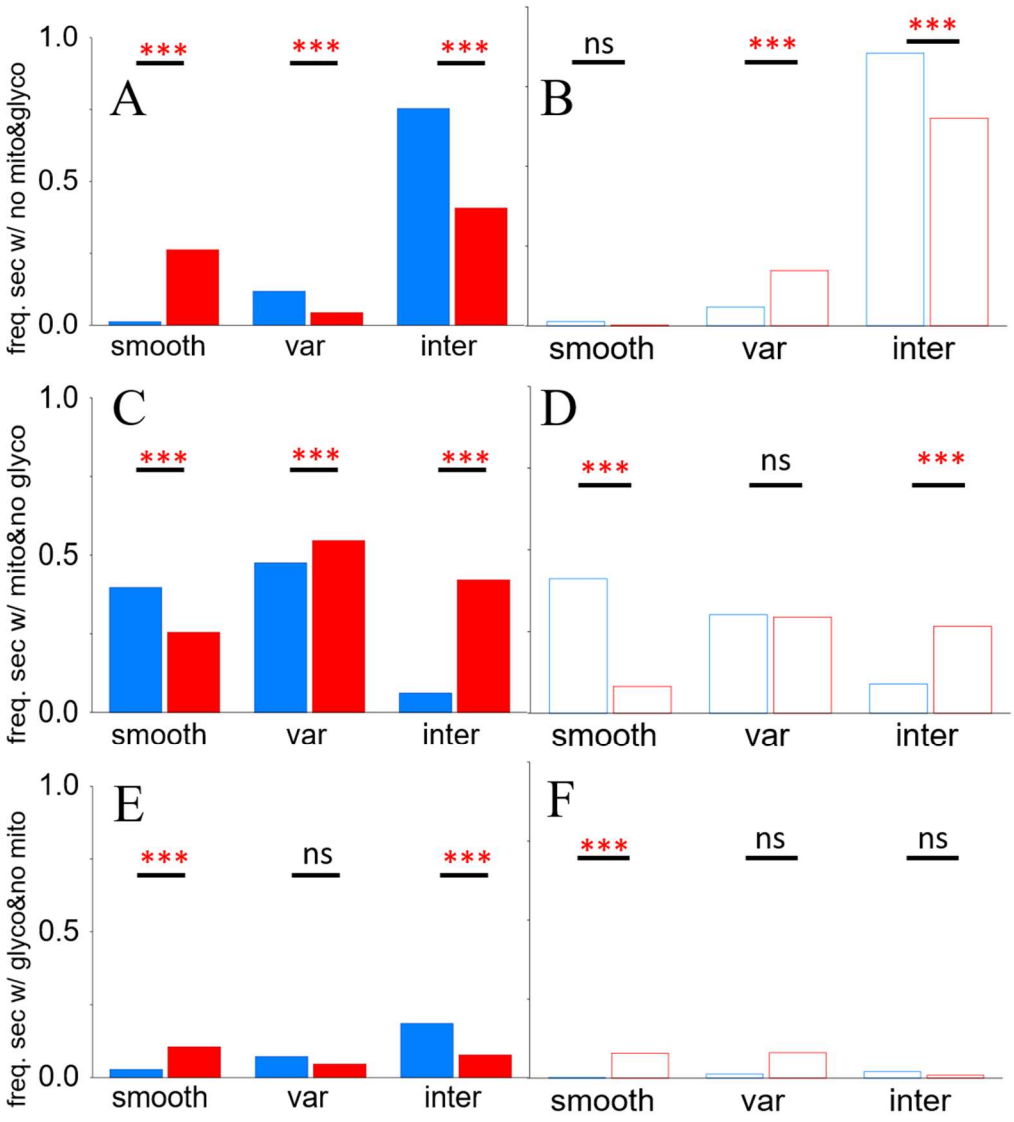

Figure 40. (A-B) Slice 1 and 2 portion of sections per region and condition with no mitochondria and no glycogen. (C-D) Same but sections with mitochondria and no glycogen. (F-F) Same but sections with glycogen only and no mitochondria.

We know from Figure 30 that mitochondria appear in the majority of sections from smooth and varicose regions in both conditions though the portion is altered by TBS, increasing where synapses enlarged and decreasing where synapses decreased or did not change. The exception was inter-varicose regions, where mitochondria-containing sections were rare in control conditions but drastically increased after TBS. Figure 40 shows that less than 20% of smooth and varicose sections lack mitochondria and glycogen, with only slice 1 TBS approaching 20%, all other smooth and varicose regions had less than 10% of sections with no mitochondria or glycogen. Contrasting this, the inter-varicose regions from both slices showed large proportions of sections without mitochondria and glycogen in control, which both fell significantly after TBS. In Figure 40 (C-D) it is apparent that mitochondria can often occur without glycogen present, but from (E-F) the converse is not true—there were very few sections with glycogen that did not also contain mitochondria.

GLYCOGEN AND SYNAPSES

Glycogen particles per synapse remained constant between conditions for all but one region in one slice. The only significant change in glycogen was in slice 2 TBS smooth region synapses which increased compared to control. This is the only dendrite region type where synapses significantly decreased in size after TBS. In the other conditions where there was no change or an increase in synapse area, there was no change in glycogen. This result is curious given that the count of glycogen particles per synapse depends on the size of the synapse as well as the number of coinciding particles.

As the synapses shrank compared to controls in slice 2 smooth region there was less area over which to include glycogen yet the total number of particles per synapse increased. One possible explanation for this is that a decrease in synaptic area is associated with LTD and a decrease in synaptic activity. If a major role of dendritic glycogen is to support active synapses, this increase could reflect a lower ongoing utilization of energy reserves, allowing it to increase to its preferred set point. As noted, neurons tend to maintain stable levels of glycogen despite changes in local glucose availability (Saez et al., 2014). For detailed summary graphs of mitochondria distribution, synaptic glycogen, and synapse area changes, see Figure 41.

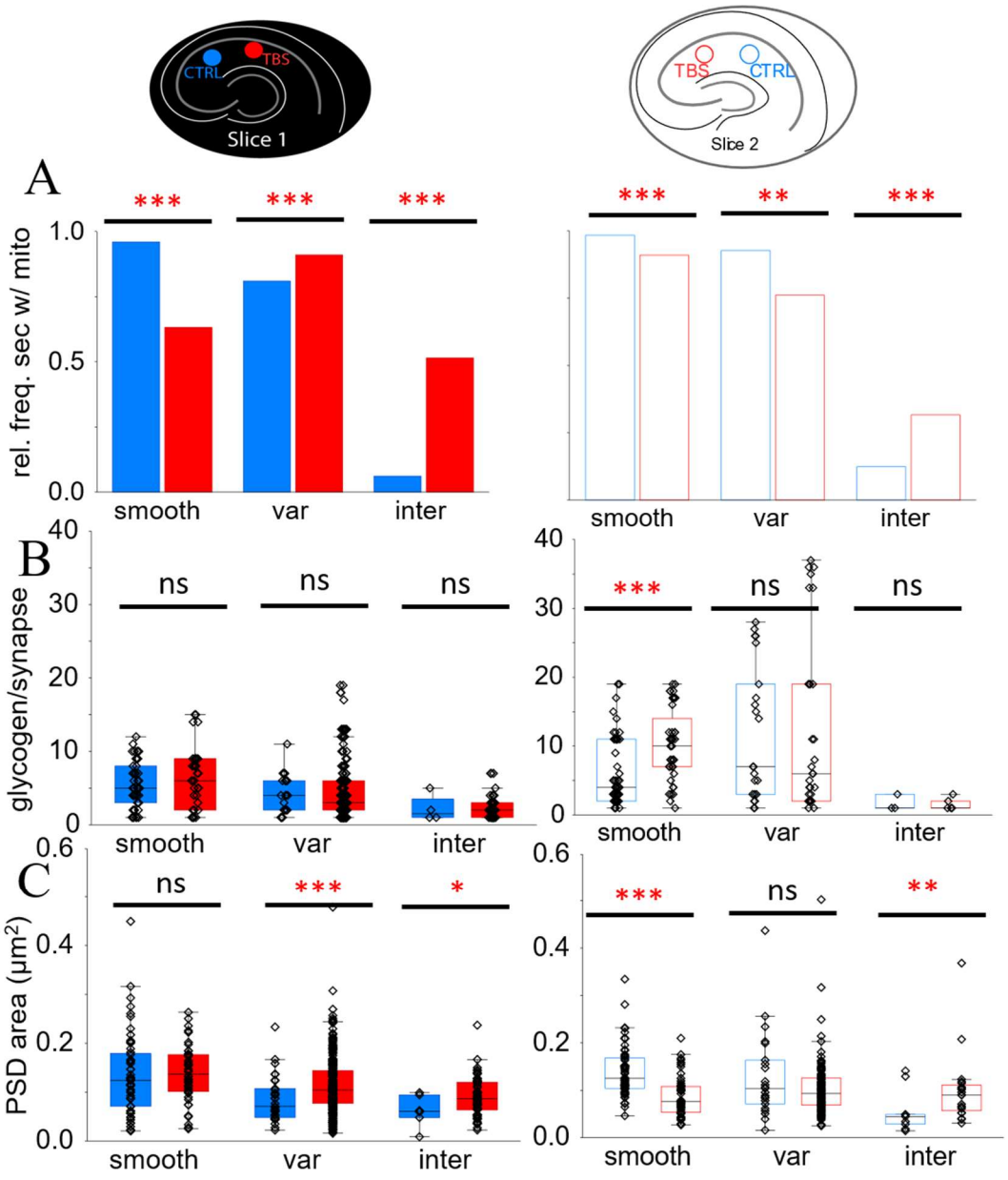

Figure 41. (A) The change in section portion with mitochondria by condition and slice. (B) The effect of TBS on glycogen particles per synapse—no change occurred except in slice 2 smooth region synapses which significantly decreased in size after TBS. (C) The effects of TBS on synapse size by region and slice. Mitochondria per section portion changes the same way depending on whether synapses enlarged or shrank.

GLYCOGEN – SUMMARY

These detailed EM quantifications of the distribution of glycogen particles in aspiny interneuron dendrites are consistent with the numerous findings reporting high energy demand by the many types of fast spiking and burst firing inhibitory neurons in the hippocampus and other regions of the brain (Gulyás et al., 2010; Kann, 2012; Kann et al., 2016, 2011, 2014; Vodovozov et al., 2018). An accurate understanding of the connection between energy demand, blood supply, and neural information processing is a major goal for modern neuroscience. Our findings on the distribution of glycogen particles in aspiny interneuron dendrites may prove useful by providing empirical data on energy reserves and some constraints for modeling. This is especially important given that non-invasive neuroimaging techniques rely on detecting changes in cerebral blood flow. The BOLD signal from functional magnetic resonance imaging (fMRI) assumes a tight coupling between neuronal activity and blood dynamics (Hillman, 2014). Better understanding of the relationship between nervous activity and blood flow will improve the interpretation of BOLD signals and increase the accuracy of both research and clinical studies.

The findings on the close association between glycogen and mitochondria and the association between mitochondria and synapses supports theories about the important relationship between energy supply, resource availability, and information processing by biological neural networks, all of which provide important constraints on one another.

Chapter 7: Discussion and future directions

We found that the previously identified aspiny dendrite morphologies of smooth and varicose (Cowan et al., 1990; Defelipe et al., 2013; Freund et al., 1996; Kageyama et al., 1982; Kawaguchi, 1993; Kita et al., 1990; Ascoli et al., 2008) found in light microscopy were also apparent in 3DEM reconstructions. We also found that these types could be robustly distinguished by quantitative measurements of their anatomical parameters. Smooth, varicose, and inter-varicose regions were readily distinguishable by their cross sectioned area, the maximum/minimum ratio in a region, and the variance within a region. We found that the regions have characteristic morphological properties that did not change between condition in either slice and were not different from the perfused control dendrites, particularly diameter and average length of varicose and inter-varicose regions.

The different regions all contained synapses with smooth regions tending to have the largest and inter-varicose the smallest. On varicose dendrites, the varicosities contained on average 80% of all synapses across both slices in TBS and control conditions and in perfused tissue. There was variation in this proportion by dendrite. Ideally, we would be able to relate these proportions to the molecular identity of the parent interneurons. Such a mapping would be of great use if subtypes with different membrane responses, expression profiles, roles, and network positions prefer stereotypical synaptic distributions this would provide clues to the functional roles these fine structures underlie. Further, if the variation seen in synaptic distribution between

varicose and inter-varicose regions is explained by the parent subtype and we can identify these, we would have a much stronger basis for understanding structural synaptic plasticity.

Among our many findings, one stands out as particularly suggestive—the similarity in the size of synapses in the control regions of both slices and the perfused tissue. Finding this similarity depended on distinguishing the fine structures, as the synapse sizes were only similar when the same region types were compared. This is even though the molecular identity of the dendrites is under no constraint to be the same, either within one control region or across all control regions. The dendrites may all be from the same subtype of interneuron, or they may all be from different types. We do not know. But the tendency for unstimulated synapses (perfused condition) and synapses that received only control stimulation (one pulse every 2.5 minutes) to display no significant differences in size across the dozens of dendrites in these conditions suggests that the fine structures may be supporting similar tasks.

Such similarities between control regions and perfused tissue were seen before in pyramidal cell dendrites (Bourne et al., 2011a) in this tissue at the same 2 hour time point. But that this should be the case for interneuron synapses is curious. Pyramidal cells form a predominantly homogeneous group. Interneurons are not a homogeneous group and there is no *prima facie* reason why their synapses should be so similar in control regions and perfused. Either slices taken at approximately the same distance from the septal pole from animals of nearly identical age and weight have very similar distributions of interneuron subtypes or interneurons of different types naturally have

synapses that tend to some preferred size without intentional manipulation, perhaps influenced by their location with respect to the fine structures. A consensus list of all actually distinct types of interneurons in the hippocampus is not available and even the possibility of making one has been questioned.

However, conventions do exist. To coin a term (but see Hodge et al., (2018)), *supertypes* of interneurons would be inclusive groups that share one broad but distinct feature (such as: calcium binding protein, developmental origin, position of soma, directionality of inhibition, etc.). Though a supertype will contain multiple recognized subtypes, this organizing scheme would make it possible to construct a coarse but informative map of the distribution of dendrite types. As we become more oriented at this coarse level, using such an imprecise map will enable an increasingly sophisticated dendritic cartography. Mapping the forest before attempting to describe every unique tree can focus the great effort already being expended on grappling with the often-overwhelming complexity of interneuron subtypes. Once a consensus is reached at a simpler level, tools exist for mapping at taxonomically higher (so to speak) resolutions. Such tools exist and are constantly being improved—like genetically modified driver animals that restrict expression of some virally-delivered proteins to genetically or molecularly identified interneuron subtypes. As in war, taming the dendritic jungle will require a strategy of divide and conquer, not conquer first then divide.

The differential responses in size adjustment of synapses on the different regions to LTP induction in the slices makes any simplistic theory of synaptic plasticity rules based on their underlying fine structures unrealistic. Even though the fine structures may

be supporting similar tasks, the specific position of the parent neuron within the local network is likely to be the most important factor in determining how synaptic plasticity is expressed and in what direction it should change, i.e., potentiation or depression. For example, interneurons mediating feed-forward inhibition are not expected to respond the same way to stimuli as those mediating feed-back inhibition (Kullmann et al., 2011). We can imagine a scenario in which simultaneous LTP at glutamatergic synapses supplied by the same axon should obtain when driving feed-forward inhibition as this is important for preserving the temporal fidelity of coincidence detection at pyramidal cell dendrites. Conversely, an interneuron mediating feedback inhibition might need to depress to prevent clamping upstream elements. The situation becomes more complex when disinhibition in both feed-forward and feedback configurations are taken into consideration.

Systematic empirical study of the interplay between synaptic plasticity and the directionality of inhibition is called for, but such experiments remain very technically challenging. Detailed simulations will be of aid here, especially molecular dynamic simulations at scale, which are becoming possible with the increasing computational power available. However, without precise details on nanoscale connectivity, such simulations will be incomplete, perhaps hopelessly so, but every constraint supplied by empirical observations will improve confidence in their utility.

Potentiation in slice significantly changed the distribution of mitochondria in the fine structures. Mitochondria were much more common in inter-varicose sections after TBS compared to controls and became less common in smooth sections. In varicose

sections, mitochondria prevalence increased where the synapses increased in area and decreased where the synapses did not significantly change. While the decrease in varicose region synapses in slice 2 did not reach statistical significance, the trend was toward smaller synapses.

Glycogen particles in aspiny dendrites were massively enriched compared to nearby spiny dendrites. This was unexpected, but in retrospect perhaps not surprising. Given the many studies of the energy demands of highly active interneurons and the findings linking fast network oscillations to available energy reserves, our observation of high glycogen concentration comports well with such results. We saw before that neurons, unlike astrocytes, do not accumulate glycogen when provided with media with high glucose concentration, and we showed that glycogen availability per synapse did not significantly change by condition except in smooth regions in slice 2. Further interrogation of glycogen availability at synapses awaits larger datasets covering more time points.

Our findings of structural synaptic plasticity on aspiny interneuron dendrites raises several questions as well as providing some context that may aid the interpretation of earlier findings of functional long-term plasticity in the hippocampal interneurons. The possibility that inherent fine structures in aspiny dendrites play a role in the induction or maintenance of plasticity is intriguing. Our data showed that inter-varicose region synapses enlarged in response to theta burst in both slices and their portion of mitochondria per section also increased. It must be kept in mind that the varicose and inter-varicose synapses are on the same dendritic segments, which raises the possibility

that varicose and inter-varicose regions might allow synapses to make independent plastic responses to the same stimulation even over distances as short as 1-2 μm, the average length of those regions. Larger datasets and greater insight into the network position of these dendrites is needed to address this question.

The different responses by synapses on the smooth dendritic regions between the slices might be explained in part by the molecular identity of their parent somata as well as their role in the type of inhibition being provided. It is currently unknown which could, or should, have a stronger impact on how synapses respond to a stimulus. Much work remains to investigate the prevalence of the different dendritic types in different interneuron subtypes. A detailed atlas of the ultrastructure and distribution of the interneuron subtypes is needed across all axes of the hippocampus.

Several studies (Freund et al., 1996; Gulyá et al., 1999; Scheuss et al., 2014) have found that many types of interneurons show both varicose and smooth dendrites—often remarking that proximal dendrites are smooth and become varicose, though it is unknown if a smooth dendrite far from the soma can have varicose regions or the converse. In our data we did not see any transitions from varicose to smooth, though the longest of our segments was ~11μm long.

ENERGETICS

In chapters 5 and 6 we presented our findings on mitochondrial distribution and glycogen prevalence in aspiny dendrites. Though all neurons have high energy requirements compared to other tissue, the amount of power demanded by interneurons

places them in a unique position. It is not controversial that fast-spiking interneurons consume energy disproportionate to their size (Kann et al., 2014; Sohal et al., 2009). It is also believed that information processing and routing through the hippocampus depends in large part on high frequency oscillations like the gamma rhythm, that depends to a large extent on the activity of PV-expressing interneurons (Galow et al., 2014; Tamura et al., 2006). Although only the CR-expressing interneuron-specific interneurons completely avoid contributing inhibitory synapses to pyramidal cells, most interneuron types send at least a few direct inputs to most other interneuron types (Bezaire et al., 2013). Several neurological disorders can be characterized by detectible disruptions to normal rhythmic activity. The most well-known disorder associated with extreme and inappropriate synchronization is epilepsy (Löscher, 2017). Rhythm abnormalities have been found in schizophrenia (Bassett et al., 2010; Dvey-Aharon et al., 2015; Williamson, 2007), Alzheimer's (Haan et al., 2009), acute and persistent psychosis (Gong et al., 2017; Samudra et al., 2015), and recently specific increases in pallidal and thalamic theta-rhythm spectral power and prolonged theta burst activity have been found to correlate with muscle tics in Tourette syndrome (Neumann et al., 2018).

We have remarked on the ability of specific interneurons to modify local blood flow, and the importance of learning to read how this activity affects hemodynamics and the spatial extent of this influence for the interpretation of non-invasive neuroimaging. The information given here on the distribution of glycogen could prove useful when considering the time course of energy demand if accurate models can be constructed regarding the magnitude and variability of available fuel reserves of different types of

interneurons, especially with respect to their activation history and network position. We have already seen that slices maintained *in vitro* are capable of supporting gamma oscillations for up to 8 minutes in the absence of glucose while their glycogen metabolizing enzymes are inhibited (Galow et al., 2014). Extending these observations from whole slices to individual interneurons or interneuron types will be of great utility.

Although the relationship between structure and function in biological entities often appears obvious, this is certainly not always the case. The dictum that form follows function can provide guidance in cases where both or either form and function are too complex to grasp in any straightforward way. Evolution is under no obligation to always find the absolute optimal solution to some problem. Finding some local minimum, using an analogy with gradient descent, that is "good enough", will be maintained by selection pressure and invoking simple adaptationism on the complexity of interneuron forms is clearly insufficient (Gould & Lewontin, 1979). Including some physical constraints, as suggested by Gould and Lewontin, can prevent theoretical models from becoming completely uncoupled with the underlying physical phenomenon and increase predicative or explanatory power. Since our knowledge of the specific computational processes supported by the aspiny dendrites is incomplete, to say nothing of the processes supported by entire classes of interneurons, constraints imposed by energy requirements have proven useful in the effort to develop theories of neural information processing (Moore et al., 2008) and might be fruitfully applied here. Our data on the regularity of fine structures, mitochondrial distribution, and glycogen availability are fundamental

physical processes that are reasonable to assume to be common among interneurons and may provide some additional empirical constraints to aid in constructing theories.

INTERNEURON COMPUTATIONS IN THE CONTEXT OF FINE STRUCTURE

Dendritic computation is a much-studied topic in principal cells (Abbott & Regehr, 2004; Bloss et al., 2018; Denk et al., 2012; Polsky et al., 2004; Silver, 2010a). There is, however, little that is universally agreed upon. At the grossest and probably least controversial level are abstractions like associativity, pattern completion, pattern separation, memory, generalization, and reasoning (Bromer et al., 2018; Marr, 1970, 1971; van Hemmen & Sejnowski, 2009). Getting deeper into the fine structures there are some features that can be linked to such abstract level operations (Govindarajan et al., 2006; Makara et al., 2009; Schmidt-Hieber et al., 2007; Silver, 2010b), such as flexible dendritic integration, coincidence detecting receptors, and synaptic plasticity (Bloss et al., 2016).

Despite progress on neural computation in general, there is little agreement on the computational roles of specific fine structures; even the dendritic spine, a highly conserved and common structure used by numerous types of neurons across species separated by enormous evolutionary distances, merits little agreement on its fundamental role in information processing. Theories of spine function have ranged from physical (increasing surface area or extending reach to more axons), to chemical (sequestering or concentrating resources), to (arguably) computational (altering integration dynamics by

changing membrane properties) (Bokota et al., 2016; Gulledge et al., 2012; Koch & Zador, 1993; Mancuso et al., 2014).

Even less is known about what sorts of computation an aspiny dendrite can perform that a spiny dendrite cannot, or further, what a dendritic varicosity can do that a smooth or an inter-varicose region cannot. Perhaps the fine structural modules of varicosities separated by the constricted inter-varicose region form independent subunits that interneurons with different molecular profiles, excitability properties, and inhibitory configurations within the local network can use in characteristic ways to support whatever it is they are specialized at doing. The bewildering array of forms and functions could not remain so well conserved were they not efficiently solving a problem that could not be solved in any other way. What those specific problems may be are sufficiently complex to be opaque to us now. Such spatiotemporal complexity of form suggests a massive repertoire of contingent responses, that is, access to an enormous space of possible computations that we are working to understand. Theories of biological neural network computation are so difficult to make explicit because our knowledge of the detailed processes and structures involved is limited.

Recognizing that inhibition is important to prevent runaway excitation, or the role that lateral and surround inhibition play in sharpening location discrimination in primary senses is an achievement (Yu et al., 2014); and the advances and utility in machine learning based off insights from the brain are beyond question, even if we do not know all the details about why they work. One path to understanding something is to break part of it and observe the results. Only very recently has technology become available to

allow perturbation of identified inhibitory neurons and thereby gain some information about their function.

Two recent studies focusing on identified interneuron types will illustrate the possibilities. In a study on the functional effects of different types of CA1 interneurons, either dendrite-targeting SST-expressing interneurons or soma-targeting PV-expressing interneurons were deactivated via selective expression of halorhodopsin, a light-gated chloride pump, and the focused delivery of light to animals expressing the protein in one cell type or the other. Recordings of place cells (PlCs) from head-fixed animals running on an enriched treadmill demonstrated that the two types of inhibition had quite different effects on the output of the PlCs. Intriguingly, deactivation of neither SST or PV-expressing interneurons had any effect on the size or location of the recorded place cell's receptive field. Instead, suppression of dendritic inhibition greatly increased burst-firing (45% increase in spike doublets and 280% increase for >5 spike bursts) of the place cell without altering the normal phase-locking of PlC spikes with the hippocampal theta oscillation, while suppression of somatic inhibition resulted in a relatively small increase in firing (30% increase in doublets) but a significant (but not complete) desynchronization of spike generation from theta (Royer et al., 2012).

Second, and perhaps more suggestive about how neurons use time for computation, Basu et al. (2016) used similar targeted optogenetic and pharmacogenetic techniques to first identify a specific long-range inhibitory pathway from the lateral entorhinal cortex (LEC). Selective activation of this pathway results in large IPSCs located in a subclass of SR-SLM border-dwelling CCK interneuron (CCK SR-SLM), the

target of the long-range inhibitory path from LEC. LEC, opposed to MEC, delivers multi-modal non-spatial information to hippocampus (no grid cells). These CCK SR-SLM interneurons also receive strong excitatory drive from Schaffer collateral axons to its dendrites in SR and in turn provides inhibitory synapses to CA1 pyramidal cell dendrites, consistent with a role in feed-forward inhibition. Entorhinal cortex (EC) supplies the major cortical input to the hippocampus through the perforant path (PP), with the largest inputs (indirect path) arriving in the dentate molecular layer, the first step of the tri-synaptic loop. Some of the EC PP fibers diverge and carry information directly (direct path) to the distal apical dendrites of CA1 pyramidal cells in the SLM. This results in an interesting temporal delay and an opportunity for CA1 cells to compare the same information from the EC—received first directly at the distal dendrites, then indirectly after processing performed by dentate and CA3. Such processing likely consists of some sort or sorts of transformation and the addition of information (hippocampus receives information from sources other than EC, most prominent is from septum which synapses in dentate, second is supramammillary and other hypothalamic inputs also mostly to dentate, and a direct and specific input from supramammillary to CA2 (Bliss, 2007)). These upstream areas send the processed data to CA1 via the Schaffer axons, which arrive at the spatially closer and physically larger proximal apical dendrites, ~25ms after direct EC input (Yeckel & Berger, 1990).

Basu et al. (2016) showed that by blocking EC inhibitory drive onto the CCK SR-SLM interneurons, i.e., disinhibition of the CCK inhibition, or increased inhibitory drive from CCK to CA1 dendrites prevented supralinear summation of excitatory potentials

from direct EC input and indirect CA3 SC inputs that arrive ~20ms later. Further, slice experiments with paired EC-SC stimulation led to potentiation of EPSPs in CA1 neurons when EC stimulation preceded SC stimulation by 20ms if LEC long-range inhibitory inputs to CCK SL-SLM interneurons was not occluded, effectively demonstrating conditionally dynamic activation functions. Pharmacological inactivation of LEC output inhibition *in vivo* led to inappropriate generalization of contextual fear conditioning, and deficits in novel object recognition, though memory acquisition was not prevented. Experiments like these producing more data and informing more sophisticated methods of analyzing synchronization at higher resolutions (Colgin, 2016; Roux & Buzsáki, 2015) provide a basis to begin distinguishing which questions are relevant for understanding neural computations.

Building the map of interneuron ultrastructure in CA1 is a major challenge and tools to construct it are only now becoming available (Aghili & Fang, 2018; Deng et al., 2018; Harris et al., 2018; Le Roux et al., 2015; Royer et al., 2012; Tricoire et al., 2011; Wang et al., 2018). Pharmacogenetic and optogenetic techniques will allow the increasingly specific perturbation of defined interneuron types (Basu et al., 2016; Royer et al., 2012). Massive single cell transcriptomics and proteomics (Harris et al., 2018; Tasic, 2018) and improvements in machine learning that are being turned on the massive amounts of molecular information (Ding et al., 2018; Johnstone & Fetit, 2018; Tasic, 2018) can help find relationships that might be too obscure or complex for humans to find.

FUTURE DIRECTIONS

Volume EM reconstructions are not the only way to go about building the connectome of interneurons of the hippocampus. Super resolution microscopy techniques like such as stochastic optical reconstruction microscopy (STORM) and photoactivated localization microscopy (PALM) can currently achieve x-y resolution of ~10nm and z-resolution of twice that (Hauser et al., 2017). Combined with multiple fluorescent tags, such methods could be sufficient for wiring diagrams and quantifying the distribution of dendrite fine structures in identified interneurons. We know of no systematic studies using such techniques to study the distribution of fine structures in aspiny interneuron dendrites and the resolution is insufficient for detailed analysis of changes in synapse size and many relevant structures are too small to resolve. 3DEM remains the best but slowest and most labor-intensive method to achieve adequate resolution for the detailed study of fine structure and subcellular resource distribution. For realistic biophysical simulations of neural compartments, only models derived from EM resolution data will be sufficiently constrained by empirical measurements.

The extreme spatial specificity with which interneurons of different types send axons to characteristic domains of pyramidal cell dendrites is being explored (Bloss et al., 2016). The complimentary specificity with which excitatory axons discriminate domains or fine structures of interneuron dendrites must be explored as well, and this will comprise part of the task of creating a complete description of the connectivity of interneuron subtypes in the CA1 region of the rat hippocampus. The complete connectome of the interneurons of the rat hippocampus is achievable with currently

available technology, though without further developments in sample preparation and acquisition speed, achievable merely means possible in a finite amount of time, however many years (decades) that may be.

The desirability of such a structural map cannot be overstated, but in the absence of detailed information about the structural responses of synapses onto the interneurons, that is, more systematic understanding of synaptic plasticity with respect to subtype, network position, and fine structure distribution, this map would be incomplete. By combining existing methods, some awaiting publication, this structural map can be extended to yield rules about synaptic plasticity, of which the present dissertation merely scratches the surface.

The magnitude of such an undertaking should not be underestimated. Before describing the future, it is valuable to understand the past. The first complete reconstruction of an animal nervous system, that of the nematode *Caenorhabditis elegans,* consisted of 8000 serial EM sections completely describing all ~300 neurons and the total set of connections between them. This herculean task of manual reconstruction took 15 years to complete (White et al., 1986).

More recently, connectomic data comprising the entire central nervous system (CNS) from a 6-hour old female fruit fly larva has become available (Ohyama et al., 2015). The CNS reconstruction was obtained from 4840 serial sections at ~50nm thickness imaged on a TEM at ~4nm per pixel. Reconstructions were partially automated using a modified version of CATMAID (Saalfeld et al., 2009) software (http://www.catmaid.org). Automating 3DEM reconstruction is an important step but

currently cannot match the accuracy of human experts. This work is notable in that the number of neurons reconstructed in the larval fly was ~10,000.

Another entire central nervous system, from the ascidian tadpole larva, *Ciona intestinalis,* was reconstructed via serial section electron microscopy (Ryan et al., 2016) from 6928 sections ranging from 60-100nm in thickness and imaged on a TEM at ~4nm per pixel. Images were imported into Reconstruct (Fiala, 2005) in either high or low magnification series. Low magnification series had neuronal processes skeletonized using the Z-Trace tool. Processes not exhibiting synapses or seen leaving the CNS were not included. In the high magnification series, structures deemed to contribute to the CNS connectome were then manually traced. *Ciona intestinalis* is a sea squirt. As a member of the subphylum *Tunicata*, it is the first chordate to have its full CNS connectome reconstructed, which was found to consist of 177 central neurons that form 6618 synapses.

A single hemisphere of a rat hippocampal area CA1 is estimated to contain ~38,500 interneurons (Bezaire et al., 2013). Constructing a complete interneuron connectome including plasticity descriptions can be accomplished with extant technology and significant effort. One possible avenue to achieve this would combine array tomography—a technique that allows for correlative super resolution fluorescent microscopy and electron microscopy (Hauser et al., 2017; Micheva & Smith, 2007; Watanabe et al., 2014)—with an optogenetic method for plasticity induction currently in development (unpublished data). The opto-LTP (long-term plasticity) method uses adeno-associated virus injections to deliver the optical effector and a second protein

allowing the identification of infected, hence light-sensitive, axons in EM images. Using viral injections to deliver channelrhodopsin and a genetically encoded ascorbate peroxidase to cell bodies in CA3, the subset axons expressing the construct can be stimulated with light to induce LTP and subsequently labeled with gold-conjugated antibodies for EM identification (data not published). This would allow the identification of defined interneuron subtypes along with information on the activity of specific synapses. Using super resolution correlative fluorescent microscopy with EM could allow us to dispense with the peroxidase if resolution is sufficient to discriminate fluorescent axons.

Array tomography allows for the fluorescent tagging of multiple proteins with immunofluorescence or using tissue from animals engineered to express fluorescent markers in specific neuron subtypes. An acrylic resin is used as embedding media rather than epoxy (Micheva et al., 2007). The same tissue can be imaged multiple times using specific markers to distinguish different structures in the final combined section which can be pseudo-colored for identifying which marker is expressed in which structure. A desirable technical challenge to solve to increase throughput is the development of a technique that makes this possible with tSEM. Array tomography uses glass to hold the sections, so transmission imaging is not possible. Adapting the technique to allow transmission mode in a scanning EM will allow acquisition of far larger fields and decrease the time needed for imaging. Another desirable feature of using tSEM is the possibility of performing electron (EM) tomography (not the same thing as array tomography) on the ultrathin sections.

EM tomography (Subramaniam & Zhang, 2003) is akin to the CT (computed tomography) scan frequently used in medicine (Brooks & Chiro, 1976; Ledley et al., 1974). Tomography—from the Ancient Greek *tomos,* "slice, or section" and *grapho,* "to write"—generally refers to imaging by section using any kind of penetrating wave. For our purposes the penetrating wave is the electron beam. EM tomography involves imaging a sample multiple times at different angles by tilting the specimen during acquisition. Tilting exposes internal structures in different parts of the sample to the focal plane of the beam. After several rounds of imaging, some method, i.e., advanced modern computer-assisted mathematical inference (van Aarle et al., 2015) or purely optical techniques that have long been in use (Oldendorf, 1961), is applied to project or reconstruct information from within the sample (Gilbert, 1972).

There are two immediate and obvious benefits that EM tomography methods provide. First, it allows for the cutting of thicker sections which will reduce both the total number of sections needed as well reduce the probable loss of sections during collection as thicker sections are more durable. Second, tomography generates virtual slices of the imaged specimen obtained from within the sample. Serial ultrathin sections cannot physically be cut thinner than ~30nm. While serial block (SB) face methods are restricted to scanning EM (SEM) only, techniques like diamond-knife SBEM can remove ~20nm of sample surface between images and ablation with a focused beam of metal ions (FIB) has achieved a depth resolution of ~2nm (Denk et al., 2012; Xu et al., 2017), they require difficult en-block staining, image fields are limited to at most a few tens of microns by the ion beam (Kornfeld & Denk, 2018), and they destroy the sample. In TEM or tSEM

imaging, the electron beam passes through the ultrathin sample, projecting and smearing any objects smaller than the section thickness together at the detector. An x-y resolution of 4nm is common and 2nm is often achieved, yet the z resolution is typically $1/20^{th}$ of that. There are many structures of interest with processes that are significantly smaller than 30nm, e.g., thin axonal processes may be obscured by overlying structures and lost (Bourne et al., 2013), and tubules of smooth endoplasmic reticulum can be difficult to connect between sections as they can move laterally for some distance through the thickness of an ultrathin section (Chirillo et al., 2015; Cui-Wang et al., 2012).

Tomographic virtual sections can achieve z resolution of ~5nm or less (Harris et al., 2015; Zhu et al., 2006). Virtual sections confer another benefit beyond simply affording better z resolution. The uncertainty of object position that occurs when the imaging beam passes through the sample and collapses ~30nm worth of information into a single image is the main challenge faced by machine vision algorithms used for auto-segmentation (Januszewski et al., 2018; Kornfeld et al., 2018). Following the purely manual methods used by White et al, (1986) or restricting ourselves to FIB-SBEM for its resolution, acquiring comparatively large volumes like a whole mouse brain, or even a mouse hippocampus would take thousands of years without enhancements to acquisition and reconstruction (Kornfeld et al., 2018). It has been estimated that computer-aided manual dense reconstruction (dense means full reconstruction of every visible structure in the available volume) with the methods used in this dissertation if applied to a single human brain (~1500cm^3 or 1.5 quadrillion μm^3) would take 8 trillion years (Harris, 2014).

The idea of synaptic scale reconstruction of a single hemisphere of rat hippocampal area CA1 with its ~350,000 neurons (Bezaire et al., 2013) is no longer the impossible dream that it was as little as a decade ago. 30 years passed between the publication of the complete EM reconstruction of *Caenorhabditis elegans* nervous system by White et al. (1986) and that of *Ciona intestinalis* by Ryan et al. (2016). Less than two years later a complete electron microscopy volume of the brain of an adult fruit fly, *Drosophila melanogaster*, was published (Zheng et al., 2018). 7050 serial sections at ~40nm thickness consisting ~100,000 neurons in a volume of ~80 million μm^3 were cut, imaged on a TEM at 4nm per pixel, and analyzed over the course of 18 months. The analysis and reconstructions are not yet complete, the data is openly available and interested parties may contribute at http://www.temca2data.org/. Zheng et al. (2018) developed methods for automated specimen loading into the EM allowing 24/7 imaging of the ~2400 uniquely identifiable grids that held the 7050 serial sections. In chapter 2 we examined the limited field size that can be acquired by TEM, ~8x8µm, and to circumvent this we used the tSEM method which gave us larger field sizes of ~50x50µm, a necessity for finding the rare aspiny interneuron dendrites in unlabeled tissue. The limited field size was addressed by Zheng (2018) by employing an improved version of a high-speed TEM camera (TEMCA) that allows the simultaneous parallel acquisition of multiple small TEM fields on the same physical section (Bock et al., 2011). In conjunction with custom apparatus for rapid and precise movement of the stage allowed acquisition of a whole brain section of ~750µm by ~350µm, or ~260,000μm^2 in 7 minutes at 4nm per pixel.

As we wish much larger reconstructions with known synaptic activity history, we must begin with the acute slice rather than an entire hippocampal hemisphere. Our dorsal slices have approximate dimensions of ~3mm from the edge of CA3 to the subiculum along the proximo-distal axis, ~2.5mm from the top of CA1 stratum oriens to the bottom of the exposed blade of the dentate and are ~400µm thick. This translates to a volume of ~2 billion μm^3. The CA1 alone spans ~2mm proximo-distal and ~1.25mm from oriens to the hippocampal fissure, or ~1 billion μm^3. Preparing such a large block of tissue for ssEM is not standard, but there are methods available for dividing embedded blocks of this size into smaller pieces without significant tissue loss, such as the hot diamond knife (Hayworth et al., 2015). Cutting the ~2mm wide CA1 into 4 sections would yield rectangular blocks ~500 µm wide and ~400 µm thick, within the range of section sizes obtained by Zheng et al. (2018) for the adult fly brain. The resulting strips spanning SLM to SO would be ~1250 µm long and if cut at ~40nm would require 31,250 serial sections each, totaling ~125,000 sections. Even though Zheng et al. (2018) lost only 12 sections out of 7062 (99.8% success), the move from ~7000 to ~125,000 sections is not trivial.

Tomography can ameliorate this serious technical challenge by allowing thicker sections. 300nm is a common sample thickness in STEM tomography, which would reduce the needed sections to ~16,666; 300nm sections can routinely produce virtual sections with axial resolution well below 10nm, and 1µm thick heavy-metal stained plastic embedded sections can produce good quality virtual section resolutions around 20-30nm (Noske et al., 2008; Soto et al., 1994; Sousa et al., 2011). At 1µm thick, only ~5000 total sections would need to be cut.

An encouraging development was the publication of whole-brain ssEM volumes at synaptic resolution from the zebra fish larva, obtained from two sets of images at ~60nm thickness each comprising more than 17,000 sections (Hildebrand et al., 2017).

The area of single tSEM field can easily contain 60 TEM fields at the same pixel size of 2nm, reaching ~4,300μm^2. To equal the area acquired by TEMCA would require ~60 individual tSEM images, but by using montaging the operator time need not increase linearly with the number of images (Kuwajima et al., 2013). Imaging like this, especially if tomography is used, the acquisition time would be several days for ~200 physical sections of comparable size to those of the adult fly brain. tSEM is amenable to parallelization using camera arrays as it uses transmission imaging, so one possible path to drastic improvements in acquisition time are possible. There is no reason in principle that parallelization of acquisition is not compatible with tomographic methods, but modifications to the stage and sensor would be likely. tSEM is also quite suitable for tomography due to the low accelerating voltages, tomography is effective at low electron doses (Kuwajima, 2014; Nickell et al., 2005), but remains effective at higher voltage as the specimen thickness increases. Tomography is not the only method to acquire virtual sections with increased axial resolution. Techniques that do not require sample tilting or only require one rotation of the sample do exist, such as multi-energy deconvolution EM (De Goede et al., 2017). Tomography is, however, the most successful and widely used method for virtual sectioning with numerous software packages available for image reconstruction (Fung et al., 1996; Koster et al., 1992; Messaoudii et al., 2007; Nakazawa et al., 2006.; Phan & Lawrence, 2008; Zheng et al., 2004; Shawn Q. Zheng et al., 2007).

One of the many virtues of the tSEM method is the ability to collect backscattered electrons in addition to the transmitted electrons. With scanning detectors capable of registering electrons with different energy levels, sample interiors can be probed with minimal rotations. In addition, gains in acquisition speed can be realized by combining magnetic beam rasterization and physical translation of the sample by precise movements of the stage.

These methods will not be fast or easy, but previous work suggests that it is possible. The move from a fruit fly brain to even a single hemisphere hippocampal area CA1 from adult rat will be a great challenge, but such an undertaking now seems inevitable. As the great philosopher Spinoza said, “All things excellent are as difficult as they are rare” (Spinoza, 1677).

Our data provide the first information on the ultrastructural plasticity of synapses on aspiny interneuron dendrites as well as the furthest timepoint in the study of interneuron synaptic plasticity available. Since we did not use patch clamp methods, cellular integrity was maintained for the duration of the two-hour recording period.

These data reveal only a small part of a much larger and more complex picture. The study of structural plasticity on aspiny interneuron dendrites affords a glimpse into the computational processes the interneurons support, both as whole cells and the sub-computations being performed within dendritic segments. Any future analysis of interneuron function must take dendrite fine structures into account. Failure to do so would be analogous to studying pyramidal cell dendrites in the absence of knowledge of the existence of dendritic spines. In a very literal sense one can say that the structure of a

neuron *is identical* to its function. It is only through the detailed, painstaking, and thorough exploration of structure that we will come to understand function.

References

Abbe, E. (1873). Ueber einen neuen Beleuchtungsapparat am Mikroskop. *Archiv Für Mikroskopische Anatomie*, *9*(1), 469–480. https://doi.org/10.1007/BF02956177

Abbott, L. F., & Regehr, W. G. (2004). Synaptic computation. *Nature*, *431*(7010), 796–803. https://doi.org/10.1038/nature03010

Aghili, M., & Fang, R. (2018). Mining Big Neuron Morphological Data. *Computational Intelligence and Neuroscience*, *2018*(2), 1–13. https://doi.org/10.1155/2018/8234734

Armstrong, C., Krook-Magnuson, E., & Soltesz, I. (2012). Neurogliaform and Ivy Cells: A Major Family of nNOS Expressing GABAergic Neurons. *Frontiers in Neural Circuits*, *6*(May), 23. https://doi.org/10.3389/fncir.2012.00023

Bartol, T. M., Bromer, C., Kinney, J., Chirillo, M. A., Bourne, J. N., Harris, K. M., & Sejnowski, T. J. (2015). Nanoconnectomic upper bound on the variability of synaptic plasticity. *ELife*, *4*(NOVEMBER2015). https://doi.org/10.7554/eLife.10778

Bassett, D. S., Bullmore, E., Verchinski, B. a, Mattay, V. S., Weinberger, D. R., & Meyer-lindenberg, A. (2010). Hierarchical organization of human cortical networks in health and schizophrenia, *28*(37), 9239–9248. https://doi.org/10.1523/JNEUROSCI.1929-08.2008.Hierarchical

Basu, J., Zaremba, J. D., Cheung, S. K., Hitti, F. L., Zemelman, B. V., Losonczy, A., & Siegelbaum, S. A. (2016). Gating of hippocampal activity, plasticity, and memory by entorhinal cortex long-range inhibition. *Science*, *351*(6269).

https://doi.org/10.1126/science.aaa5694

Bell, M. E., Bourne, J. N., Chirillo, M. A., Mendenhall, J. M., Kuwajima, M., & Harris, K. M. (2014). Dynamics of nascent and active zone ultrastructure as synapses enlarge during long-term potentiation in mature hippocampus. *Journal of Comparative Neurology*, *522*(17), 3861–3884. https://doi.org/10.1002/cne.23646

Bezaire, M. J., & Soltesz, I. (2013). Quantitative assessment of CA1 local circuits: Knowledge base for interneuron-pyramidal cell connectivity. *Hippocampus*, *23*(9), 751–785. https://doi.org/10.1002/hipo.22141

Bliss, T. (2007). The hippocampus book. (P. Andersen, R. Morris, D. Amaral, & J. O'Keefe, Eds.), *The Hippocampus Book.* New York, NY, US: Oxford University Press.

Bloss, E. B., Cembrowski, M. S., Karsh, B., Colonell, J., Fetter, R. D., & Spruston, N. (2016). Structured Dendritic Inhibition Supports Branch-Selective Integration in CA1 Pyramidal Cells. *Neuron*, *89*(5), 1016–1030. https://doi.org/10.1016/j.neuron.2016.01.029

Bock, D. D., Lee, W. C. A., Kerlin, A. M., Andermann, M. L., Hood, G., Wetzel, A. W., … Reid, R. C. (2011). Network anatomy and in vivo physiology of visual cortical neurons. *Nature*, *471*(7337), 177–184. https://doi.org/10.1038/nature09802

Bokota, G., Magnowska, M., Kuśmierczyk, T., Łukasik, M., Roszkowska, M., & Plewczynski, D. (2016). Computational Approach to Dendritic Spine Taxonomy and Shape Transition Analysis. *Frontiers in Computational Neuroscience*, *10*(December), 1–11. https://doi.org/10.3389/fncom.2016.00140

Bourne, J., & Harris, K. M. (2007). Do thin spines learn to be mushroom spines that remember? *Current Opinion in Neurobiology*, *17*(3), 381–386. https://doi.org/10.1016/j.conb.2007.04.009

Bourne, J. N., Chirillo, M. A., & Harris, K. M. (2013). Presynaptic ultrastructural plasticity along CA3???CA1 axons during long-term potentiation in mature hippocampus. *Journal of Comparative Neurology*, *521*(17), 3898–3912. https://doi.org/10.1002/cne.23384

Bourne, J. N., & Harris, K. M. (2011a). Coordination of size and number of excitatory and inhibitory synapses results in a balanced structural plasticity along mature hippocampal CA1 dendrites during LTP. *Hippocampus*, *21*(4), 354–373. https://doi.org/10.1002/hipo.20768

Bourne, J. N., & Harris, K. M. (2011b). Coordination of size and number of excitatory and inhibitory synapses results in a balanced structural plasticity along mature hippocampal CA1 dendrites during LTP. *Hippocampus*, *21*(4), 354–373. https://doi.org/10.1002/hipo.20768

Bourne, J. N., & Harris, K. M. (2012). Nanoscale analysis of structural synaptic plasticity. *Current Opinion in Neurobiology*, *22*(3), 372–382. https://doi.org/10.1016/j.conb.2011.10.019

Bowden, J. B., Abraham, W. C., & Harris, K. M. (2012). Differential effects of strain, circadian cycle, and stimulation pattern on LTP and concurrent LTD in the dentate gyrus of freely moving rats. *Hippocampus*, *22*(6), 1363–1370. https://doi.org/10.1002/hipo.20972

Brandt, M. D., Jessberger, S., Steiner, B., Kronenberg, G., Reuter, K., Bick-Sander, A., … Kempermann, G. (2003). Transient calretinin expression defines early postmitotic step of neuronal differentiation in adult hippocampal neurogenesis of mice. *Molecular and Cellular Neuroscience*, *24*(3), 603–613. https://doi.org/10.1016/S1044-7431(03)00207-0

Brocard, J. B., Tassetto, M., & Reynolds, I. J. (2001). Quantitative evaluation of mitochondrial calcium content in rat cortical neurones following a glutamate stimulus. *J Physiol*, *531*(Pt 3), 793–805. https://doi.org/10.1111/j.1469-7793.2001.0793h.x

Broglie, L. De, & Broglie, L. De. (1924). Recherches sur la théorie des Quanta.

Bromer, C., Bartol, T. M., Bowden, J. B., Hubbard, D. D., Hanka, D. C., Gonzalez, P. V., … Harris, K. M. (2018). Long-term potentiation expands information content of hippocampal dentate gyrus synapses. *Proceedings of the National Academy of Sciences*, *115*(10), E2410–E2418. https://doi.org/10.1073/pnas.1716189115

Brooks, R. A., & Chiro, D. G. (1976). Principles of computer assisted tomography (CAT) in radiographic and radioisotopic imaging. *Physics in Medicine and Biology*, *21*(5), 689–732. https://doi.org/10.1088/0031-9155/21/5/001

Bukalo, O., Campanac, E., Hoffman, D. A., & Fields, R. D. (2013). Synaptic plasticity by antidromic firing during hippocampal network oscillations. *Proceedings of the National Academy of Sciences*, *110*(13), 5175–5180. https://doi.org/10.1073/pnas.1210735110

Buzsáki, G., & Eidelberg, E. (1982). Direct afferent excitation and long-term potentiation

of hippocampal interneurons. *Journal of Neurophysiology*, *48*(3), 597–607. https://doi.org/10.1152/jn.1982.48.3.597

Buzsáki, G., Kaila, K., & Raichle, M. (2007). Inhibition and Brain Work. *Neuron*, *56*(5), 771–783. https://doi.org/10.1016/j.neuron.2007.11.008

Buzsáki, G., & Mizuseki, K. (2014). The log-dynamic brain: How skewed distributions affect network operations. *Nature Reviews Neuroscience*, *15*(4), 264–278. https://doi.org/10.1038/nrn3687

Buzsáki, G., & Wang, X.-J. (2012). Mechanisms of Gamma Oscillations. *Annual Review of Neuroscience*, (March), 203–225. https://doi.org/10.1146/annurev-neuro-062111-150444

Carlson, G. M., Dienel, G. A., & Colbran, R. J. (2018). Novel insights into brain glycogen metabolism. *Journal of Biological Chemistry*, *293*, jbc.TM118.002642. https://doi.org/10.1074/jbc.TM118.002642

Cates, M. S., Teodora, M. L., & Phillips, G. N. (2002). Molecular mechanisms of calcium and magnesium binding to parvalbumin. *Biophysical Journal*, *82*(3), 1133–1146. https://doi.org/10.1016/S0006-3495(02)75472-6

Cembrowski, M. S., Bachman, J. L., Wang, L., Sugino, K., Shields, B. C., & Spruston, N. (2016). Spatial Gene-Expression Gradients Underlie Prominent Heterogeneity of CA1 Pyramidal Neurons. *Neuron*, *89*(2), 351–368. https://doi.org/10.1016/j.neuron.2015.12.013

Chamberland, S., & Topolnik, L. (2012). Inhibitory control of hippocampal inhibitory neurons. *Frontiers in Neuroscience*, *6*(NOV), 1–13.

https://doi.org/10.3389/fnins.2012.00165

Chirillo, M., Bourne, J., Lindsey, L., & Harris, K. (2015). Complexity of dendritic SER increases at enlarging synapses during LTP. *BioRxiv*, 015974. https://doi.org/10.1101/015974

Colgin, L. L. (2016). Rhythms of the hippocampal network. *Nature Reviews Neuroscience*, *17*(4), 239–249. https://doi.org/10.1038/nrn.2016.21

Colgin, L. L., Denninger, T., Fyhn, M., Hafting, T., Bonnevie, T., Jensen, O., … Moser, E. I. (2009). Frequency of gamma oscillations routes flow of information in the hippocampus. *Nature*, *462*(7271), 353–357. https://doi.org/10.1038/nature08573

Cowan, R. L., Wilson, C. J., Emson, P. C., & Heizmann, C. W. (1990). Parvalbumin-containing GABAergic interneurons in the rat neostriatum. *The Journal of Comparative Neurology*, *302*(2), 197–205. https://doi.org/10.1002/cne.903020202

Cui-Wang, T., Hanus, C., Cui, T., Helton, T., Bourne, J., Watson, D., … Ehlers, M. D. (2012). Local zones of endoplasmic reticulum complexity confine cargo in neuronal dendrites. *Cell*, *148*(1–2), 309–321. https://doi.org/10.1016/j.cell.2011.11.056

De Goede, M., Johlin, E., Sciacca, B., Boughorbel, F., & Garnett, E. C. (2017). 3D multi-energy deconvolution electron microscopy. *Nanoscale*, *9*(2), 684–689. https://doi.org/10.1039/c6nr07991a

Deco, G., Kringelbach, M. L., Jirsa, V. K., & Ritter, P. (2017). The dynamics of resting fluctuations in the brain: Metastability and its dynamical cortical core. *Scientific Reports*, *7*(1), 1–14. https://doi.org/10.1038/s41598-017-03073-5

Defelipe, J., López-Cruz, P. L., Benavides-Piccione, R., Bielza, C., Larrañaga, P.,

Anderson, S., … Ascoli, G. A. (2013). New insights into the classification and nomenclature of cortical GABAergic interneurons. *Nature Reviews Neuroscience*, *14*(3), 202–216. https://doi.org/10.1038/nrn3444

Del Río, M. R., & DeFelipe, J. (1997). Colocalization of parvalbumin and calbindin D-28k in neurons including chandelier cells of the human temporal neocortex. *Journal of Chemical Neuroanatomy*, *12*(3), 165–173. https://doi.org/10.1016/S0891-0618(96)00191-3

Deng, Y., Bao, F., Dai, Q., Wu, L., & Altschuler, S. (2018). Massive single-cell RNA-seq analysis and imputation via deep learning. *BioRxiv*, 315556. https://doi.org/10.1101/315556

Denk, W., Briggman, K. L., & Helmstaedter, M. (2012). Structural neurobiology: missing link to a mechanistic understanding of neural computation. *Nature Reviews. Neuroscience*, *13*(5), 351–358. https://doi.org/10.1038/nrn3169

Desai, M., Kahn, I., & Knoblich, U. (2011). Mapping brain networks in awake mice using combined optical neural control and fMRI. *J. Neurophysiol.*, *105*, 1393–1405. https://doi.org/10.1152/jn.00828.2010.

Ding, J., Condon, A., & Shah, S. P. (2018). Interpretable dimensionality reduction of single cell transcriptome data with deep generative models. *Nature Communications*, *9*(1), 2002. https://doi.org/10.1038/s41467-018-04368-5

Dvey-Aharon, Z., Fogelson, N., Peled, A., & Intrator, N. (2015). Schizophrenia detection and classification by advanced analysis of EEG recordings using a single electrode approach. *PLoS ONE*, *10*(4), 1–12. https://doi.org/10.1371/journal.pone.0123033

Fiala, J. C. (2005). Reconstruct: a free editor for serial section microscopy. *Journal of Microscopy*, *218*(Pt 1), 52–61. https://doi.org/10.1111/j.1365-2818.2005.01466.x

Fiala, J. C., Allwardt, B., & Harris, K. M. (2002). Dendritic spines do not split during hippocampal LTP or maturation. *Nature Neuroscience*, *5*(4), 297–298. https://doi.org/10.1038/nn830

Fiala, J. C., & Harris, K. M. (2001). Extending Unbiased Stereology of Brain Ultrastructure to Three-dimensional Volumes. *Journal of the American Medical Informatics Association*, *8*(1), 1–16. https://doi.org/10.1136/jamia.2001.0080001

Fiala, J. C., Kirov, S. a, Feinberg, M. D., Petrak, L. J., George, P., Goddard, C. A., & Harris, K. M. (2003). Timing of neuronal and glial ultrastructure disruption during brain slice preparation and recovery in vitro. *The Journal of Comparative Neurology*, *465*(1), 90–103. https://doi.org/10.1002/cne.10825

Fifková, E., & Anderson, C. L. (1981). Stimulation-induced changes in dimensions of stalks of dendritic spines in the dentate molecular layer. *Experimental Neurology*, *74*(2), 621–627. https://doi.org/10.1016/0014-4886(81)90197-7

Fifková, E., & Van Harreveld, A. (1977). Long-lasting morphological changes in dendritic spines of dentate granular cells following stimulation of the entorhinal area. *Journal of Neurocytology*, *6*(2), 211–230. https://doi.org/10.1007/BF01261506

Finsen, B. R., Tønder, N., Augood, S., & Zimmer, J. (1992). Somatostatin and neuropeptide Y in organotypic slice cultures of the rat hippocampus: An immunocytochemical and in situ hybridization study. *Neuroscience*, *47*(1), 105–113. https://doi.org/10.1016/0306-4522(92)90125-L

Freund, T. F., & Buzsáki, G. (1996). Interneurons of the hippocampus. *Hippocampus*, *6*(4), 347–470. https://doi.org/10.1002/(SICI)1098-1063(1996)6:4<347::AID-HIPO1>3.0.CO;2-I

Freund, T. F., & Buzsáki, G. (1998). Interneurons of the hippocampus. *Hippocampus*, *6*(4), 347–470. https://doi.org/10.1002/(SICI)1098-1063(1996)6:4<347::AID-HIPO1>3.0.CO;2-I

Freund, T. F., & Katona, I. (2007a). Perisomatic Inhibition. *Neuron*, *56*(1), 33–42. https://doi.org/10.1016/j.neuron.2007.09.012

Freund, T. F., & Katona, I. (2007b). Perisomatic Inhibition. *Neuron*, *56*(1), 33–42. https://doi.org/10.1016/j.neuron.2007.09.012

Fung, J. C., Liu, W., de Ruijter, W. J., Chen, H., & Abbey, C. K. (1996). Toward Fully Automated High-Resolution Electron Tomography. *Journal of Structural Biology*, *116*, 181–189. https://doi.org/10.1006/jsbi.1996.0029

Galow, L. V., Schneider, J., Lewen, A., Ta, T. T., Papageorgiou, I. E., & Kann, O. (2014). Energy substrates that fuel fast neuronal network oscillations. *Frontiers in Neuroscience*, *8*(DEC), 1–12. https://doi.org/10.3389/fnins.2014.00398

Geiger, J. R. P., Lübke, J., Roth, A., Frotscher, M., & Jonas, P. (1997). Submillisecond AMPA receptor-mediated signaling at a principal neuron- interneuron synapse. *Neuron*, *18*(6), 1009–1023. https://doi.org/10.1016/S0896-6273(00)80339-6

Gertler, T. S., Chan, C. S., & Surmeier, D. J. (2008). Dichotomous Anatomical Properties of Adult Striatal Medium Spiny Neurons. *Journal of Neuroscience*, *28*(43), 10814–10824. https://doi.org/10.1523/JNEUROSCI.2660-08.2008

Gibson, H. E., Edwards, J. G., Page, R. S., Van Hook, M. J., & Kauer, J. A. (2008). TRPV1 Channels Mediate Long-Term Depression at Synapses on Hippocampal Interneurons. *Neuron*, *57*(5), 746–759. https://doi.org/10.1016/j.neuron.2007.12.027

Gilbert, P. (1972). The Reconstruction of a Three-Dimensional Structure from Projections and Its Application to Electron Microscopy. II. Direct Methods. *Proceedings of the Royal Society B: Biological Sciences*, *182*(1066), 89–102. https://doi.org/10.1098/rspb.1972.0068

Goldberg, J. H., Tamas, G., Aronov, D., & Yuste, R. (2003). Calcium microdomains in aspiny dendrites. *Neuron*, *40*(4), 807–821. https://doi.org/10.1016/S0896-6273(03)00714-1

Gonchar, Y. (2008). Multiple distinct subtypes of GABAergic neurons in mouse visual cortex identified by triple immunostaining. *Frontiers in Neuroanatomy*, *1*(March). https://doi.org/10.3389/neuro.05.003.2007

Gong, Q., Hu, X., Pettersson-Yeo, W., Xu, X., Lui, S., Crossley, N., … Mechelli, A. (2017). Network-Level Dysconnectivity in Drug-Naï¿½ve First-Episode Psychosis: Dissociating Transdiagnostic and Diagnosis-Specific Alterations. *Neuropsychopharmacology*, *42*(4), 933–940. https://doi.org/10.1038/npp.2016.247

Gould, S. J., & Lewontin, R. C. (1979). The Spandrels of San Marco and the Panglossian Paradigm: A Critique of the Adaptationist Programme. *Proceedings of the Royal Society B: Biological Sciences*, *205*(1161), 581–598. https://doi.org/10.1098/rspb.1979.0086

Govindarajan, A., Kelleher, R. J., & Tonegawa, S. (2006). A clustered plasticity model of

long-term memory engrams. *Nature Reviews. Neuroscience*, *7*(7), 575–583. https://doi.org/10.1038/nrn1937

Granger, A. J., Wallace, M. L., & Sabatini, B. L. (2017). Multi-transmitter neurons in the mammalian central nervous system. *Current Opinion in Neurobiology*, *45*, 85–91. https://doi.org/10.1016/j.conb.2017.04.007

Gray, E. G. (1959). Axo-somatic and axo-dendritic synapses of the cerebral cortex. *Journal of Anatomy*, *93*(Pt 4), 420–433. https://doi.org/10.1038/1831592a0

Gulledge, A. T., Carnevale, N. T., & Stuart, G. J. (2012). Electrical advantages of dendritic spines. *PLoS ONE*, *7*(4). https://doi.org/10.1371/journal.pone.0036007

Gulyá, A. I., Megías, M., Emri, Z., & Freund, T. F. (1999). Total Number and Ratio of Excitatory and Inhibitory Synapses Converging onto Single Interneurons of Different Types in the CA1 Area of the Rat Hippocampus. *The Journal of Neuroscience*, *19*(22), 10082–10097.

Gulyás, a I., Hájos, N., & Freund, T. F. (1996). Interneurons containing calretinin are specialized to control other interneurons in the rat hippocampus. *The Journal of Neuroscience : The Official Journal of the Society for Neuroscience*, *16*(10), 3397–3411.

Gulyás, A. I., Buzsáki, G., Freund, T. F., & Hirase, H. (2006). Populations of hippocampal inhibitory neurons express different levels of cytochrome c. *European Journal of Neuroscience*, *23*(10), 2581–2594. https://doi.org/10.1111/j.1460-9568.2006.04814.x

Gulyas, A. I., Szabo, G. G., Ulbert, I., Holderith, N., Monyer, H., Erdelyi, F., … Hajos,

N. (2010). Parvalbumin-Containing Fast-Spiking Basket Cells Generate the Field Potential Oscillations Induced by Cholinergic Receptor Activation in the Hippocampus. *Journal of Neuroscience*, *30*(45), 15134–15145. https://doi.org/10.1523/JNEUROSCI.4104-10.2010

Gulyás, A. I., Tóth, K., Dános, P., & Freund, T. F. (1991). Subpopulations of GABAergic neurons containing parvalbumin, calbindin D28k, and cholecystokinin in the rat hippocampus. *Journal of Comparative Neurology*, *312*(3), 371–378. https://doi.org/10.1002/cne.903120305

Haan, W. De, Pijnenburg, Y. A. L., Strijers, R. L. M., Van, Y., Made, D., Flier, W. M. Van Der, … Stam, C. J. (2009). Functional neural network analysis in frontotemporal dementia and Alzheimer ' s disease using EEG and graph theory, *12*, 1–12. https://doi.org/10.1186/1471-2202-10-101

Halasy, K., Buhl, E. H., Lörinczi, Z., Tamás, G., & Somogyi, P. (1996). Synaptic target selectivity and input of GABAergic basket and bistratified interneurons in the CA1 area of the rat hippocampus. *Hippocampus*, *6*(3), 306–329. https://doi.org/10.1002/(SICI)1098-1063(1996)6:3<306::AID-HIPO8>3.0.CO;2-K

Harris, K. D., Hochgerner, H., Skene, N. G., Magno, L., Katona, L., Bengtsson Gonzales, C., … Hjerling-Leffler, J. (2018). Classes and continua of hippocampal CA1 inhibitory neurons revealed by single-cell transcriptomics. *PLoS Biology*, *16*(6), e2006387. https://doi.org/10.1371/journal.pbio.2006387

Harris, K. M. (1994). CHAPTER 18 - Serial Electron Microscopy as an Alternative or Complement to Confocal Microscopy for the Study of Synapses and Dendritic

Spines in the Central Nervous System. In J. K. STEVENS, L. R. MILLS, & J. E. B. T.-T. C. M. TROGADIS (Eds.), *Cell Biology* (pp. 421–445). San Diego: Academic Press. https://doi.org/https://doi.org/10.1016/B978-0-12-668330-1.50022-3

Harris, K. M. (2014). Age-Dependent Responses of Dendrite Structure to Hippocampal Synaptic Plasticity. Retrieved from www.labroots.com/webinar/age-dependent-responses-of-dendrite-structure-to-hippocampal-synaptic-plasticity

Harris, K. M., & Kater, S. B. (1994). Dendritic spines: cellular specializations imparting both stability and flexibility to synaptic function. *Annual Review of Neuroscience*, *17*, 341–371. https://doi.org/10.1146/annurev.ne.17.030194.002013

Harris, K. M., Spacek, J., Bell, M. E., Parker, P. H., Lindsey, L. F., Baden, A. D., … Burns, R. (2015). A resource from 3D electron microscopy of hippocampal neuropil for user training and tool development. *Scientific Data*, *2*, 1–19. https://doi.org/10.1038/sdata.2015.46

Harris, K., Marshall, P. E., & Landis, D. M. (1985). Ultrastructural study of cholecystokinin-immunoreactive cells and processes in area CA1 of the rat hippocampus. *The Journal of Comparative Neurology*, *233*(2), 147–158. https://doi.org/10.1002/cne.902330202

Harris, K., & Stevens, J. (1988). Study of dendritic spines by serial electron microscopy and three-dimensional reconstructions. In: Intrinsic determinants of neuronal form and function. In *Neurology and Neurobiology* (pp. 179–199). New York.

Hauser, M., Wojcik, M., Kim, D., Mahmoudi, M., Li, W., & Xu, K. (2017). Correlative Super-Resolution Microscopy: New Dimensions and New Opportunities. *Chemical*

Reviews, *117*(11), 7428–7456. https://doi.org/10.1021/acs.chemrev.6b00604

Hayama, T., Noguchi, J., Watanabe, S., Takahashi, N., Hayashi-Takagi, A., Ellis-Davies, G. C. R., … Kasai, H. (2013). GABA promotes the competitive selection of dendritic spines by controlling local Ca(2+) signaling. *Nature Neuroscience*, *16*(10), 1409–1416. https://doi.org/10.1038/nn.3496

Hayworth, K. J., Xu, C. S., Lu, Z., Knott, G. W., Fetter, R. D., Tapia, J. C., … Hess, H. F. (2015). Ultrastructurally smooth thick partitioning and volume stitching for large-scale connectomics. *Nature Methods*, *12*(4), 319–322. https://doi.org/10.1038/nmeth.3292

Hebb, D. (1949). *The Organization of Behavior*.

Helmstaedter, M., Briggman, K. L., & Denk, W. (2008). 3D structural imaging of the brain with photons and electrons. *Current Opinion in Neurobiology*, *18*(6), 633–641. https://doi.org/10.1016/j.conb.2009.03.005

Hildebrand, D. G. C., Cicconet, M., Torres, R. M., Choi, W., Quan, T. M., Moon, J., … Engert, F. (2017). Whole-brain serial-section electron microscopy in larval zebrafish. *Nature*, *545*(7654), 345–349. https://doi.org/10.1038/nature22356

Hillman, E. M. C. (2014). Coupling Mechanism and Significance of the BOLD Signal: A Status Report. *Annual Review of Neuroscience*, *37*(1), 161–181. https://doi.org/10.1146/annurev-neuro-071013-014111

Hope, B. T., Michael, G. J., Knigge, K. M., & Vincent, S. R. (1991). Neuronal NADPH diaphorase is a nitric oxide synthase. *Proceedings of the National Academy of Sciences*, *88*(7), 2811–2814. https://doi.org/10.1073/pnas.88.7.2811

Hu, H., Gan, J., & Jonas, P. (2014a). Fast-spiking, parvalbumin+ GABAergic interneurons: From cellular design to microcircuit function. *Science*, *345*(6196). https://doi.org/10.1126/science.1255263

Hu, H., Gan, J., & Jonas, P. (2014b). Fast-spiking, parvalbumin+ GABAergic interneurons: From cellular design to microcircuit function. *Science*, *345*(6196), 1255263–1255263. https://doi.org/10.1126/science.1255263

Huchzermeyer, C., Berndt, N., Holzhütter, H.-G., & Kann, O. (2013). Oxygen Consumption Rates during Three Different Neuronal Activity States in the Hippocampal CA3 Network. *Journal of Cerebral Blood Flow & Metabolism*, *33*(2), 263–271. https://doi.org/10.1038/jcbfm.2012.165

Ichas, F., Jouaville, l. S., & Matzat, J.-P. (1997). Mitochondria are excitable organelles capaple of generating and conveying electric and calcium currents. *Cell*, *89*, 1145–1153.

Igarashi, K. M., Ito, H. T., Moser, E. I., & Moser, M. B. (2014). Functional diversity along the transverse axis of hippocampal area CA1. *FEBS Letters*, *588*(15), 2470–2476. https://doi.org/10.1016/j.febslet.2014.06.004

Januszewski, M., Kornfeld, J., Li, P. H., Pope, A., Blakely, T., Lindsey, L., … Jain, V. (2018). High-precision automated reconstruction of neurons with flood-filling networks. *Nature Methods*, *15*(August), 1–6. https://doi.org/10.1038/s41592-018-0049-4

Jensen, F. E., & Harris, K. M. (1989). Preservation of neuronal ultrastructure in hippocampal slices using rapid microwave-enhanced fixation. *Journal of*

Neuroscience Methods, *29*(3), 217–230. Retrieved from http://www.ncbi.nlm.nih.gov/pubmed/2507828

Jinno, S., Klausberger, T., Marton, L. F., Dalezios, Y., Roberts, J. D. B., Fuentealba, P., … Somogyi, P. (2007). Neuronal diversity in GABAergic long-range projections from the hippocampus. *The Journal of Neuroscience : The Official Journal of the Society for Neuroscience*, *27*(33), 8790–8804. https://doi.org/10.1523/JNEUROSCI.1847-07.2007

Johnstone, M., & Fetit, R. (2018). HippoCA3mpal Stem Cell Models Expose Dysfunctional Circuits in Schizophrenia. *Cell Stem Cell*, *22*(5), 609–611. https://doi.org/10.1016/j.stem.2018.04.008

Kageyama, G. H., & Wong-Riley, M. T. T. (1982). Histochemical localization of cytochrome oxidase in the hippocampus: Correlation with specific neuronal types and afferent pathways. *Neuroscience*, *7*(10), 2337–2361. https://doi.org/10.1016/0306-4522(82)90199-3

Kalweit, A. N., Amanpour-Gharaei, B., Colitti-Klausnitzer, J., & Manahan-Vaughan, D. (2017). Changes in Neuronal Oscillations Accompany the Loss of Hippocampal LTP that Occurs in an Animal Model of Psychosis. *Frontiers in Behavioral Neuroscience*, *11*(March), 1–15. https://doi.org/10.3389/fnbeh.2017.00036

Kann, O. (2012). The energy demand of fast neuronal network oscillations: Insights from brain slice preparations. *Frontiers in Pharmacology*, *3 JAN*(January), 1–6. https://doi.org/10.3389/fphar.2011.00090

Kann, O., Hollnagel, J.-O., Elzoheiry, S., & Schneider, J. (2016). Energy and Potassium

Ion Homeostasis during Gamma Oscillations. *Frontiers in Molecular Neuroscience*, *9*(June), 1–13. https://doi.org/10.3389/fnmol.2016.00047

Kann, O., Huchzermeyer, C., Kovács, R., Wirtz, S., & Schuelke, M. (2011). Gamma oscillations in the hippocampus require high complex i gene expression and strong functional performance of mitochondria. *Brain*, *134*(2), 345–358. https://doi.org/10.1093/brain/awq333

Kann, O., & Kovacs, R. (2006). Mitochondria and neuronal activity. *AJP: Cell Physiology*, *292*(2), C641–C657. https://doi.org/10.1152/ajpcell.00222.2006

Kann, O., Papageorgiou, I. E., & Draguhn, A. (2014). Highly energized inhibitory interneurons are a central element for information processing in cortical networks. *Journal of Cerebral Blood Flow and Metabolism*, *34*(8), 1270–1282. https://doi.org/10.1038/jcbfm.2014.104

Karnkowska, A., Vacek, V., Zubáčová, Z., Treitli, S. C., Petrželková, R., Eme, L., … Hampl, V. (2016). A eukaryote without a mitochondrial organelle. *Current Biology*, *26*(10), 1274–1284. https://doi.org/10.1016/j.cub.2016.03.053

Kasthuri, N., Hayworth, K. J., Berger, D. R., Schalek, R. L., Conchello, J. A., Knowles-Barley, S., … Lichtman, J. W. (2015). Saturated Reconstruction of a Volume of Neocortex. *Cell*, *162*(3), 648–661. https://doi.org/10.1016/j.cell.2015.06.054

Kawaguchi, Y. (1993). Physiological, morphological, and histochemical characterization of three classes of interneurons in rat neostriatum. *The Journal of Neuroscience : The Official Journal of the Society for Neuroscience*, *13*(11), 4908–4923. Retrieved from http://www.ncbi.nlm.nih.gov/pubmed/7693897

Kawaguchi, Y., & Kubota, Y. (1993). Correlation of physiological subgroupings of nonpyramidal cells with parvalbumin- and calbindinD28k-immunoreactive neurons in layer V of rat frontal cortex. *Journal of Neurophysiology*, *70*(1), 387–396. https://doi.org/10.1152/jn.1993.70.1.387

Kempermann, G., Jessberger, S., Steiner, B., & Kronenberg, G. (2004). Milestones of neuronal development in the adult hippocampus. *Trends in Neurosciences*, *27*(8), 447–452. https://doi.org/10.1016/j.tins.2004.05.013

Kirov, S. a, Sorra, K. E., & Harris, K. M. (1999). Slices have more synapses than perfusion-fixed hippocampus from both young and mature rats. *The Journal of Neuroscience : The Official Journal of the Society for Neuroscience*, *19*(8), 2876–2886. Retrieved from http://www.ncbi.nlm.nih.gov/pubmed/10191305

Kita, H., Kosaka, T., & Heizmann, C. W. (1990). Parvalbumin-immunoreactive neurons in the rat neostriatum: a light and electron microscopic study. *Brain Research*, *536*(1–2), 1–15. https://doi.org/10.1016/0006-8993(90)90002-S

Klausberger, T. (2009). GABAergic interneurons targeting dendrites of pyramidal cells in the CA1 area of the hippocampus. *The European Journal of Neuroscience*, *30*(6), 947–957. https://doi.org/10.1111/j.1460-9568.2009.06913.x

Klausberger, T., & Somogyi, P. (2008). Neuronal Diversity and Temporal Dynamics: The Unity of Hippocampal Circuit Operations. *Science*, *321*(5885), 53–57. https://doi.org/10.1126/science.1149381

Kleinfeld, D., Blinder, P., Drew, P. J., Driscoll, J. D., Muller, A., Tsai, P. S., & Shih, A. Y. (2011). A guide to delineate the logic of neurovascular signaling in the brain.

Frontiers in Neuroenergetics, *3*(APRIL), 1–9. https://doi.org/10.3389/fnene.2011.00001

Koch ', C., & Zador, A. (1993). The Function of Dendritic Spines: Devices Subserving Biochemical Rather Than Electrical Compartmentalization. *The Journal of Neuroscience*, *13*(2), 413–422. https://doi.org/10.1523/JNEUROSCI.13-02-00413.1993

Köhler, C., & Chan-Palay, V. (1982). Somatostatin-like immunoreactive neurons in the hippocampus: An immunocytochemical study in the rat. *Neuroscience Letters*, *34*(3), 259–264. https://doi.org/10.1016/0304-3940(82)90185-9

Kojetin, D. J., Venters, R. A., Kordys, D. R., Thompson, R. J., Kumar, R., & Cavanagh, J. (2006). Structure, binding interface and hydrophobic transitions of Ca 2+-loaded calbindin-D28K. *Nature Structural and Molecular Biology*, *13*(7), 641–647. https://doi.org/10.1038/nsmb1112

Kornfeld, J., & Denk, W. (2018). Progress and remaining challenges in high-throughput volume electron microscopy. *Current Opinion in Neurobiology*, *50*, 261–267. https://doi.org/10.1016/j.conb.2018.04.030

Koster, A. J., Chen, H., Sedat, J. W., & Agard, D. A. (1992). Automated microscopy for electron tomography. *Ultramicroscopy*, *46*(1–4), 207–227. https://doi.org/10.1016/0304-3991(92)90016-D

Kullmann, D. M. (2011). Interneuron networks in the hippocampus. *Current Opinion in Neurobiology*, *21*(5), 709–716. https://doi.org/10.1016/j.conb.2011.05.006

Kullmann, D. M., & Lamsa, K. P. (2011). LTP and LTD in cortical GABAergic

interneurons: Emerging rules and roles. *Neuropharmacology*, *60*(5), 712–719. https://doi.org/10.1016/j.neuropharm.2010.12.020

Kuwajima, M. (2014). Anti-Fluorophore Post-embedding Immunogold Labeling to Identify GFP-containing Cells.

Kuwajima, M., Mendenhall, J. M., & Harris, K. M. (2013). Large-volume reconstruction of brain tissue from high-resolution serial section images acquired by SEM-based scanning transmission electron microscopy. *Methods in Molecular Biology*, *950*, 253–273. https://doi.org/10.1007/978-1-62703-137-0_15

Kuwajima, M., Mendenhall, J. M., Lindsey, L. F., & Harris, K. M. (2013). Automated Transmission-Mode Scanning Electron Microscopy (tSEM) for Large Volume Analysis at Nanoscale Resolution. *PLoS ONE*, *8*(3), 1–14. https://doi.org/10.1371/journal.pone.0059573

Kyrozis, A., & Reichling, D. B. (1995). Perforated-patch recording with gramicidin avoids artifactual changes in intracellular chloride concentration. *Journal of Neuroscience Methods*, *57*(1), 27–35.

Lamsa, K., Heeroma, J. H., & Kullmann, D. M. (2005a). Hebbian LTP in feed-forward inhibitory interneurons and the temporal fidelity of input discrimination. *Nature Neuroscience*, *8*(7), 916–924. https://doi.org/10.1038/nn1486

Lamsa, K., Heeroma, J. H., & Kullmann, D. M. (2005b). Hebbian LTP in feed-forward inhibitory interneurons and the temporal fidelity of input discrimination. *Nature Neuroscience*, *8*(7), 916–924. https://doi.org/10.1038/nn1486

Lamsa, K., Irvine, E. E., Giese, K. P., & Kullmann, D. M. (2007). NMDA receptor-

dependent long-term potentiation in mouse hippocampal interneurons shows a unique dependence on Ca2+/ calmodulin-dependent kinases. *Journal of Physiology*, *584*(3), 885–894. https://doi.org/10.1113/jphysiol.2007.137380

Lamsa, K. P., Heeroma, J. H., Somogyi, P., Rusakov, D. A., & Kullmann, D. M. (2007). Anti-Hebbian long-term potentiation in the hippocampal feedback inhibitory circuit. *Science (New York, N.Y.)*, *315*(5816), 1262–1266. https://doi.org/10.1126/science.1137450

Lansing, E. (1984). PASSIVE CABLE PROPERTIES SPINY NEURONS1 OF DENDRITIC SPINES. *Journal of Neuroscience*.

Le Roux, N., Cabezas, C., Böhm, U. L., & Poncer, J. C. (2013). Input-specific learning rules at excitatory synapses onto hippocampal parvalbumin-expressing interneurons. *Journal of Physiology*, *591*(7), 1809–1822. https://doi.org/10.1113/jphysiol.2012.245852

Ledley, R. S., Di Chiro, G., Luessenhop, A. J., & Twigg, H. L. (1974). Computerized transaxial x-ray tomography of the human body. *Science (New York, N.Y.)*, *186*(4160), 207–212. Retrieved from http://www.ncbi.nlm.nih.gov/pubmed/4606376

Li, Z., Okamoto, K.-I., Hayashi, Y., & Sheng, M. (2004). The importance of dendritic mitochondria in the morphogenesis and plasticity of spines and synapses. *Cell*, *119*(6), 873–887. https://doi.org/10.1016/j.cell.2004.11.003

Lisman, J. (1989). A mechanism for the Hebb and the anti-Hebb processes underlying learning and memory. *Proceedings of the National Academy of Sciences*, *86*(23), 9574–9578. https://doi.org/10.1073/pnas.86.23.9574

Lisman, J., Cooper, K., Sehgal, M., & Silva, A. J. (2018). Memory formation depends on both synapse-specific modifications of synaptic strength and cell-specific increases in excitability. *Nature Neuroscience*, *21*(3), 309–314. https://doi.org/10.1038/s41593-018-0076-6

Lopez-pigozzi, D., Laurent, F., Brotons-mas, J. R., Valderrama, M., Fernandez-lamo, I., Cid, E., … Gal, B. (2016). Altered Oscillatory Dynamics of CA1 Parvalbumin Basket Cells during Theta – Gamma Rhythmopathies of Temporal Lobe Epilepsy, *3*(December).

Lorén, I., Emson, P. C., Fahrenkrug, J., Björklund, A., Alumets, J., Håkanson, R., & Sundler, F. (1979). Distribution of vasoactive intestinal polypeptide in the rat and mouse brain. *Neuroscience*, *4*(12), 1953–1976. https://doi.org/10.1016/0306-4522(79)90068-X

Löscher, W. (2017). Animal Models of Seizures and Epilepsy: Past, Present, and Future Role for the Discovery of Antiseizure Drugs. *Neurochemical Research*, *42*(7), 1873–1888. https://doi.org/10.1007/s11064-017-2222-z

Maccaferri, G., & Lacaille, J.-C. (2003). Interneuron Diversity series: Hippocampal interneuron classifications--making things as simple as possible, not simpler. *Trends in Neurosciences*, *26*(10), 564–571. https://doi.org/10.1016/j.tins.2003.08.002

Maccaferri, G., & McBain, C. J. (1996). Long-term potentiation in distinct subtypes of hippocampal nonpyramidal neurons. *The Journal of Neuroscience : The Official Journal of the Society for Neuroscience*, *16*(17), 5334–5343.

MacKinnon, R., Cohen, S. L., Kuo, A., Lee, A., & Chait, B. T. (1998). Structural

conservation in prokaryotic and eukaryotic potassium channels. *Science (New York, N.Y.)*, *280*(5360), 106–109. https://doi.org/10.1126/science.280.5360.106

Magistretti, P. (2017). Neuron-glia metabolic coupling: Role in plasticity and neuroprotection. *Journal of the Neurological Sciences*, *381*(2017), 24. https://doi.org/10.1016/j.jns.2017.08.107

Magistretti, P. J. (2011). Neuron-glia metabolic coupling and plasticity. *Experimental Physiology*, *96*(4), 407–410. https://doi.org/10.1113/expphysiol.2010.053157

Makara, J. K., Losonczy, A., Wen, Q., & Magee, J. C. (2009). Experience-dependent compartmentalized dendritic plasticity in rat hippocampal CA1 pyramidal neurons. *Nature Neuroscience*, *12*(12), 1485–1487. https://doi.org/10.1038/nn.2428

Malinow, R., & Tsien, R. W. (1990). Presynaptic enhancement shown by whole cell recordings of long- term potentiation in hippocampal slices. *Nature*, *346*, 177–180.

Mancuso, J. J., Cheng, J., Yin, Z., Gilliam, J. C., Xia, X., Li, X., & Wong, S. T. C. (2014). Integration of multiscale dendritic spine structure and function data into systems biology models. *Frontiers in Neuroanatomy*, *8*(November), 1–15. https://doi.org/10.3389/fnana.2014.00130

Mangia, S., Simpson, I. A., Vannucci, S. J., & Carruthers, A. (2009). The in vivo neuron-to-astrocyte lactate shuttle in human brain: evidence from modeling of measured lactate levels during visual stimulation. *Journal of Neurochemistry*, *109 Suppl*(Suppl 1), 55–62. https://doi.org/10.1111/j.1471-4159.2009.06003.x

Marchand, I., Chorneyko, K., Tarnopolsky, M., Hamilton, S., Shearer, J., Potvin, J., & Graham, T. E. (2002). Quantification of subcellular glycogen in resting human

muscle: granule size, number, and location. *Journal of Applied Physiology*, *93*(5), 1598–1607. https://doi.org/10.1152/japplphysiol.00585.2001

Mariño, J., Schummers, J., Lyon, D. C., Schwabe, L., Beck, O., Wiesing, P., … Sur, M. (2005). Invariant computations in local cortical networks with balanced excitation and inhibition. *Nature Neuroscience*, *8*(2), 194–201. https://doi.org/10.1038/nn1391

Markram, H., Gerstner, W., & Sjöström, P. J. (2011). A history of spike-timing-dependent plasticity. *Frontiers in Synaptic Neuroscience*, (AUG), 1–24. https://doi.org/10.3389/fnsyn.2011.00004

Markram, H., Toledo-Rodriguez, M., Wang, Y., Gupta, A., Silberberg, G., & Wu, C. (2004). Interneurons of the neocortical inhibitory system. *Nature Reviews. Neuroscience*, *5*(10), 793–807. https://doi.org/10.1038/nrn1519

Marr, D. (1970). A Theory for Cerebral Neocortex. *Proceedings of the Royal Society B: Biological Sciences*, *176*(1043), 161–234. https://doi.org/10.1098/rspb.1970.0040

Marr, D. (1971). Simple Memory: A Theory for Archicortex. *Philosophical Transactions of the Royal Society B: Biological Sciences*, *262*(841), 23–81. https://doi.org/10.1098/rstb.1971.0078

Matsuzaki, M., Honkura, N., Ellis-Davies, G. C. R., & Kasai, H. (2004). Structural basis of long-term potentiation in single dendritic spines. *Nature*, *429*(6993), 761–766. https://doi.org/10.1038/nature02617

Mattson, M. P., Gleichmann, M., & Cheng, A. (2008). Mitochondria in neuroplasticity and neurological disorders. *Neuron*, *60*(5), 748–766. https://doi.org/10.1016/j.neuron.2008.10.010

Mayford, M., Siegelbaum, S. a, & Kandel, E. R. (2012). Synapses and memory storage. *Cold Spring Harbor Perspectives in Biology*, *4*(6). https://doi.org/10.1101/cshperspect.a005751

McBain, C. J., & Fisahn, A. (2001). Interneurons unbound. *Nature Reviews. Neuroscience*, *2*(1), 11–23. https://doi.org/10.1038/35049047

McBain, C. J., Freund, T. F., & Mody, I. (1999). Glutamatergic synapses onto hippocampal interneurons: Precision timing without lasting plasticity. *Trends in Neurosciences*, *22*(5), 228–235. https://doi.org/10.1016/S0166-2236(98)01347-2

McMahon, L. L., & Kauer, J. A. (1997). Hippocampal interneurons express a novel form of synaptic plasticity. *Neuron*, *18*(2), 295–305. https://doi.org/10.1016/S0896-6273(00)80269-X

Megías, M., Emri, Z., Freund, T. F., & Gulyás, A. I. (2001). Total number and distribution of inhibitory and excitatory synapses on hippocampal CA1 pyramidal cells. *Neuroscience*, *102*(3), 527–540. Retrieved from http://www.ncbi.nlm.nih.gov/pubmed/11226691

Megías, M., Emri, Z., Freund, T. ., & Gulyás, A. . (2001). Total number and distribution of inhibitory and excitatory synapses on hippocampal CA1 pyramidal cells. *Neuroscience*, *102*(3), 527–540. https://doi.org/10.1016/S0306-4522(00)00496-6

Messaoudii, C., Boudier, T., Sanchez Sorzano, C. O., & Marco, S. (2007). TomoJ: tomography software for three-dimensional reconstruction in transmission electron microscopy. *BMC Bioinformatics*, *8*, 288. https://doi.org/10.1186/1471-2105-8-288

Micheva, K. D., & Smith, S. J. (2007). Array tomography: a new tool for imaging the

molecular architecture and ultrastructure of neural circuits. *Neuron*, *55*(1), 25–36. https://doi.org/10.1016/j.neuron.2007.06.014

Mishchenko, Y., Hu, T., Spacek, J., Mendenhall, J., Harris, K. M., & Chklovskii, D. B. (2010). Ultrastructural analysis of hippocampal neuropil from the connectomics perspective. *Neuron*, *67*(6), 1009–1020. https://doi.org/10.1016/j.neuron.2010.08.014

Moore, C. I., & Cao, R. (2008). The hemo-neural hypothesis : on the role of blood flow in information processing. *The Journal of Neurophysiology*, *99*, 2035–2047. https://doi.org/10.1152/jn.01366.2006.

Müller, M., Mironov, S. L., Ivannikov, M. V., Schmidt, J., & Richter, D. W. (2005). Mitochondrial organization and motility probed by two-photon microscopy in cultured mouse brainstem neurons. *Experimental Cell Research*, *303*(1), 114–127. https://doi.org/10.1016/j.yexcr.2004.09.025

Nakazawa, E., Ogasawa, M., Yotsuji, T., & Hashimoto, T. (2006). 3D reconstruction system of H-7650 TEM for tomography and its application to biological specimen. *Hitachi E.M. News*, 1–6.

Neumann, W., Huebl, J., Brücke, C., Lofredi, R., Horn, A., Saryyeva, A., … Kühn, A. A. (2018). Pallidal and thalamic neural oscillatory patterns in Tourette syndrome. *Annals of Neurology*. https://doi.org/10.1002/ana.25311

Nickell, S., Förster, F., Linaroudis, A., Del Net, W., Beck, F., Hegerl, R., … Plitzko, J. M. (2005). TOM software toolbox: Acquisition and analysis for electron tomography. *Journal of Structural Biology*, *149*(3), 227–234.

https://doi.org/10.1016/j.jsb.2004.10.006

Noske, A. B., Costin, A. J., Morgan, G. P., & Marsh, B. J. (2008). Expedited approaches to whole cell electron tomography and organelle mark-up in situ in high-pressure frozen pancreatic islets. *Journal of Structural Biology*, *161*(3), 298–313. https://doi.org/10.1016/j.jsb.2007.09.015

Ohyama, T., Schneider-Mizell, C. M., Fetter, R. D., Aleman, J. V., Franconville, R., Rivera-Alba, M., … Zlatic, M. (2015). A multilevel multimodal circuit enhances action selection in Drosophila. *Nature*, *520*(7549), 633–639. https://doi.org/10.1038/nature14297

Oldendorf, W. H. (1961). Isolated Flying Spot Detection of Radiodensity Dis-Continuities-Displaying the Internal Structural Pattern of a Complex Object. *IRE Transactions on Bio-Medical Electronics*, *8*(1), 68–72. https://doi.org/10.1109/TBMEL.1961.4322854

Ostroff, L. E., Fiala, J. C., Allwardt, B., & Harris, K. M. (2002). Polyribosomes redistribute from dendritic shafts into spines with enlarged synapses during LTP in developing rat hippocampal slices. *Neuron*, *35*(3), 535–545. Retrieved from http://www.ncbi.nlm.nih.gov/pubmed/12165474

Overly, C. C., Rieff, H. I., & Hollenbeck, P. J. (1996). Organelle motility and metabolism in axons vs dendrites of cultured hippocampal neurons. *Journal of Cell Science*, *109 (Pt 5*, 971–980. https://doi.org/1996/05/01 00:01

Pawelzik, H., Hughes, D. I., & Thomson, A. M. (2003). Modulation of inhibitory autapses and synapses on rat CA1 interneurones by GABA $_a$ receptor ligands. *The*

Journal of Physiology, *546*(3), 701–716. https://doi.org/10.1113/jphysiol.2002.035121

Pelkey, K. A., Chittajallu, R., Craig, M. T., Tricoire, L., Wester, J. C., & McBain, C. J. (2017a). Hippocampal GABAergic Inhibitory Interneurons. *Physiological Reviews*, *97*(4), 1619–1747. https://doi.org/10.1152/physrev.00007.2017

Pelkey, K. A., Chittajallu, R., Craig, M. T., Tricoire, L., Wester, J. C., & McBain, C. J. (2017b). Hippocampal GABAergic Inhibitory Interneurons. *Physiological Reviews*, *97*(4), 1619–1747. https://doi.org/10.1152/physrev.00007.2017

Penttonen, M., Kamondi, A., Acsády, L., & Buzsáki, G. (1998). Gamma frequency oscillation in the hippocampus of the rat: Intracellular analysis in vivo. *European Journal of Neuroscience*, *10*(2), 718–728. https://doi.org/10.1046/j.1460-9568.1998.00096.x

Perez, Y., Morin, F., & Lacaille, J.-C. (2001). A hebbian form of long-term potentiation dependent on mGluR1a in hippocampal inhibitory interneurons. *Proceedings of the National Academy of Sciences*, *98*(16), 9401–9406. https://doi.org/10.1073/pnas.161493498

Petilla Interneuron Nomenclature Group, Ascoli, G. A., Alonso-Nanclares, L., Anderson, S. A., Barrionuevo, G., Benavides-Piccione, R., … Yuste, R. (2008). Petilla terminology: nomenclature of features of GABAergic interneurons of the cerebral cortex. *Nature Reviews. Neuroscience*, *9*(7), 557–568. https://doi.org/10.1038/nrn2402

Petryszyn, S., Parent, A., & Parent, M. (2018). The calretinin interneurons of the

striatum: comparisons between rodents and primates under normal and pathological conditions. *Journal of Neural Transmission*, *125*(3), 279–290. https://doi.org/10.1007/s00702-017-1687-x

Phan, S., & Lawrence, A. (2008). Tomography of large format electron microscope tilt series: Image alignment and volume reconstruction. *Proceedings - 1st International Congress on Image and Signal Processing, CISP 2008*, *2*, 176–182. https://doi.org/10.1109/CISP.2008.535

Polsky, A., Mel, B. W., & Schiller, J. (2004). Computational subunits in thin dendrites of pyramidal cells. *Nature Neuroscience*, *7*(6), 621–627. https://doi.org/10.1038/nn1253

Pouille, F., & Scanziani, M. (2001). Enforcement of temporal fidelity in pyramidal cells by somatic feed-forward inhibition. *Science*, *293*(5532), 1159–1163. https://doi.org/10.1126/science.1060342

Ramón y Cajal, S. (1904). *Histologia del Systema Nervioso del Hombre y de los Vertebrados*. Madrid.

Ramón y Cajal, S. (1989). *Recollections of my Life* (3rd ed.). philadelphia: MIT Press.

Rebecca D Hodge, Trygve E Bakken, Jeremy A Miller, Kimberly A Smith, Eliza R Barkan, Lucas T Graybuck, Jennie L Close, Brian Long, Osnat Penn, Zizhen Yao, Jeroen Eggermont, Thomas Hollt, Boaz P Levi, Soraya I Shehata, Brian Aevermann, Allison Beller, Darr, E. S. L. (2018). Conserved cell types with divergent features between human and mouse cortex. *BioRxiv*, 1–112. https://doi.org/10.1101/384826

Roach, P. J., Depaoli-Roach, A. A., Hurley, T. D., & Tagliabracci, V. S. (2012).

Glycogen and its metabolism: some new developments and old themes. *Biochemical Journal*, *441*(3), 763–787. https://doi.org/10.1042/BJ20111416

Roberts, J. C., McCrossan, M. V, & Jones, H. B. (1990). The case for perfusion fixation of large tissue samples for ultrastructural pathology. *Ultrastructural Pathology*, *14*(2), 177–191.

Rogers, J. H. (1987). Calretinin: A gene for a novel calcium-binding protein expressed principally in neurons. *Journal of Cell Biology*, *105*(3), 1343–1353. https://doi.org/10.1083/jcb.105.3.1343

Roux, L., & Buzsáki, G. (2015). Tasks for inhibitory interneurons in intact brain circuits. *Neuropharmacology*, *88*(September), 10–23. https://doi.org/10.1016/j.neuropharm.2014.09.011

Roy, C. S., & Sherrington, C. S. (1890). On the Regulation of the Blood-supply of the Brain. *The Journal of Physiology*, *11*(1–2), 85–158.17.

Royer, S., Zemelman, B. V., Losonczy, A., Kim, J., Chance, F., Magee, J. C., & Buzsáki, G. (2012). Control of timing, rate and bursts of hippocampal place cells by dendritic and somatic inhibition. *Nature Neuroscience*, *15*(5), 769–775. https://doi.org/10.1038/nn.3077

Ryan, K., Lu, Z., & Meinertzhagen, I. A. (2016). The CNS connectome of a tadpole larva of Ciona intestinalis (L.) highlights sidedness in the brain of a chordate sibling. *ELife*, *5*(DECEMBER2016), 1–34. https://doi.org/10.7554/eLife.16962

Saalfeld, S., Cardona, A., Hartenstein, V., & Tomančák, P. (2009). CATMAID: Collaborative annotation toolkit for massive amounts of image data. *Bioinformatics*,

25(15), 1984–1986. https://doi.org/10.1093/bioinformatics/btp266

Saez, I., Duran, J., Sinadinos, C., Beltran, A., Yanes, O., Tevy, M. F., … Guinovart, J. J. (2014a). Neurons have an active glycogen metabolism that contributes to tolerance to hypoxia. *Journal of Cerebral Blood Flow and Metabolism*, *34*(6), 945–955. https://doi.org/10.1038/jcbfm.2014.33

Saez, I., Duran, J., Sinadinos, C., Beltran, A., Yanes, O., Tevy, M. F., … Guinovart, J. J. (2014b). Neurons Have an Active Glycogen Metabolism that Contributes to Tolerance to Hypoxia. *Journal of Cerebral Blood Flow & Metabolism*, *34*(6), 945–955. https://doi.org/10.1038/jcbfm.2014.33

Samudra, N., Ivleva, E. I., Hubbard, N. A., Rypma, B., Sweeney, J. A., Clementz, B. A., … Tamminga, C. A. (2015). Alterations in hippocampal connectivity across the psychosis dimension. *Psychiatry Research - Neuroimaging*, *233*(2), 148–157. https://doi.org/10.1016/j.pscychresns.2015.06.004

Scheffer, M., Bascompte, J., Brock, W. a, Brovkin, V., Carpenter, S. R., Dakos, V., … Sugihara, G. (2009). Early-warning signals for critical transitions. *Nature*, *461*(7260), 53–59. https://doi.org/10.1038/nature08227

Scheuss, V., & Bonhoeffer, T. (2013). Function of Dendritic Spines on Hippocampal Inhibitory Neurons. *Cerebral Cortex (New York, N.Y. : 1991)*, (line M), 1–12. https://doi.org/10.1093/cercor/bht171

Scheuss, V., & Bonhoeffer, T. (2014). Function of dendritic spines on hippocampal inhibitory neurons. *Cerebral Cortex*, *24*(12), 3142–3153. https://doi.org/10.1093/cercor/bht171

Schmidt-Hieber, C., Jonas, P., & Bischofberger, J. (2007). Subthreshold Dendritic Signal Processing and Coincidence Detection in Dentate Gyrus Granule Cells. *Journal of Neuroscience*, *27*(31), 8430–8441. https://doi.org/10.1523/JNEUROSCI.1787-07.2007

Silver, R. A. (2010a). Neuronal arithmetic. *Nature Reviews. Neuroscience*, *11*(7), 474–489. https://doi.org/10.1038/nrn2864

Silver, R. A. (2010b). Neuronal arithmetic. *Nature Reviews Neuroscience*, *11*(7), 474–489. https://doi.org/10.1038/nrn2864

Smith, D. H. (2009). Stretch growth of integrated axon tracts: Extremes and exploitations. *Progress in Neurobiology*, *89*(3), 231–239. https://doi.org/10.1016/j.pneurobio.2009.07.006

Smith, H. L., Bourne, J. N., Cao, G., Chirillo, M. A., Ostroff, L. E., Watson, D. J., & Harris, K. M. (2016). Mitochondrial support of persistent presynaptic vesicle mobilization with age-dependent synaptic growth after LTP. *ELife*, *5*(DECEMBER2016), 1–30. https://doi.org/10.7554/eLife.15275

Sohal, V. S., Zhang, F., Yizhar, O., & Deisseroth, K. (2009). Parvalbumin neurons and gamma rhythms enhance cortical circuit performance. *Nature*, *459*(7247), 698–702. https://doi.org/10.1038/nature07991

Soltesz, I., & Losonczy, A. (2018). CA1 pyramidal cell diversity enabling parallel information processing in the hippocampus. *Nature Neuroscience*, *21*(4), 484–493. https://doi.org/10.1038/s41593-018-0118-0

Somogyi, J., Szabo, A., Somogyi, P., & Lamsa, K. (2012). Molecular analysis of ivy cells

of the hippocampal CA1 stratum radiatum using spectral identification of immunofluorophores. *Frontiers in Neural Circuits*, *6*(May), 35. https://doi.org/10.3389/fncir.2012.00035

Sorra, K. E., Fiala, J. C., & Harris, K. M. (1998). Critical assessment of the involvement of perforations, spinules, and spine branching in hippocampal synapse formation. *The Journal of Comparative Neurology*, *398*(2), 225–240. Retrieved from http://www.ncbi.nlm.nih.gov/pubmed/9700568

Soto, G. E., Young, S. J., Martone, M. E., Deerinck, T. J., Lamont, S., Carragher, B. O., … Ellisman, M. H. (1994). Serial section electron tomography: a method for three-dimensional reconstruction of large structures. *NeuroImage*. https://doi.org/10.1006/nimg.1994.1008

Sousa, A. A., Azari, A. A., Zhang, G., & Leapman, R. D. (2011). Dual-axis electron tomography of biological specimens: Extending the limits of specimen thickness with bright-field STEM imaging. *Journal of Structural Biology*, *174*(1), 107–114. https://doi.org/10.1016/j.jsb.2010.10.017

Sparagna, G. C., Gunter, K. K., Sheu, S.-S., & Gunter, T. E. (1995). Mitochondrial Calcium Uptake from Physiological-type Pulses of Calcium. *Journal of Biological Chemistry*, *270*(46), 27510–27515. https://doi.org/10.1074/jbc.270.46.27510

Spinoza, B. (1677). *The Ethics*. The Hague.

Squire, L. R. (2009). The legacy of patient H.M. for neuroscience. *Neuron*, *61*(1), 6–9. https://doi.org/10.1016/j.neuron.2008.12.023

Subramaniam, S., & Zhang, P. (2003). Electron Tomography: a Powerful Tool for 3D

Cellular Microscopy. *ASM News-American …*, *69*(5), 240–245. Retrieved from http://forms.asm.org/ASM/files/CCLIBRARYFILES/FILENAME/0000000316/nw20030061p.pdf

Sun, Y., Nitz, D. A., Holmes, T. C., & Xu, X. (2018). Opposing and Complementary Topographic Connectivity Gradients Revealed by Quantitative Analysis of Canonical and Noncanonical Hippocampal CA1 Inputs. *ENeuro*, *5*(1), ENEURO.0322-17.2018. https://doi.org/10.1523/ENEURO.0322-17.2018

Takács, V. T., Szőnyi, A., Freund, T. F., Nyiri, G., & Gulyás, A. I. (2015). Quantitative ultrastructural analysis of basket and axo-axonic cell terminals in the mouse hippocampus. *Brain Structure & Function*, *220*(2), 919–940. https://doi.org/10.1007/s00429-013-0692-6

Tamura, H., Ikegaya, Y., & Shiosaka, S. (2006). Hippocampal CA1 synaptic plasticity as a gamma transfer function. *Neuroscience*, *138*(4), 1049–1053. https://doi.org/10.1016/j.neuroscience.2006.01.004

Tanaka, S., Sako, K., Tanaka, T., Nishihara, I., & Yonemasu, Y. (1990). Uncoupling of local blood flow and metabolism in the hippocampal CA3 in kainic acid-induced limbic seizure status. *Neuroscience*, *36*(2), 339–348. https://doi.org/10.1016/0306-4522(90)90430-C

Tasic, B. (2018). Single cell transcriptomics in neuroscience: cell classification and beyond. *Current Opinion in Neurobiology*, *50*, 242–249. https://doi.org/10.1016/j.conb.2018.04.021

Todorova, V., & Blokland, A. (2017). Mitochondria and Synaptic Plasticity in the Mature

and Aging Nervous System. *Current Neuropharmacology*, *15*(1), 166–173. https://doi.org/10.2174/1570159X14666160414111821

Tognoli, E., & Kelso, J. A. S. (2014). The Metastable Brain. *Neuron*, *81*(1), 35–48. https://doi.org/10.1016/j.neuron.2013.12.022

Tóth, K., & McBain, C. J. (1998). Afferent-specific innervation of two distinct AMPA receptor subtypes on single hippocampal interneurons. *Nature Neuroscience*, *1*(7), 572–578. https://doi.org/10.1038/2807

Tricoire, L., Pelkey, K. A., Erkkila, B. E., Jeffries, B. W., Yuan, X., & McBain, C. J. (2011). A Blueprint for the Spatiotemporal Origins of Mouse Hippocampal Interneuron Diversity. *Journal of Neuroscience*, *31*(30), 10948–10970. https://doi.org/10.1523/JNEUROSCI.0323-11.2011

Tricoire, L., & Vitalis, T. (2012). Neuronal nitric oxide synthase expressing neurons: a journey from birth to neuronal circuits. *Frontiers in Neural Circuits*, *6*(December), 1–16. https://doi.org/10.3389/fncir.2012.00082

Turnbull, J., Girard, J. M., Lohi, H., Chan, E. M., Wang, P., Tiberia, E., … Minassian, B. A. (2012). Early-onset Lafora body disease. *Brain*, *135*(9), 2684–2698. https://doi.org/10.1093/brain/aws205

Tyan, L., Chamberland, S., Magnin, E., Camire, O., Francavilla, R., David, L. S., … Topolnik, L. (2014). Dendritic Inhibition Provided by Interneuron-Specific Cells Controls the Firing Rate and Timing of the Hippocampal Feedback Inhibitory Circuitry. *Journal of Neuroscience*, *34*(13), 4534–4547. https://doi.org/10.1523/JNEUROSCI.3813-13.2014

Urban, A., Rancillac, A., Martinez, L., & Rossier, J. (2012). Deciphering the neuronal circuitry controlling local blood flow in the cerebral cortex with optogenetics in PV:: Cre transgenic mice. *Frontiers in Pharmacology*, *3 JUN*(June), 1–8. https://doi.org/10.3389/fphar.2012.00105

Valles-Ortega, J., Duran, J., Garcia-Rocha, M., Bosch, C., Saez, I., Pujadas, L., … Guinovart, J. J. (2011). Neurodegeneration and functional impairments associated with glycogen synthase accumulation in a mouse model of Lafora disease. *EMBO Molecular Medicine*, *3*(11), 667–681. https://doi.org/10.1002/emmm.201100174

van Aarle, W., Palenstijn, W. J., De Beenhouwer, J., Altantzis, T., Bals, S., Batenburg, K. J., & Sijbers, J. (2015). The ASTRA Toolbox: A platform for advanced algorithm development in electron tomography. *Ultramicroscopy*, *157*, 35–47. https://doi.org/10.1016/j.ultramic.2015.05.002

van Hemmen, J. L., & Sejnowski, T. J. (2009). *23 Problems in Systems Neuroscience*. *23 Problems in Systems Neuroscience*. https://doi.org/10.1093/acprof:oso/9780195148220.001.0001

Vodovozov, W., Schneider, J., Elzoheiry, S., Hollnagel, J., Lewen, A., & Kann, O. (2018). Metabolic modulation of neuronal gamma-band oscillations, 1377–1389.

Waitt, A. E., Reed, L., Ransom, B. R., & Brown, A. M. (2017). Emerging Roles for Glycogen in the CNS. *Frontiers in Molecular Neuroscience*, *10*(March), 1–10. https://doi.org/10.3389/fnmol.2017.00073

Wamsley, B., & Fishell, G. (2017). Genetic and activity-dependent mechanisms underlying interneuron diversity. *Nature Reviews Neuroscience*, *18*(5), 299–309.

https://doi.org/10.1038/nrn.2017.30

Wang, X., Wang, X., Allen, W. E., Wright, M. A., Sylwestrak, E. L., Samusik, N., … Deisseroth, K. (2018). Three-dimensional intact-tissue sequencing of single-cell transcriptional states, *5691*(June), 1–18. https://doi.org/10.1126/science.aat5691

Washburn, M. S., Numberger, M., Zhang, S., & Dingledine, R. (1997). Differential dependence on GluR2 expression of three characteristic features of AMPA receptors. *The Journal of Neuroscience : The Official Journal of the Society for Neuroscience*, *17*(24), 9393–9406. https://doi.org/10.1523/jneurosci.5023-03.2004

Watanabe, S., Lehmann, M., Hujber, E., Fetter, R. D., Richards, J., Söhl-Kielczynski, B., … Jorgensen, E. M. (2014). *Nanometer-resolution fluorescence electron microscopy (Nano-EM) in cultured cells*. *Methods in Molecular Biology* (Vol. 1117). https://doi.org/10.1007/978-1-62703-776-1_22

White, J. G., Southgate, E., Thomson, J. N., & Brenner, S. (1986). The Structure of the Nervous System of the Nematode Caenorhabditis elegans. *Philosophical Transactions of the Royal Society B: Biological Sciences*, *314*(1165), 1–340. https://doi.org/10.1098/rstb.1986.0056

Wierenga, C. J., Müllner, F. E., Rinke, I., Keck, T., Stein, V., & Bonhoeffer, T. (2010). Molecular and electrophysiological characterization of GFP-expressing CA1 interneurons in GAD65-GFP mice. *PloS One*, *5*(12), e15915. https://doi.org/10.1371/journal.pone.0015915

Williamson, P. (2007). Are anticorrelated networks in the brain relevant to schizophrenia? *Schizophrenia Bulletin*, *33*(4), 994–1003.

https://doi.org/10.1093/schbul/sbm043

Xu, C. S., Hayworth, K. J., Lu, Z., Grob, P., Hassan, A. M., García-Cerdán, J. G., … Hess, H. F. (2017). Enhanced FIB-SEM systems for large-volume 3D imaging. *ELife*, *6*, 1–36. https://doi.org/10.7554/eLife.25916

Yeckel, M. F., & Berger, T. W. (1990). Feedforward excitation of the hippocampus by afferents from the entorhinal cortex: redefinition of the role of the trisynaptic pathway. *Proceedings of the National Academy of Sciences*, *87*(15), 5832–5836. https://doi.org/10.1073/pnas.87.15.5832

Yu, Y., Migliore, M., Hines, M. L., & Shepherd, G. M. (2014). Sparse Coding and Lateral Inhibition Arising from Balanced and Unbalanced Dendrodendritic Excitation and Inhibition. *Journal of Neuroscience*, *34*(41), 13701–13713. https://doi.org/10.1523/JNEUROSCI.1834-14.2014

Zheng, Q. S., Braunfeld, M. B., Sedat, J. W., & Agard, D. A. (2004). An improved strategy for automated electron microscopic tomography. *Journal of Structural Biology*, *147*(2), 91–101. https://doi.org/10.1016/j.jsb.2004.02.005

Zheng, S. Q., Keszthelyi, B., Branlund, E., Lyle, J. M., Braunfeld, M. B., Sedat, J. W., & Agard, D. A. (2007). UCSF tomography: An integrated software suite for real-time electron microscopic tomographic data collection, alignment, and reconstruction. *Journal of Structural Biology*, *157*(1), 138–147. https://doi.org/10.1016/j.jsb.2006.06.005

Zheng, Z., Lauritzen, J. S., Perlman, E., Robinson, C. G., Nichols, M., Milkie, D., … Bock, D. D. (2018). A Complete Electron Microscopy Volume of the Brain of Adult

Drosophila melanogaster. *Cell*, *174*(3), 730–743.e22. https://doi.org/10.1016/j.cell.2018.06.019

Zhou, Q., Homma, K. J., & Poo, M. (2004). Shrinkage of dendritic spines associated with long-term depression of hippocampal synapses. *Neuron*, *44*(5), 749–757. https://doi.org/10.1016/j.neuron.2004.11.011

Zhu, P., Liu, J., Bess, J., Chertova, E., Lifson, J. D., Grisé, H., … Roux, K. H. (2006). Distribution and three-dimensional structure of AIDS virus envelope spikes. *Nature*, *441*(7095), 847–852. https://doi.org/10.1038/nature04817